All-Carbon Polyradical Architectures

by

Matthew D Rollings

A dissertation submitted in partial satisfaction of the
requirements for the degree of
Doctor of Philosophy
in
Chemistry
in the
Graduate Division
of the
University of California, Berkeley

Committee in charge:
Professor Felix Fischer, Chair
Professor Dean Toste
Professor Michael F. Crommie

Summer 2023

All-Carbon Polyradical Architectures

By

Matthew D Rollings

Abstract

Open-Shell Character and Magnetic Order in Low-Dimensional Carbon Nanomaterials

By

Matthew D Rollings

Doctor of Philosophy in Chemistry

University of California, Berkeley

Professor Felix Fischer, Chair

Scanning probe techniques at the vacuum-solid interface have unlocked new avenues in the synthesis and study of reactive materials. The study of stable radicals has grown as a field since the onset of the twentieth century. Polyaromatic hydrocarbons (PAHs) have represented a significant portion of these studies. Though as the degree of radical or radicaloid nature of target structures increases, their solution synthesis and study become more challenging. Diradical(oid)s have been studied more regularly since the end of the twentieth century, with the achievement of tetraradical(oid)s and hexaradical(oid)s occurring only in the last few years. The solid-vacuum interfaces and scanning probe microscopy (SPM) have permitted an enormous leap in the accessibility of target structures and the robustness of characterization. For example, zigzag-edged graphene nanoribbons, unsubstituted triangulene molecules, and magnetic porphyrins have been studied using these methods. These methods have allowed a more detailed inspection of the magnetic properties of open-shell carbon materials. The work described in this dissertation targets all-carbon polyradical nanomaterials for the study of fundamental phenomena in carbon magnetism. This work has implications for next-generation spintronics and quantum computing. Chapter 2 focuses on the synthesis of a modular spin supergraphene of $S = ½$ phenalenyl and its 1-dimensional superpolyacetylene analogues. Chapter 3 focuses on the analogous study of $S = 1$ triangulene modular periodic materials. Chapter 4 focuses on 1-dimensional polyradical graphene nanoribbons (GNRs) in solution and at the vacuum-gold interface. These materials hold promise for achieving fully integrated molecular circuits. And finally, Chapter 5 focuses on 0-dimensional magnetic structures, biphenalenyl and bottom-up synthesis of a nitrogen-vacancy (NV) center.

Contents

1 Introduction

1.1 Graphene nanomaterials

Graphene is a 2-D material: a planar sheet of sp^2-hybridized carbon atoms in a hexagonal honeycomb lattice and was first isolated in 2004 by Geim and Novoselov.[1] Graphene demonstrates impressive mechanical strength, thermodynamic stability, charge carrier mobility, nonlinear diamagnetism, and other useful physical properties.[2–6] The lamellar structure of graphite was first suggested in 1859 and in 1947, P.R. Wallace was the first to study the theoretical properties of the material.[7,8] Fullerenes, a class of nanomaterials consisting of a closed or partially closed mesh of graphene sp^2 carbon atoms, have been the subject of theoretical interest since C_{60}, buckminsterfullerene, was proposed in 1970.[9] Their accidental synthesis in 1985 led to their discovery in nature and a swell of research interest in these buckyballs, buckybowls, and carbon nanotubes.[10] The discovery of graphene in 2004 led to another surge in research interest in the burgeoning field of carbon nanomaterials, winning the 2010 Nobel Prize in physics. Around this time, graphene nanoribbons were first synthesized—planar analogues to quasi-1-dimensional carbon nanotubes.[11] Carbon nanomaterials at their nanoscopic limit, however, have been studied for nearly two centuries. Polyaromatic hydrocarbon (PAH) chemistry has been a rich field of interest since the isolation of benzene and naphthalene in the early nineteenth century.[12,13] These hydrogen-passivated nanoflakes of graphene exhibit unique optoelectronic properties depending on their size,[14,15] topology,[16–18] constituent ring-size,[19–22] and physical distortion.[23–26] The optoelectronic and open-shell properties of PAHs have been explored, ranging from their use as dyes,[27–29] to multiexciton generators,[30–34] to quantum dots.[35–38] They have been investigated for their open-shell character[39–41] and the qualities of their stable radicals.[42–45] Recently, there has increased interest in low-dimensional carbon-based magnetic materials.[46–51]

1.2 Magnetic properties of carbon nanomaterials

Carbon nanomaterials' ability to display magnetic properties results from the electron's intrinsic magnetic moment, which results from an intrinsic, quantized angular momentum of fundamental particles, as demonstrated by the Stern-Gerlach experiment.[52–55] The allowed values for the electron spin (s) are described by **Equation 1**, for any non-negative integer, n.

$$s = \frac{n}{2} \tag{1}$$

The spin of an elementary particle is dependent only on its identity, with electrons having a spin quantum number of ½. The spin magnetic quantum number, m_s, can take on values ranging from $-s$ to $+s$ in integer increments, hence –½ or +½ for an electron. In an atom or molecule, the electron spin magnetic numbers combine to give a total molecular spin, S. Paired electrons take on opposite values of m_s, according to the Pauli exclusion principle, hence closed-shell molecules, in which all electrons are paired into bonds, take on a value of $S = 0$. An atom or molecule with two unpaired electrons, however, can take on a value of $S = 0$ or $S = 1$, depending on the relative alignment of the electrons' spin magnetic quantum numbers. The magnetic moment (μ_s) of a spin-S particle is described by **Equation 2**, where e is the electron charge, m is the mass, and g is the "g-factor," an empirical constant relating the observed magnetic moment to the particle's spin magnetic quantum number.

$$\mu_s = \frac{ge}{2m} S \tag{2}$$

Stable free radicals host unpaired electrons, thus hosting their collective magnetic moment. The history of stable organic radicals predates the theory of the magnetic moment of electrons, beginning with Gomberg's study of the triphenyl methyl, or "trityl" radical in 1900.[42] Interest in stable organic radicals grew over the course of the twentieth century, with increasing interest in the trityl system, the postulation and exploration of the phenalenyl radical, and the discovery of the kinetically stabilizing effects of polychlorination and thermodynamically stabilizing effects of heteroatom incorporation, especially nitroxide groups.[56–64] For the focus of this work, stable organic radicals that include heteroatoms will be excluded, e.g. perchlorinated radicals and nitronylnitroxides.[60,62,64] All-carbon spin systems present an advantageous scaffold for exploiting the magnetic potential of carbon nanomaterials for two reasons. One: carbon is a light element with low spin-orbit coupling, allowing for large spin coherence times and lengths.[65] Two: the lack of heteroatoms, even light ones like nitrogen, means that there is no thermodynamic driving force for electrons to localize preferentially to any atomic sites due to electronegativity, potentially disrupting ballistic transport and the other advantages of graphene-based materials. [66,67]

In the 123 years since Gomberg's discovery of aromatically stabilized radicals, a rational design toolkit has been developed for manipulating the magnetic properties of PAHs and kinetically stabilizing their open-shell, reactive nature. There are four primary design principles for promoting (poly)radical open-shell character in PAHs: (1) aromatic stabilization driving force (2) zig-zag edge incorporation, (3) sublattice manipulation, and (4) topological frustration. Scanning probe microscopy (SPM), a powerful mode of inquiry has obviated the need for kinetic stabilization of reactive radicals by studying them at a solid-vacuum interface where radical quenching by reaction with molecular oxygen is not a risk.[50,68–74]

1.2.1 Aromatic stabilization energy

Clar's rule for aromatic sextets provides a powerful qualitative method for understanding and assessing a range of complex physical phenomena in PAHs. Clar's rule states that the resonance structures with a larger number of benzenoid units (**Figure 1.1A**) contribute more strongly to the overall resonance hybrid.[75–77] This can be used to drive biradical character when PAHs are designed in such a way that the energy penalty of dividing a π-bond into two π-radicals is compensated by the stabilization energy of the resultant aromatic sextets.[78,79] The term biradical or open-shell "character" is a careful choice of words—these molecules are not truly biradical; they have a strong contribution from biradical resonance structures to the resonance hybrid structure. The biradical character of a molecule (y_0) is calculated from the natural orbital occupation of its highest occupied molecular orbital (HOMO) and lowest unoccupied molecular orbital (LUMO).[80] The energy penalty of the biradical results from partial occupation of the higher-energy LUMO. This method has also been used to drive biradical character in structures containing five-membered rings.[81]

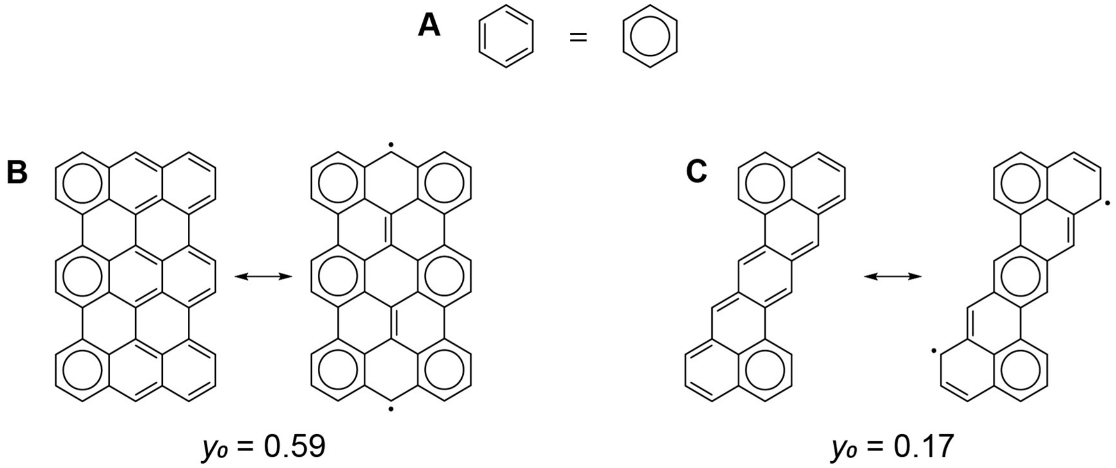

Figure 1.1 (A) circle notation for Clar's aromatic sextet rule, ,**(B)** teranthene[82] and **(C)** heptazethrene[83] molecules that have significant biradical character due to a driving force to aromatic stabilization energy

1.2.2 Topological frustration

Topological frustration can imbue a molecule with a pure biradical state, different from the biradical *character* described above, which is a result of partial LUMO occupation. In chemical terms, topological frustration describes a molecule that has two or more unpaired radical π-electrons that are unable to form a bond with each other due to the topology (*i.e.* connectivity) of the atoms in the molecule.[73,84] The phenomenon is demonstrated in 2,2'-biphenalenyl and Clar's goblet (**Figure 1.2**Error! Reference source not found.). The radical electrons cannot be paired into a π-bond using conventional Lewis dot structures and electron pushing. Due to the unmixed nature of the ground state of topologically frustrated molecules, these systems are highly desirable for carbon-based magnetic materials.

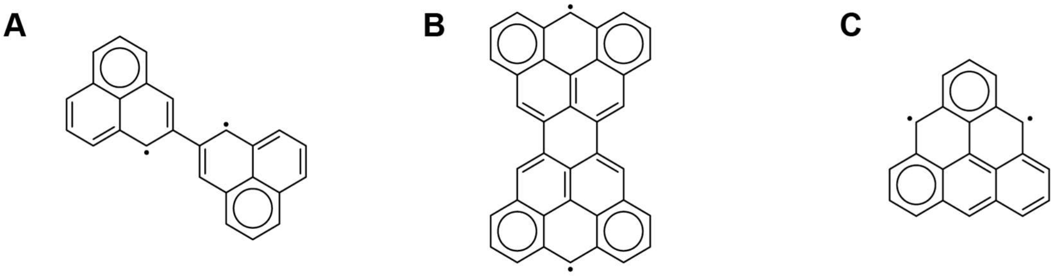

Figure 1.2 Topological frustration depicted in **(A)** 2,2'-biphenalenyl, **(B)** Clar's goblet, **(C)** triangulene

1.2.3 Zig-zag edged nanographenes

Another design principle for promoting open-shell character in nanographenes is the incorporation of zig-zag edges. Nanographene structures can have two edge morphologies: zig-zag (**Figure 1.3A**, blue) and armchair (**Figure 1.3A**, red). Zig-zag edges impart open-shell character and high reactivity, while armchair edges impart levels of reactivity comparable to that of olefins and aromatics. These relative reactivities are exemplified by oligoacenes for zig-zag edges[85] and pyrene for armchair edges.[86] The relative reactivity of these edge morphologies can be explained by Clar's rule, as described above. An armchair edge may present a Clar sextet in the fashion of a *p*-polyphenylene motif (**Figure 1.3A**, left and right edges) or olefinic double bonds when demanded by the overall nanographene structure (**Figure 1.3A**, top-right and bottom-right corners) and therefore presents a corresponding reactivity. A zig-zag edge, however, presents A single Clar sextet followed by a series of sequential double bonds until the structure is terminated (**Figure 1.3A**, top and bottom edges). This structural motif is observed in polyacenes (**Figure 1.3B**), which have been studied extensively due to their open-shell diradical characteristics that increase with increasing length, *n*.[85,87–89] This behavior can be explained by analyzing the Lewis structures of the oligoacenes using the principles of Clar's rule for the exchange of LUMO occupation, which is compensated for by aromatic stabilization energy. This tradeoff only becomes available with increasing polyacene size. Furthermore, the single Clar sextet structure always has N resonance structures, whereas the double Clar sextet structure has resonance structures that scale superexponentially with N (1 for N = 3, 4 for N = 4, 10 for N = 5) and for each addition of two benzenoid units, resonance structures with two additional radicals become attainable, leading to tetraradicaloid behavior (N = 5 and beyond), hexaradical behavior (N = 7 and beyond), and so on. These factors increasingly promote contributions of the open-shell resonance structures to the resonance hybrid structure, and thus diradical character (y_0) of the oligoacene, where pentacene (N = 5) is the first oligoacene with nontrivial y_0 (**Figure 1.3B**, table).

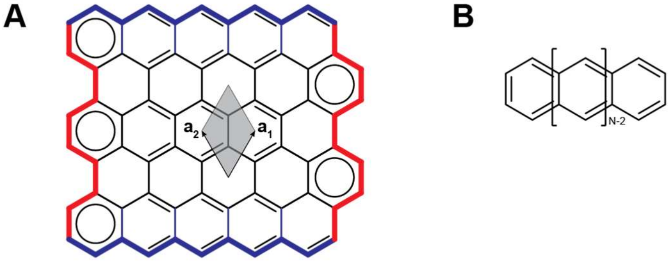

C

N	y_0
2	0.000
3	0.000
4	0.000
5	0.118
6	0.330
7	0.541
8	0.666

Figure 1.3 (A) subsection of graphene depicting zig-zag edges (blue), armchair edges (red), graphene unit cell (grey) and graphene unit cell vectors (arrows a_1 and a_2). **(B)** Chemical structure of polyacenes and associated y_0 values[85]

Rhombenes are another exemplary case of zig-zag edged molecules with open-shell character and magnetic properties.[49] In 2021, Mishra *et al.* demonstrated the size-dependent open-shell properties of a new class of zig-zag-edged rhombus-shaped nanographenes that they termed [*n*]-rhombenes, where *n* is the number of benzenoid rings along each edge of the rhombus. Much like the oligoacene series, the emergent open-shell characteristics can be explained by assessing all possible resonance structures and analysis of the tradeoff between Clar sextets and radical pairs. Study of [4]- and [5]-rhombene at the vacuum-metal interface permitted determination of the singlet-triplet energy gap (ΔE_{ST}) by inelastic electron tunneling spectroscopy.[49] Determination of ΔE_{ST} using optical spectroscopic techniques in oligoacenes is a standard characterization metric.[85,87,90,91] The application of scanning tunneling spectroscopy to determine the quantity in rhombenes showcases the power of scanning probe characterization techniques. The singlet ground state of polyacenes and [*n*]-rhombenes is explained by Lieb's theorem, which will be discussed in depth in the subsequent subchapter on graphene sublattice manipulation in nanographenes.

Finally, zig-zag edged graphene nanoribbons (GNRs) represent the infinite limit of zig-zag edge incorporation.[92] GNRs in general will be introduced in more depth below, but zig-zag GNRs, are known to have highly reactive edges that easily oxidize, much like bare metal surfaces in air. ZGNRs were originally thought to be conducting half-metals according to simulations,[93] but were later described to be magnetic semiconductors.[94,95] Extended ZGNRs were predicted to host magnetic order with spin polarization localized across both edges, displaying ferromagnetic order across each edge and antiferromagnetic order between the two edges.[96] ZGNRs can be thought of as polyacenes that are extended in both the longitudinal and transverse directions and their highly reactive, open-shell, and magnetic behavior is a natural consequence of the application of Clar sextets described above and Lieb’s theorem described below.

1.2.4 Sublattice effects in nanographenes

Sublattice imbalance is a design principle based on Lieb’s theorem for alternant aromatic hydrocarbons. Alternant aromatic hydrocarbons consist exclusively of six-membered rings. Lieb’s theorem states that if you divide the graphene sublattice into two, interpenetrating, bipartite sublattices (A and B sublattices) and count the number of atoms on each sublattice (N_A and N_B), the net spin of the molecule is given by **Equation 3**.[97]

$$\boldsymbol{S} = \frac{\boldsymbol{N_A - N_B}}{\boldsymbol{2}} \tag{3}$$

In other words, the spin up and spin down electrons in nanographenes partition themselves into the A and B sublattice, respectively. Therefore, a nanographene with an excess of A sites relative to B sites accumulates a net spin scaling with the extent of the sublattice imbalance (**Figure 1.4**). Lieb’s theorem explains the singlet ground state of polyacenes, 2,2’-biphenalenyl, and Clar’s goblet as well as the triplet ground state of triangulene. Note that molecules with high-spin ground states by Lieb’s theorem also demonstrate topological frustration between electrons on the majority sublattice (*e.g.,* triangulene).

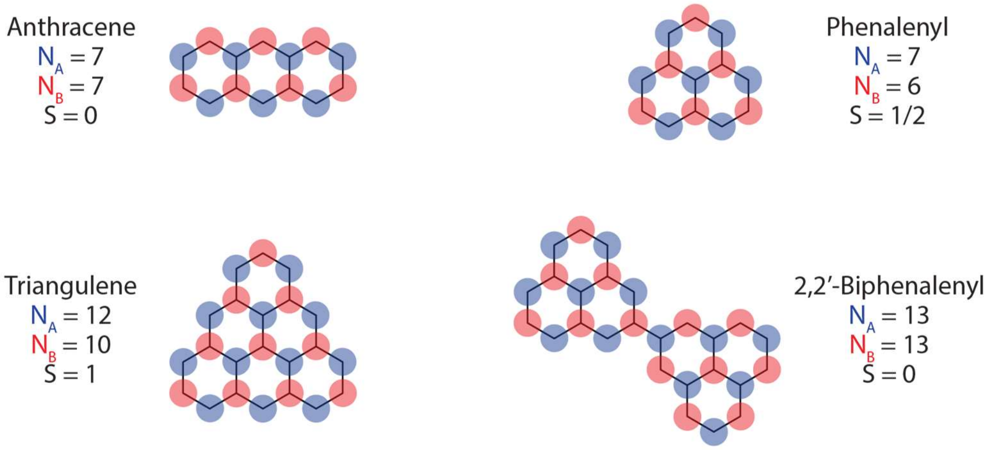

Figure 1.4 Graphical representation of Lieb’s theorem applied to a set of alternant aromatic hydrocarbons

Lieb’s theorem applies equally well to analysis of the unit cells of periodic 1- and 2-dimensional materials. This was first exploited in 2020 by Rizzo *et. al.*, in which study the authors designed and synthesized an armchair GNR with periodic addition of methylbenzo- substituents that graphitize in the final structure, yielding periodically incorporated, short zig-zag segments and concomitant addition of a single A site per unit cell in a structure termed the sawtooth GNR (sGNR).[98] Despite the addition of an excess A site per unit cell, the overall structure displayed metallic, not ferromagnetic structure due to hybridization of spin states in a strong-binding regime. The possibility of state hybridization in a tight-binding regime must be considered when designing polyradical structures and will be discussed further below.

Furthermore, Rizzo *et. al.* observed another sublattice effect: sublattice mixing. Upon annealing to sufficient temperature, the sGNR cyclodehydrogenated further, yielding the unexpected 5-sGNR structure where the “teeth” of the sawtooth GNR cyclodehydrogenate to form a bond with the GNR edge, closing into 5-membered rings periodically in the structure. The resulting structure remains metallic, but while the sGNR metallic band is highly localized, a flat band in its energy band diagram, the 5sGNR metallic state delocalizes significantly through the ribbon, yielding a wide-band metal. This occurs via sublattice mixing—the bipartite description of the underlying graphene lattice is broken by connecting two A sites via the formation of an odd-membered ring, a non-alternant structure. Sublattice mixing is a useful tool because it can be used to tune band energy, band width, and promote stability.[98,99] These techniques are commonly used in the preparation of PAHs with tunable physical properties.[100]

1.2.5 [*n*]Triangulenes

Triangulenes are a class of triangular, zig-zag edged, topologically frustrated, and sublattice imbalanced, high-spin nanographenes.[101] The nomenclature for triangulenes is [*n*]triangulene, where *n* is the number of benzenoid rings per edge (**Figure 1.5**). The high-spin nature of triangulenes is explained by Lieb's theorem and has been supported experimentally.[68–71,102–105]

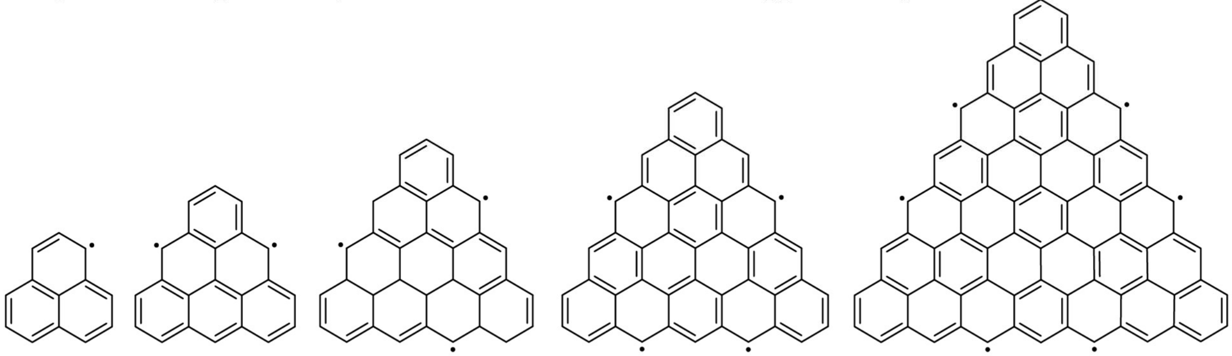

Figure 1.5 Triangulene-class molecules synthesized to-date. From left to right: [2]triangulene ("phenalenyl"),[102] [3]triangulene ("triangulene"),[68,102] [4]triangulene,[69] [5]triangulene,[70] and [7]triangulene[71]

The history of triangulenes begins with [2]triangulene, historically known as phenalenyl. Phenalenyl was first postulated in the early 1940s as a potential radical formed from perinaphthenone (antiquated, now: phenalenone).[57] The phenalenyl radical was detected transiently in 1957.[106] Reid presented a useful review of the properties of phenalene and related compounds in 1965.[107] Much later, in 1999, renewed interest in phenalenyl arose in the field of stable organic radicals, which led to the synthesis of a kinetically stable phenalenyl radical by steric protection of radical density using *t*-butyl groups.[103] This compound and a variety of other 2,5,8-trisubstituted phenalenyl species were characterized by UV-Vis absorption spectroscopy and single crystal X-ray analysis. In the 2010s, theoretical and experimental interest in the phenalenyl radicals ability to form reversible 12-center-2-electron "pancake" bonds by face-to-face alignment of the π-system of two phenalenyl radicals led to a flurry of publications interrogating the dynamics of terminal σ-dimers and fluxional π-dimers.[108–110] Novel iterations of the phenalenyl system continued to be synthesized in the solution state and studied for some years[111–113] until attention switched to studying open-shell nanographenes at the solid-vacuum interface with Pavliček and coworkers synthesis of unsubstituted triangulene.[68]

The history of [3]triangulene, historically known simply as triangulene and the namesake of the family, begins with Clar's postulating the frustrated diradical structure and attempting its synthesis in 1953.[114] Unsubstituted triangulene was found to quickly polymerize or rearrange and could not be observed even transiently, despite significant effort. In 2001, Inoue continued Goto's work by synthesizing kinetically stabilized tri-*t*-butyltriangulene and characterizing the structure in solution for the first time. In 2017, a landmark study was presented by Pavliček *et. al.* at IBM Zurich in which the authors synthesized unsubstituted triangulene at the copper-vacuum interface and characterized it with scanning probe techniques. This led to a flurry of publications on

[*n*]triangulenes,[68–71,102] [*n*]triangulene derivatives,[49,73,115,116] and [*n*]triangulene superstructures.[50,72,117,118] This is the context in which I began my study of polyradical graphene nanomaterials.

1.3 Applications of magnetic carbon nanomaterials

Near continuous advances in the academic realm don't equate to corresponding shifts to applying new technological paradigms due to technological entrenchment and manufacturing scalability. So despite persistent effort and consistent claims of newer, faster, more energy-efficient logic devices, metal-oxide-semiconductor field-effect transistor (MOSFET) technology first deployed commercially in 1971[119] remains the only type of microprocessor available on the market. With half a trillion dollars invested globally in new chip fabrication plants and over a trillion semiconductor units produced annually, microprocessors based on silicon MOSFETs are deeply entrenched.[120,121] In order to supplant this technology, a compelling alternative must be proposed for investment over the next decades or even century. The benefits of transitioning to a new technology, therefore, must be great to justify the obsolescence of trillions of dollars' worth of infrastructure. It is in this context that academic researchers pursue that holy grail—a decisive leap in performance, speed, energy efficiency, processability, sustainability, and more.

1.3.1 New materials and mechanisms for logic switches

Microprocessors based on FETs manufactured from silicon wafers monopolize logic devices across the board. A logic device can be described by its materials (*e.g.,* polycrystalline silicon, aluminum) and its architecture (*e.g.* complementary metal oxide semiconductor, tunneling field effect transistor, thin-film transistor), where the architecture refers to the type and arrangement of individual components (*e.g.* source, drain, gate, channel). The fundamental mechanism of switching is determined by the device architecture; *e.g.* MOSFET logic switches modulate the channel current between low current (OFF) and high current (ON) states, which is governed by thermionic emission.[122] This switching mechanism has a fundamental limit to its speed and efficiency, which fundamental limit is determined theoretically based on the architecture and mechanism of the switching device. While there is research thrust in improving logic efficiency from the software side,[123] all-new architectures will be needed to overcome these limits.[122,124]

One thrust for the improvement of logic devices is materials development for FETs.[125–128] Another thrust designing novel device architectures.[129,130] In the quest for a drastic improvement in logic device performance, carbon nanomaterials represent one promising research thrust for improving semiconductor FET technologies,[91,131,132] Semiconductor FETs, however, suffer from poor energy efficiency. FETs switch between a low current OFF state and a high current ON state, but it is not the current draw of the ON state that causes high power consumption. The capacitance of device interconnects and sub-threshold swing inhibit the energy efficiency of these devices. Spintronics utilize the spin degree of freedom as a means of information storage, which offer an attractive alternative to thermionic emission-based devices because spin-flip transitions are very low in energy—near the minimum, in fact,[133] hence the recent explosion in research focus on spintronics.[134,135] The work described herein marries these two realms of inquiry: exploring novel carbon nanomaterials for spintronic and quantum computing devices.

1.3.2 Magnetic materials, magnetic order, and magnons

Spin is a fundamental property carried by elementary particles that provides a useful framework for logic applications because of its binary nature. In theory, any spin-carrying particle could be used to store information or perform logical operations. In practice, however, electron spins are targeted for spintronic applications. Nuclear spin transitions are too low in energy (radio wave regime) to be useful, as thermal fluctuations and background radio waves are too great of sources of decoherence. Because the intrinsic magnetic moment of a spin-containing particle scales with the reciprocal of the particle mass, electrons have a greater magnetic moment. Electronic spin transitions fall in the microwave or far infrared regime, which overlaps with the Landauer limit of minimum energy dissipation for logic devices.[133] Making use of electron spin as a reliable unit of energy storage requires designing environments in which magnetic moments remain unquenched, are manipulable, and have available energetic transitions close to but greater than 20 meV. Carbon nanomaterials offer just such an avenue for satisfying these requirements and satisfying them on the smallest length scale physically accessible.

Over a century of research on the properties of open-shell hydrocarbons has laid the groundwork for this application. The atomic nuclei of molecules and materials can interfere with the electron spins discussed above by virtue of nuclear spins resulting from the specific combinations of protons and neutrons, themselves spin-½ particles. Heavier elements tend to have larger nuclear spins due to increasingly disproportionate amounts of neutrons to protons. Carbon, as a light element, has low spin-orbit coupling, permitting large spin coherence lengths and times.[65] Carbon-12 is spin-0 and has a natural abundance of 99%, with the remaining 1% abundance of spin-1/2 carbon-13 still permitting spin coherence on the order of tens of microseconds or longer.[136] The field is therefore ripe for the discovery of appropriate magnetic carbon nanomaterials based on currently amalgamated knowledge. The first thrust towards realizing carbon-based spin logic will be in developing a thorough understanding of magnetic carbon nanomaterials.

There are five basic varieties of magnetic order that can be achieved in solids: (**Figure 1.6**: 1-dimensional examples).[137] These can be described briefly as: diamagnetic (valence bonding), paramagnetic (non-interacting), ferromagnetic (parallel orientation), antiferromagnetic (antiparallel orientation), and ferrimagnetic (antiparallel spins of differing magnitudes; net magnetic moment). For the purposes of this thesis, ferrimagnetic materials will be excluded, though they are possible to achieve using the systems described and are potentially interesting areas of study. There are, furthermore, nine more specific subsets of magnetic behavior;[137] these will be neglected here as well.

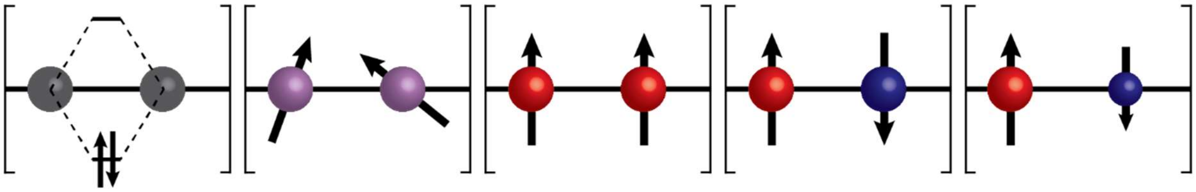

Figure 1.6 Graphical representation of magnetic order in 1-D chains. From top to bottom: diamagnetic, paramagnetic, ferromagnetic, antiferromagnetic, and ferrimagnetic

Graphical representations provide a useful mnemonic device, but the origin of these states should be described mathematically or quantum mechanically. The Hubbard model is a useful framework for describing these systems in a tight-binding model. In the Hubbard Hamiltonian, there are two parameters: a kinetic hopping integral, t, and an on-site potential energy, U.[138–140] Diamagnetic systems are found when the t is large relative to U. Paramagnetic systems are found when U/t is very large, for example because t is negligible or zero. Ferromagnetic and antiferromagnetic systems are found in the intermediate regime when U and t are not too large, but also not too similar in magnitude, with positive t corresponding to ferromagnetic order and negative t corresponding to antiferromagnetic order. When magnetic order exists, either ferro- or antiferro-, the magnitude of exchange coupling, J, is defined by **Equation 4**.[141]

$$|J| = \frac{4t^2}{U} \tag{4}$$

The exchange coupling energy corresponds to the energy required to excite a spin-flip transition. In a spin chain where each unit has identical spin, S, a spin-flip transition will cause the net magnetic moment of the material to shift by $2S$, either from NS to (N-2)S in the case of a ferromagnetic chain, or from net-zero to $\pm 2S$ in the case of an antiferromagnetic chain. Once again, thinking of this transition as simply flipping one of the spins in a linear chain, as represented in **Figure 1.6** is too simplistic and an accurate conception requires quantum mechanical consideration. Rigorously speaking, a spin-flip transition should be considered as a collective magnetic excitation and can be modeled as a quasiparticle, known as a magnon. While a single molecule is well described by a singlet-triplet transition, a similar transition in a periodic material is better considered as a magnon. This is analogous to the way lattice vibrations are modeled as phonons and electron excitations are modeled as excitons. Designing and synthesizing magnetically ordered materials is the first step to achieving spintronic devices; the next step is determining their magnonic properties, or the ways in which materials respond to, transmit, and maintain collective spin excitations. These properties must be well understood in order to understand how such materials can be applied for spin transduction in devices. Low-dimensional magnetically ordered materials with a tunable range of magnonic properties will be necessary for constructing spintronic devices for logic and other applications.

1.3.3 Scanning probe detection of magnetism and magnons

The materials generated for the studies described herein are characterized using scanning probe techniques: scanning tunneling microscopy (STM) and scanning tunneling spectroscopy (STS). STM generates topographic images (height, z, as a function of position, x,y) or differential conductance maps ($\mathrm{d}I/\mathrm{d}V$ as a function of position, x,y). Differential conductance, the first derivative of tunneling current with respect to sample bias (V_s) is used to probe the density of states (DOS). A spatial $\mathrm{d}I/\mathrm{d}V$ map, can therefore be used to probe the spatial distribution of molecular orbitals in molecules or energy bands in periodic materials.[142] STS measurements generate a differential conductance spectrum, which plots dI/dV against V_S.[143] This measurement is likewise used to assign a DOS, but relative to an energy scale, therefore yielding an experimental measurement of theoretically predictable molecular orbital energy diagrams and energy band diagrams.

In open-shell materials, $\mathrm{d}I/\mathrm{d}V$ spectra can furthermore reveal signature features that give insight into the spin structure of the material in addition to the electronic structure. Spin-polarized STM/STS is possible,[144,145] but our instruments are not capable of such measurements and therefore these techniques were not applied in these studies. The indirect features of open-shell and magnetic materials that can be revealed by spin-unpolarized STM/STS are (1) Kondo resonance for screened magnetic impurities on a metal surface, characterized by a reduced resistance at the Fermi level and therefore enhanced tunneling current. This is observed as a peak in the $\mathrm{d}I/\mathrm{d}V$ spectrum at zero bias with Fano lineshape[146] and (2) inelastic electron tunneling spectroscopy (IETS) for spin-flip, or magnonic excitations, characterized by enhanced tunneling current at energies exceeding the energy required excite the magnonic transition, yielding a U-shaped feature in the $\mathrm{d}I/\mathrm{d}V$ spectrum symmetric about zero bias.[147] This occurs because IETS, being an inelastic process, occurs when tunneling electrons/holes deposit a portion of their energy into the magnonic excitation. This can therefore occur at positive or negative bias beginning at the threshold energy of the transition, specifically the magnetic exchange energy, *J*, and remains as a channel for electron tunneling at higher biases. This is distinct from elastic electron tunneling spectroscopy features, the signature of molecular orbitals and energy bands, in which the augmented differential conductance occurs only for tunneling electrons that have energy resonant with the orbital or band through which they tunnel. In the elastic case, due to the resonance requirement, the augmented signal falls off exponentially as the bias voltage diverges from the resonant energy.[148]

1.4 2-D supergraphenes

Following the successful on-surface synthesis and characterization of unsubstituted [2], [3], [4], [5], and [7]triangulenes, intense focus has shifted to their dimers, polymers, and π-extended derivatives, some of which have already been studied and published.[49,50,72,73] The majority of the work described herein targets 2-dimensional spin networks from $S = ½$ [2]triangulene (**2T**) and $S = 1$ [3]triangulene(**3T**). Lewis dot structures, Hückel molecular orbital theory, density functional theory, and electron spin resonance experiments demonstrate that the radical spin density of **2T** is borne exclusively by what have been historically referred to as the α carbons with no spin density present on the apical carbons, historically termed the β carbons (**Figure 1.7A**). In current research on the [*n*]triangulene class of molecules of $n \geq 3$, the descriptive terms edge and apex/apical/corner are used (**Figure 1.7B**). The historical α/β nomenclature will therefore be eschewed here for the sake of consistency. For the higher triangulenes, this pattern continues: spin density is carried only by the edge carbons, not the apical carbons or interior carbons. It was therefore predicted that networking these triangular nanographenes through their apical carbons would inhibit radical recombination into a π-bond; in other words: topological frustration.

Interestingly, it was observed that due to the D_{3h} symmetry of **2T** and to its hosting a single p_z electron, 2-D networks of **2T**, when networked through the apical carbon atoms, could be considered a supergraphene in which the **2T** units act as sp^2 carbon superatoms (**Figure 1.7C**). The question then is whether the superstructure has the same bulk behavior as graphene itself—*e.g.*, zero bandgap semiconducting band structure and ballistic charge transport. The band structure and electronic/magnetic properties are determined by the relative values of the Hubbard parameters, *t* and *U* as described in Error! Reference source not found. above.

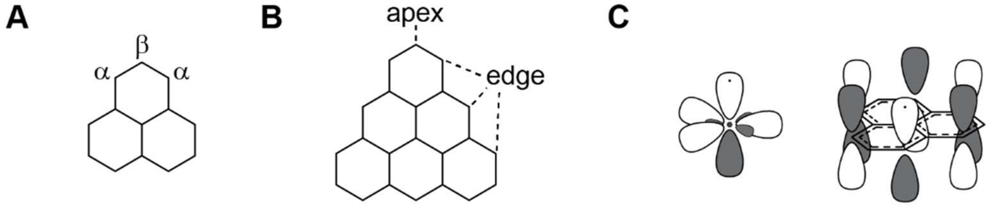

Figure 1.7 Positional nomenclature of **(A)** [2]triangulene and **(B)** [3]triangulene. **(C)** superatom analogy between sp^2 carbon atom (left) and [2]triangulene (right)

Furthermore, it was found in the course of synthesis that monomer precursors to 1-dimensional periodic chains of **2T** and **3T** were intermediates in the synthesis of the monomer precursor to the 2-D network. Divergent synthesis towards an analogous class of superpolyacetylenes was therefore completed as well.

1.4.1 Graphene and polyacetylene

Graphene and polyacetylene offer an instructive look into how the properties of 1-D and 2-D materials from near-identical unit cells can differ in fundamental properties, an observation that should inform hypotheses and analyses of 1-D and 2-D networks derived from triangulenes.

Graphene is a 2-D array of sp^2-hybridized carbon atoms in a honeycomb lattice. It is a zero-bandgap semiconductor, meaning that its valence and conduction bands overlap in only a single state at the Fermi level.[149] Graphene demonstrates impressive mechanical strength, charge carrier mobility, and other useful physical properties.[2–6] Graphene has been incorporated into a variety of applications, like batteries, sensors, catalysts, composite mechanical materials, and thermal applications.[150–154] Graphene is also used in research as an electrode or channel material in electronic and spintronic transistor devices,[155,156] as an interlayer in 2-D materials research,[157] 2-D stack devices,[158] and twistronics.[159] Developing a family of supergraphenes with similar but tunable properties to graphene would generate new opportunities for advanced materials and devices.

Polyacetylene is a 1-D linear array of sp^2-hybridized carbon atoms. It exists in two regioregular conformations: all-*cis* and all-*trans*. It was discovered in 1958 but found to be intractable and air-sensitive.[160,161] In the early 1970s, polyacetylene was synthesized in workable films and found to be metallic upon halogen-doping.[162–164] From a theoretical tight-binding model, a series of identical sites each containing a single electron should form a metallic band. Based on resonance hybrids of infinite *trans*-polyacetylene one might expect this emergent metallic behavior. However, from experiment, we know that polyacetylene is a semiconductor due to Peierls distortion, creating an alternating series of a single- and double-bonds, and therefore a discrimination between adjacent sites into a series of A sites and B sites. So taken *ab initio*, Poly([2]triangulene-2,5-diyl) (**poly-2T**) might be considered to be a superpolyacetylene, but taking the Peierls distortion as an intrinsic property of polyacetylene might dash such assignment. This nonequivalence, however, remains murky at best when inspecting ongoing debate as to the origin of semiconductivity in polyacetylene,[165] as well as the recent discovery of a substrate-dependent semiconducting-to-metallic transition in *trans*-polyacetylene on a Cu(110) surface.[166] The analogy will therefore be used in this thesis to refer to the analogous structure of **poly-2T** while recognizing that resulting "superpolyacetylenes," while structurally analogous may be variable in their symmetry and therefore in their resultant properties.

Developing these supergraphenes and superpolyacetylenes will open an array of opportunities for advanced materials and devices. These projects aim to develop a class of graphene and polyacetylene analogues that can be tuned to have metallic, semiconducting, and magnetic behavior with tunable properties like band gap, band width, magnetic exchange coupling, and more.

1.4.2 Phenalenyl, $S = ½$ and triangulene, $S = 1$ supergraphenes

As mentioned above, a [2]triangulene supergraphene (**2T-sg)** offers a curious reiteration of graphene itself, a metagraphene of sorts. Based on the carbon superatom analogy, **2T-sg** could be expected to be a dispersive graphene, a 2-dimensional honeycomb lattice with emergent Dirac cone band structure.[167–174] However, instead of a zero-bandgap semiconductor, we predicted that **2T-sg** should be an antiferromagnetic spin supergraphene due to topological frustration of radical electrons and overall sublattice balance by Lieb's theorem. The [3]triangulene supergraphene (**3T-sg**) structure is further interesting due to the addition of a second radical electron—a supergraphene where each superatomic site hosts two radical electrons in a high-spin triplet state. These structures are ripe for theoretical assessment, but ultimately, synthesis and characterization will be the only way to determine which interactions dominate. Furthermore, it is important to note that these structures are synthesized and characterized on a gold surface and the substrate effects must be considered because the ensemble properties likely differ from those that occur in the vacuum phase.

1.4.3 Modular synthesis of supergraphenes

Modular **2T-** and **3T-sg**s were targeted based on structural determination of effective Hubbard parameters in the resultant superstructures. It was predicted that the hopping parameter, *t*, which is determined by the spatial separation of sites and the energy states available in between sites, could be modified by changing the linking moiety that connects the triangulene units. The base supergaphenes are triangulene molecules connected simply by σ-bonds via apical carbons, and modular structures consist of those that incorporate linkers: biphenylene, acetylene, and phenylene (**Figure 1.8A**, **2T-sg**s). The analogous **2T-sp**s are depicted below (**Figure 1.8B**). The **3T** superstructures are omitted for brevity.

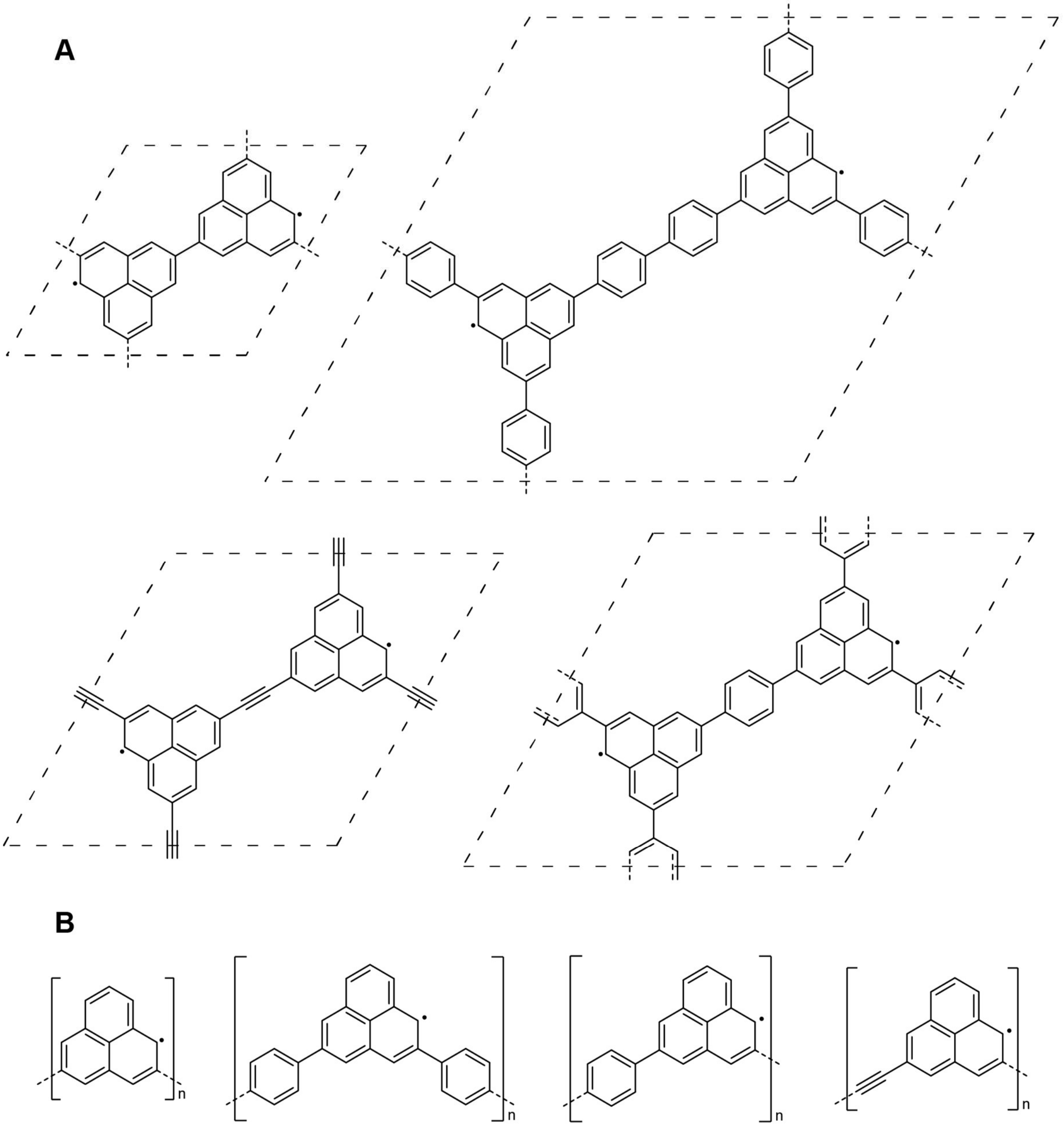

Figure 1.8 **(A)** 2T-supergraphene and **(B)** **2T**-superpolyacetylene target structures

It was further hypothesized that the on-site energy, *U*, could be tuned by changing the physical environment of the structure, *i.e.,* the substrate. Methods for achieving this in a scanning probe apparatus include: intercalating a monolayer of insulator such as potassium bromide or xenon,[68,175] dragging the carbon nanostructure onto a monolayer insulator such as sodium chloride,[176] or oxidizing the metallic substrate.[166] These experiments were not conducted in the work described herein. They are recommended for future researchers to continue this line of inquiry, though dragging 2-dimensional structures by scanning probe tip-manipulation is not feasible and oxidizing the underlying metal substrate could pose problems due to high likelihood of undesired oxidation of the radical centers as well.

1.5 Polyradical graphene nanoribbons

While work focused primarily on networking nanographenes in two dimensions through a σ-bonding framework, secondary projects target networking radical sites in one dimension mediated by a graphitic structure, the graphene nanoribbon (GNR). This work expands on the discovery of a technique for inducing metallicity in GNRs[98] as well as a rich body of research on PAH polyradicals and polyradicaloids.[78,81,177–180] Synthesizing periodic polyradicals of high degree in solution would represent a massive leap in the field of polyradical(oid) chemistry that has progressed gradually from the study of diradicals to tetraradicals to hexaradicals.

1.5.1 Graphene nanoribbons and their synthesis

Graphene nanoribbons are narrow, quasi-1-dimensional strips of graphene, flat cousins of carbon nanotubes. The zigzag and armchair edge structure of GNRs was described in **Section 1.2.1**. GNRs can be synthesized using top-down methods such as lithographically[181] or chemically[182–184] etching graphene or unzipping carbon nanotubes. [185,186] However, these methods do not produce GNRs with uniform or pristine widths and edge geometries, which properties have a powerful deterministic effect on the electronic properties of the GNRs.[187–193] For applications to be viable, it is therefore desirable to reliably produce GNRs with atomically precise widths and edge morphologies. Bottom-up methods for synthesizing GNRs are therefore preferable. In bottom-up synthesis, a small molecule precursor monomer is synthesized, polymerized, and then graphitized into the final GNR structure. Polymerization and graphitization can take place at a metal surface or in solution.[11,194,195] Monomer synthesis is achieved using traditional organic synthetic methods.

1.5.2 Inducing metallicity in graphene nanoribbons

It was found in our group that by evenly spacing an extra A-sublattice carbon atom per unit cell, metallicity could be achieved due to the equivalency between hopping parameters t_1 and t_2.[98] It was further found that five-membered ring formation caused sublattice mixing that broadened the metallic band. This informed a design principle that evenly spaced zero modes in a GNR leads to the formation of a metallic band, whereas unevenly spaced zero modes causes hybridization into a valence and conduction band, as described by the Su-Shrieffer-Heeger (SSH) model.[196]

Metallic graphene nanoribbons are desirable because contacting semiconducting GNRs has proven a challenge in the field due to the Schottky barrier.[197–199] Designing a metallic graphene nanoribbon for intimate graphitic integration is desirable for the realization of molecular electronics. In our group, achieving a regioregular metallic 9-AGNR (**Figure 1.9**) has been attempted repeatedly with no success. Routes to achieving the five-membered ring involving cyclodehydrogenation with a pendant methyl group have yielded defective and cross-linked ribbons. In the synthesis described herein, a fluorene moiety was preinstalled with closed five-membered ring and a pre-formed polymer was deposited on the surface using matrix-assisted direct contact transfer (MAD). The GNR was furthermore designed with aryl protecting groups that solubilize the ribbon in solution and kinetically stabilize the sites of localized radical density for solution-state characterization experiments.

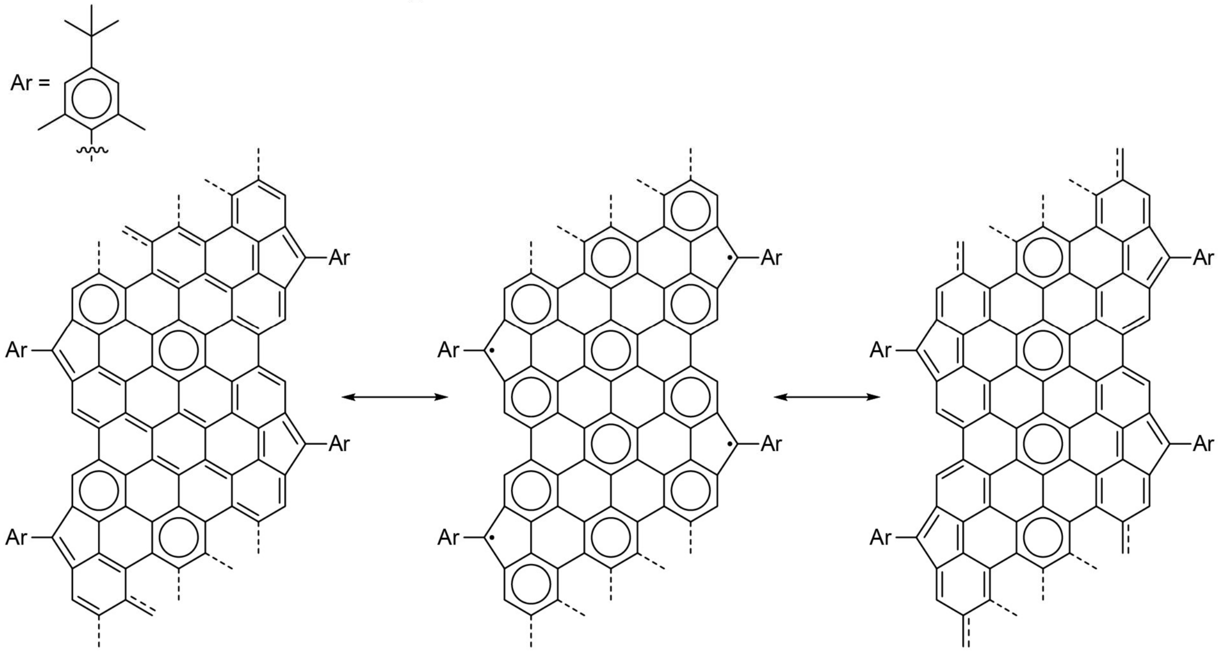

Figure 1.9 Resonance structures of metallic 9-AGNR

1.5.3 Polyradical GNRs: hybrid solution/on-surface studies

Due to π-stacking interactions and large, flat, extended geometry, GNRs are highly insoluble. Incorporating solubilizing groups and prolonged sonication can be effective ways to disperse GNRs in solution in some cases, but oftentimes, aggregation dominates, especially on long enough time scales. Solubilizing GNRs for long enough to do chemical reactions and gather ensemble measurements, such as electron spin resonance (ESR) spectroscopy is a worthwhile endeavor because in concert with powerful characterization provided by scanning probe techniques, a rich understanding of the physics of the system can be developed.

In addition to the solubilized metallic 9-AGNRs project, with the assistance of an undergraduate assistant, Maggie Khoury, synthesis towards a polyradical GNR with *m*-indenofluorene moiety periodically positioned along each edge was developed (**Figure 1.10**). Indenofluorenes are a class of PAHs, with three possible configurations: *ortho*-, *meta*-, and *para*-, with *o*- and *p*-indenofluorenes closed-shell and *m*-indenofluorenes open-shell with relatively high biradical character ($y_0 = 0.68$).[200,201] This structure would likewise be interesting to study in solution as the logical conclusion of the direction of study in current inquiries of polyradicaloids.

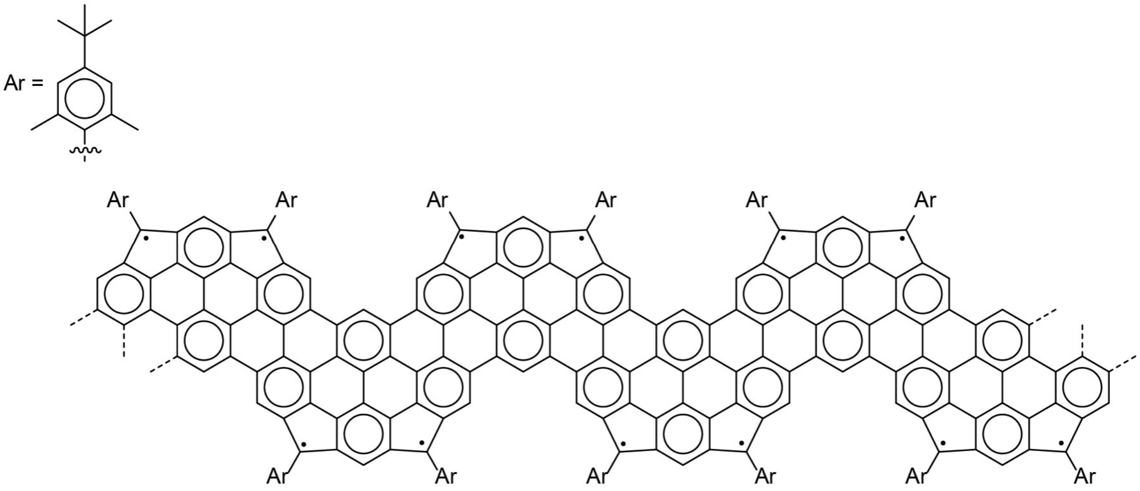

Figure 1.10 Chemical structure of *m*-indenofluorene-GNR

1.6 0-D spin systems

In addition to the 2-dimensional networks and 1-dimensional chains that were targeted and synthesized, there were some small efforts to generate interesting 0-dimensional spin systems. Neither project was completed, but perhaps can serve as inspiration to another synthetic chemist to target these fascinating structures.

1.6.1 Biphenalenyl: interest and applications

While targeting **poly-2T** and researching the history of phenalenyl and related materials, it was noticed that 2,2’-biphenalenyl had never been synthesized. While this system was ultimately generated and characterized in the on-surface synthesis of **poly-2T** described herein, prior to that achievement, we planned a synthesis for a kinetically stabilized 5,5’,8,8’-tetra-*t*-butyl-[2,2’-biphenalenyl] (**^{t}Bu$_4$-bi-2T**) (**Figure 1.11**) that remains as an attainable product. ESR characterization of bi-2T **^{t}Bu$_4$-bi-2T** will provide valuable data in the structure of the biradical in solution state. On-surface, the molecule maintains a planar geometry, but in solution, orthogonal alignment of the two **2T** units is likely the lowest energy state geometrically, which would inhibit orbital overlap and change the physics of the system. It may not be possible to determine the true geometry of the system in solution but following the standard practices of biradical chemistry and previous studies of **2T**, it would be interesting to grow a crystal of the biradical material to analyze the geometry in the crystalline state. Study of this biradical would provide additional insight alongside the STM/STS data gathered on **poly-2T**. The results of such work could have impactful implications on the fields of organic electronics and qubit research.

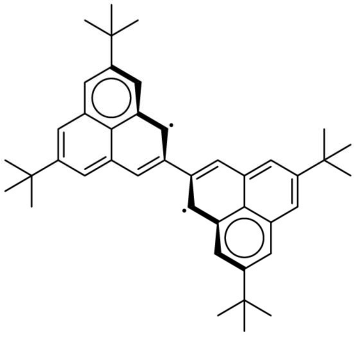

Figure 1.11 Chemical structure of 5,5’,8,8’-tetra-*t*-butyl[2,2’-bi[2]triangulene]

1.6.2 Nitrogen vacancy center: interest and applications

Nitrogen vacancy (NV) centers are a defect in diamond in which a nitrogen atom incorporates into the diamond structure and the nitrogen's lone pair precludes a carbon atom from filling an adjacent lattice site.[202] This causes three dangling bonds, two electrons of which pair up into a singlet bonding-like state and the remaining radical gives the structure an overall doublet spin. NV centers are a hot area of research right now, and currently they are generated by grinding diamond into extremely fine powders. In the project described herein, we targeted the smallest functional unit of an NV center for bottom-up synthesis, a highly cyclic molecule with a nitrogen bonded to three cyclohexane units of a trisubstituted tetracycloheneiocasane (**Figure 1.12**). Unlike GNR precursors, however, the NV-center has a 3-dimensional structure; not a mostly-2-dimensional PAH, like the rest of our monomers. Attempts to synthesize the molecule required a broader reaction scope and techniques not commonly used in our group. Ultimately a route was chosen, but quickly proved to be too challenging to justify the focus and effort required. Once again, we would be fascinated to see another chemist with sufficient drive, motivation, and funding inspect this system further and bring it to reality. Bottom-up synthesized NV centers could provide powerful hyperpolarization reagents to amplify NMR signals as well as useful magnetic polarization reagents in a whole of research fields.

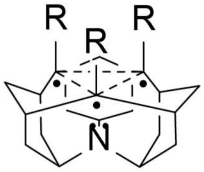

Figure 1.12 Target structure for smallest functional unit of a nitrogen-vacancy center

1.7 Summary

In short, the work contained herein can be broadly described as an interrogation of low-dimensional all-carbon polyradical and polyradicaloid materials. The benefits of all-carbon materials for spintronic applications are: low spin-orbit coupling, low interference from nuclear spins, and a thermodynamically flat energy landscape for electrons. The bottom-up synthesis approach provides a toolkit that has been developed by over a hundred years of synthetic exploration, atomic precision of target structures, abundant feedstocks, and good scalability. This work coincides with rising interest in alternatives to silicon logic technology as well as alternatives to semiconductor logic technology. The exploration of magnetic carbon nanomaterials as a technological advancement provides the potential for a massive leap in computing speed, energy efficiency, and environmental sustainability.

2 Phenalenyl, *S* = ½ supergraphenes and superpolyacetylenes

2.1 Abstract

Phenalenyl is the smallest open-shell, alternant hydrocarbon. It was hypothesized in the ‘40s, measured transiently in the ‘50s, kinetically stabilized and studied in solution in 1999, and has received intermittent interest in various studies of open-shell materials in the early twenty-first century. In the context of broader research in the triangulene class of molecules, phenalenyl has recently been dubbed [2]triangulene (**2T**) for systematic reasons. In this work, we targeted 2-dimensional networks of **2T** with the objective of achieving a spin-supergraphene. A divergent synthesis to the 1-dimensional chains of **2T** targeting spin-superpolyacetylenes was also completed. The initial target monomer precursor to [2]triangulene-supergraphene (**2T-sg**) was achieved in four steps with a divergence to the monomer precursor to [2]triangulene-superpolyacetylene (**2T-sp**) in three steps overall. A concise route to the phenalenone core, along with pre-installation of bromine in a strategic position allowed for a direct and highly modular synthesis of a range of **2T** supergraphenes and superpolyacetylenes. These materials were predicted to be antiferromagnetically ordered due to topological frustration precluding a closed-shell structure and Lieb’s theorem for the net spin of nanographenes. Though the full range of modular materials was not achieved, those that were generated and characterized provided a strong starting point for the study of this class of materials. Notably, poly([2]triangulene-2,5-diyl) (**poly-2T**), the base **2T-sp** demonstrated a surprising violation of topological frustration, forming an emergent metallic band via a four-center, two-electron, third-nearest neighbor hopping interaction with δ-bond symmetry between four non-adjacent carbon atoms and a σ-bond framework.

2.2 Phenalenyl

The open-shell nature of **2T** is well understood from its long history of inquiry. At the Hückel molecular orbital theory (HMOT) level, the thirteen carbon p-orbitals generate thirteen π molecular orbitals, six bonding, six antibonding, and one nonbonding. The nonbonding orbital is localized on the six α-carbons on the periphery of the molecule (**Figure 2.1A,B**) (note, these are A lattice sites by Lieb’s theorem), with no density on the β-carbons (peripheral B lattice sites by Lieb’s theorem).[110] Historically the edge carbons and apical carbons have been referred to as α-sites and β-sites, respectively. To avoid confusion, modern parlance “edge” and “apex” will be used. Because the nonbonding orbital lies at the α-level (zero of energy scale) on the MO diagram, **2T** exists as a relatively stable cation and anion in addition to its radical state—the only extra energy penalties for increased electron count are the kinetic energy of the additional electron(s) and the added coulomb repulsions; there is no additional stabilization or destabilization from filling a bonding or antibonding orbital. Curiously, the seventh hypothetical resonance structure for the phenalenyl radical, which places the radical on the central carbon (also an A site, by Lieb’s theorem) has zero contribution to the resonance hybrid, which can be understood because this would generate a 12π-electron antiaromatic system in the peripheral ring of the molecule. The unrestricted density-functional theory (UDFT) level predicts the same spatial distribution of the singly occupied molecular orbital (SOMO) as HMOT predicts for the nonbonding state (**Figure 2.1C**).[203] These theoretical results are supported by electron spin resonance measurements on unsubstituted **2T**, as well as on 2,5,8-tri-*t*-butyl-[2]triangulene (**Figure 2.1D**).[104,106]

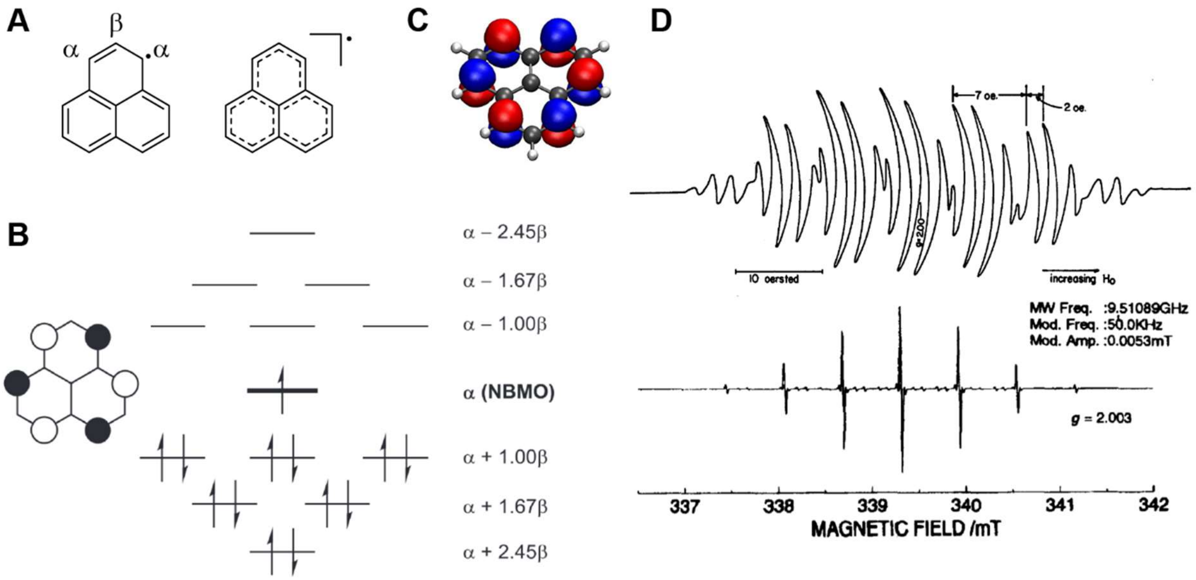

Figure 2.1 (A) One resonance structure of **2T** with α- and β-carbons labeled, resonance hybrid structure of **2T**; **(B)** Hückel molecular orbital diagram with corresponding prediction of spatial distribution of the non-bonding molecular orbital;**[110]** **(C)** unrestricted density functional theory electron density simulation of the singly occupied molecular orbital;**[203]** **(D)** Electron spin resonance spectra of unsubstituted (top) and 2,5,8-tri-*t*-butl[2]triangulene (bottom)**[104,106]**

Although unsubstituted **2T** was characterized by STM/STS in this work, while our work was under review, other researchers concomitantly posted a preprint of characterization and analysis of lone **2T** generated by the same method as Pavliček *et. al.* for generating **3T** at the vacuum-metal interface in 2017.[68,102] This analysis gives direct characterization of the SOMO and singly unoccupied molecular orbital (SUMO) by virtue of the positive ion resonance (PIR) and negative ion resonance (NIR), respectively.

It was hypothesized that polymerizing **2T** by a σ-bond framework through the apical carbons, which bear no spin density would inhibit spin-quenching by radical recombination and generate a polyradical material (due to topological frustration) with an antiferromagnetic ground state (by Lieb's theorem). The proposed structures are expected to be highly oxidizable and would likely cross-link in solution, thus this synthesis was proposed at the vacuum-metal interface only. While planning the synthesis of the monomer precursor to **2T**-supergraphene (**2T-sg**), it was observed that the corresponding **2T**-superpolyacetylene (**2T-sp**) analogues were likewise achievable by diverging from a common intermediate and would provide an interesting insight into the progression from 0-D to 1-D to 2-D spin structure. The significant differences in physical properties of graphene and polyacetylene make it clear that the properties of the 2-D structure cannot be extrapolated from those of the 1-D or vice versa. Furthermore, these represent fascinating targets: a spin supergraphene and a 1-dimensional all-carbon Heisenberg spin-½ chain. It was also hypothesized that the Hubbard hopping parameter, *t*, could be modulated by inserting linking moieties between **2T** units to form a series of alternating copolymers and 2-D covalent organic frameworks (COFs). It was further hypothesized that tuning the Hubbard on-site repulsion energy, *U*, would be possible by modulating the underlying substrate, though these experiments were not achieved in the course of this work and remain for future experimentalists.

While the physics of **2T** instructed the design of desirable materials properties, synthesis of the desired structures was not trivial. To synthesize the desired monomers, it is important to know the chemistry of precursors to **2T**: phenalene and phenalenone. Reid gave a useful insight on the synthetic aspect of these molecules in addition to the physics in a 1965 review.[107] While there have been useful advancements in some aspects since then, this early review provides useful for understanding the chemical transformations of related compounds and the energetics of the phenalenyl cation/radical/anion system. The key method for achieving the desired **2T** structures is the generation of precursor phenalenes. When planning the project, it was hypothesized that a voltage pulse from the STM tip could abstract a hydrogen atom, yielding the desired **2T**, but it was found during experiments that the transformation could be achieved thermally. Phenalenes can be generated from their corresponding phenalenones by an aluminum hydride reduction. Early reports of this transformation were highly variable and a reliable improvement was published in 1978.[204] The hydride reduction of phenalenone yields phenalenol, an unstable molecule that exists in the air-free, water-free reaction mixture, but upon addition of protic solvents undergoes disproportionation wherein one phenalenol acts as a hydride reagent and further reduces another phenalenol, yielding one phenalene and one phenalenone. The hydride reduction of phenalenone into phenalene therefore has a 50% theoretical yield, with 50% of starting material being converted to phenalenol and reverted to phenalenone during workup (**Figure 2.2A**). To generate the precursor phenalenones, a concise method for double-condensation-elimination was used (**Figure 2.2B**).[205–207]

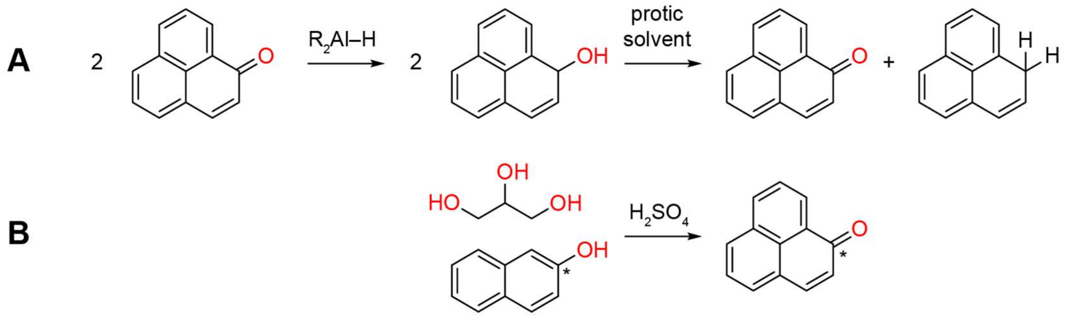

Figure 2.2 Useful reactions of phenalenones: **(A)** aluminum hydride reduction of phenalenone to phenalenol and subsequent disproportionation into phenalenone and phenalene; **(B)** double-condensation-elimination route to phenalenone from naphthol and glycerol (* indicates positional equivalency)

In this chapter will be discussed the successful synthesis of precursor monomers to on-surface synthesis of **2T-sp**s with no linker, biphenyl linker, ethynyl linker, and phenyl linker. Synthesis of the monomer precursor to **2T-sg** with no linker was nearly achieved, but time constraints prevented its ultimate synthesis, though the method for its generation was determined.

2.3 Monomer design and modular synthesis

Monomer precursors to **2T-sg** and **2T-sp** were targeted by synthesis of the corresponding dibromo- and tribromo-phenalenes (**2-1** and **2-2**), respectively (**Figure 2.3**). Making use the workhorse of on-surface synthesis (OSS), the surface-assisted Ullman-like coupling of aryl halides, these monomers were expected to grow into the corresponding 1-D and 2-D lattices, with subsequent hydrogen atom abstraction leading to the target polyradical structures.

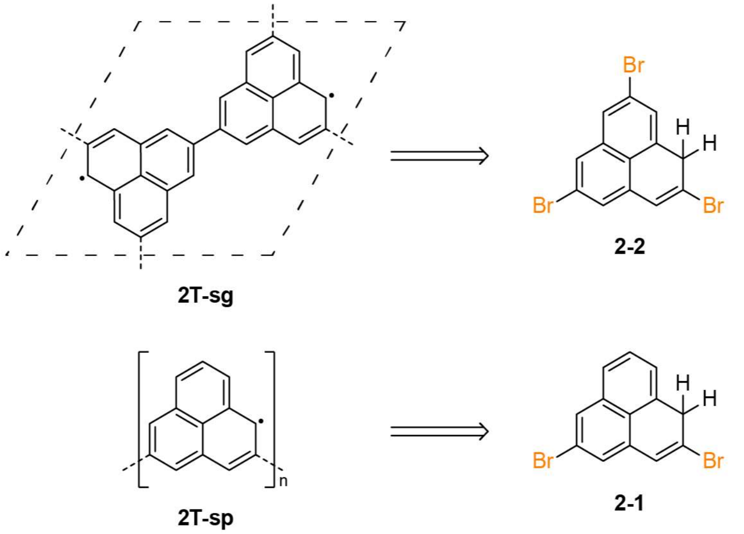

Figure 2.3 Retrosynthesis of **2T**-supergraphene and **2T**-superpolyacetylene from tribromo- and dibromo-phenalenes

The synthesis of the phenalenone core was achieved in one step from 6-bromo-naphthol where the naphthol has preinstalled a bromide in a position that would be otherwise difficult to brominate on the phenalenone structure. Other routes to substituted phenalenones use multistep syntheses to install the desired groups via a 3-(1-naphthyl)propionic acid before invoking a Friedel-Crafts ring closure to achieve the tricyclic core.[102,103] Though they do have advantages, these syntheses were incompatible with regioselectively installing bromide functionality in the desired monomer here. Drawbacks to the synthesis described herein include: poor solubility of phenalenones, especially with each additional bromination, poor regioselectivity of bromide substitution at the 8-position, and 50% theoretical yield of phenalenes from phenalenones due to disproportionation.

Monomer precursor **2-2** was synthesized in four steps from commercial materials (**Scheme 2.1**). Precursor **2-1** was achieved in a divergent synthesis in three steps total. The prebrominated phenalenone core, 5-bromophenalenone (**2-3**) was generated by a double-condensation-elimination of 6-bromo-2-naphthol with glycerol. Electrophilic addition of bromine followed by $E1_{cb}$ β-elimination yielded 2,5-dibromophenalenone (**2-4**). Forcing conditions were required to electrophilically brominate the 8-position, yielding 2,5,8-tribromophenalenone (**2-5**) in poor yield due to poor regioselectivity. DIBAL-H reduction of phenalenones **2-4** and **2-5** followed by air-free workup and purification yielded corresponding phenalenes **2-1** and **2-2** in modest yields.

It was found that forcing conditions to brominate the 8-position of 2,5-dibromophenalenone (**2-4**) inevitably led to the formation of 2,5,8,9-tetrabromophenalenone, an undesired byproduct resulting from the relatively facile substitution at the 9-position of phenalenone, which was impossible to separate by column chromatography due to similar retention factor to the desired 2,5,8-tribromophenalenone (**2-5**) and extremely low solubility of these compounds. Instead, the diversion in synthesis was performed one step earlier and the forcing bromination conditions were applied to 5-bromophenalenone (**2-3**). The yield of desired 5,8-dibromophenalenone (**2-4a**) was poor, but it separated easily from the starting material and the dominant byproduct, 2,5-dibromophenalenone (**2-4**), which unfortunately could not be recovered due to its contamination with 9-substituted analogues. After purifying 5,8-dibromophenalenone (**2-4a**), addition-elimination bromination yielded 2,5,8-tribromophenalenone (**2-5**), which despite extremely poor solubility, was able to be separated from unconverted starting material by column chromatography, yielding 2,5,8-tribromophenalenone (**2-5**) in high purity.

Finally, DIBAL-H reduction of phenalenones yields the corresponding phenalene in a theoretical yield of 50% molar conversion due to the disproportionation mechanism (**Figure 2.2B**). Reduction of 2,5-dibromophenalenone (**2-4**) was carried out using Schlenk technique, including workup and purification by column chromatography to maintain an inert atmosphere around the air-sensitive product, the three dibromophenalene regioisomers (**Figure 2.4**). The three regioisomers, **2-1a**, **2-1b**, **2-1c**, were obtained in approximately 10:10:1 ratio, determined by integral analysis of NMR spectra. This was rationalized using an electronic argument: the carbons neighboring a bromide-substituted carbon are more electrophilic by induction, lowering the energy barrier for hydride reduction at that site. DIBAL-H reduction of 2,5,8-tribromophenalenone (**2-5**) was carried out in a single attempt, but due to time constraints, was completed using minimal starting material and could not be adequately analyzed or purified. Furthermore, the analysis and purification of this trial was carried out in a nitrogen glovebox. In retrospect, the residual trace oxygen in the glovebox likely prevented attempts to purify and analyze desired product 2,5,8-tribromophenalene (**2-2**). In the future, the glovebox can be a useful tool to permit thin layer chromatography analysis and preparation of air-free NMR samples, but the superior oxygen exclusion of Schlenk technique is preferential for the air-free column chromatographic purification.

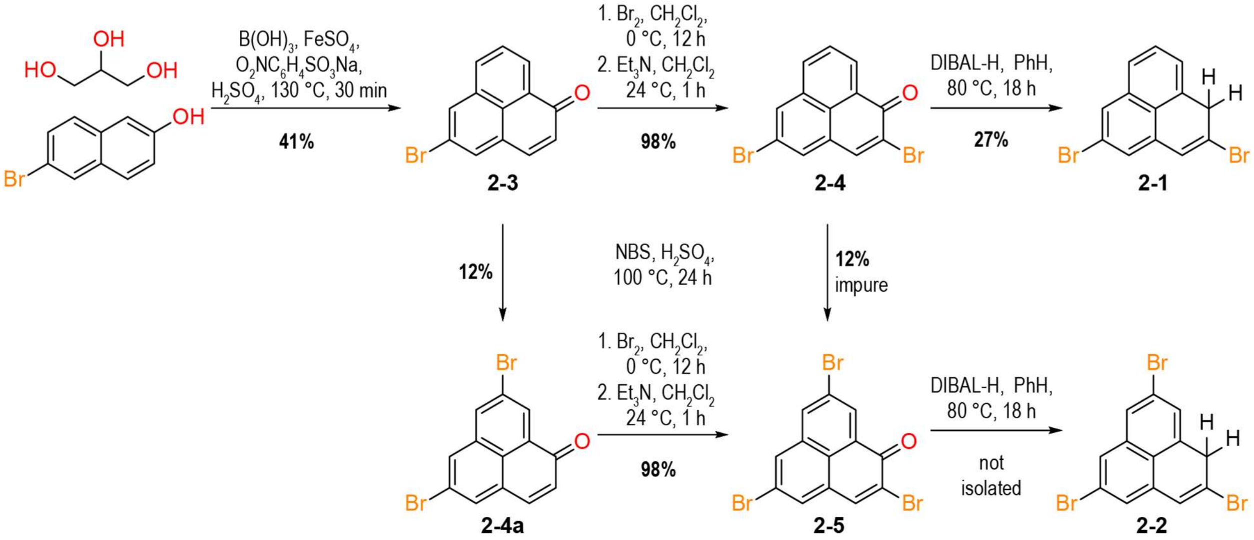

Scheme 2.1 Synthetic route to 2,5-dibromophenalene (**2-1**) and 2,5,8-tribromophenalene (**2-2**)

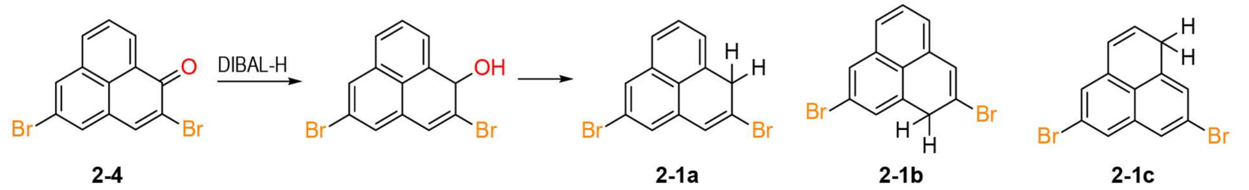

Figure 2.4 Regioisomers of dibromophenalene (**2-1**) resulting from the disproportionation of 2,5-dibromophenalenol resulting from the DIBAL-H reduction of 2,5-dibromophenalenone (**2-4**)

The bromide functionalities of 2,5-dibromo- and 2,5,8-tribromophenalenone serve as coupling handles for Ullman-like coupling on the surface after reduction to their corresponding phenalenes. This functionality furthermore permits the highly divergent synthesis to achieve a range of carbon superstructures by using the bromide handles for solution-phase cross-coupling of linker moieties.

Using this strategy, precursor monomers towards alkyne-linked, phenyl-link, and biphenyl-linked structures could be synthesized (precursors **Figure 2.5**, structures **Figure 2.6**).

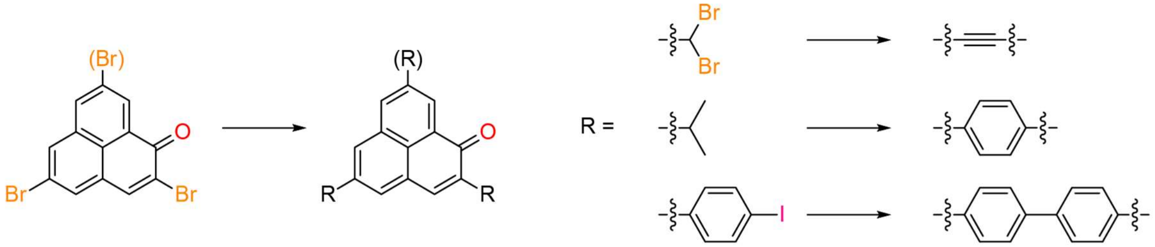

Figure 2.5 Modularly accessible bis- and tris- dibromomethyl, isopropyl, and 4-iodophenyl phenalenone monomer precursors, which provide on-surface synthesis routes to alkyne-, phenyl-, and biphenyl-linked superstructures

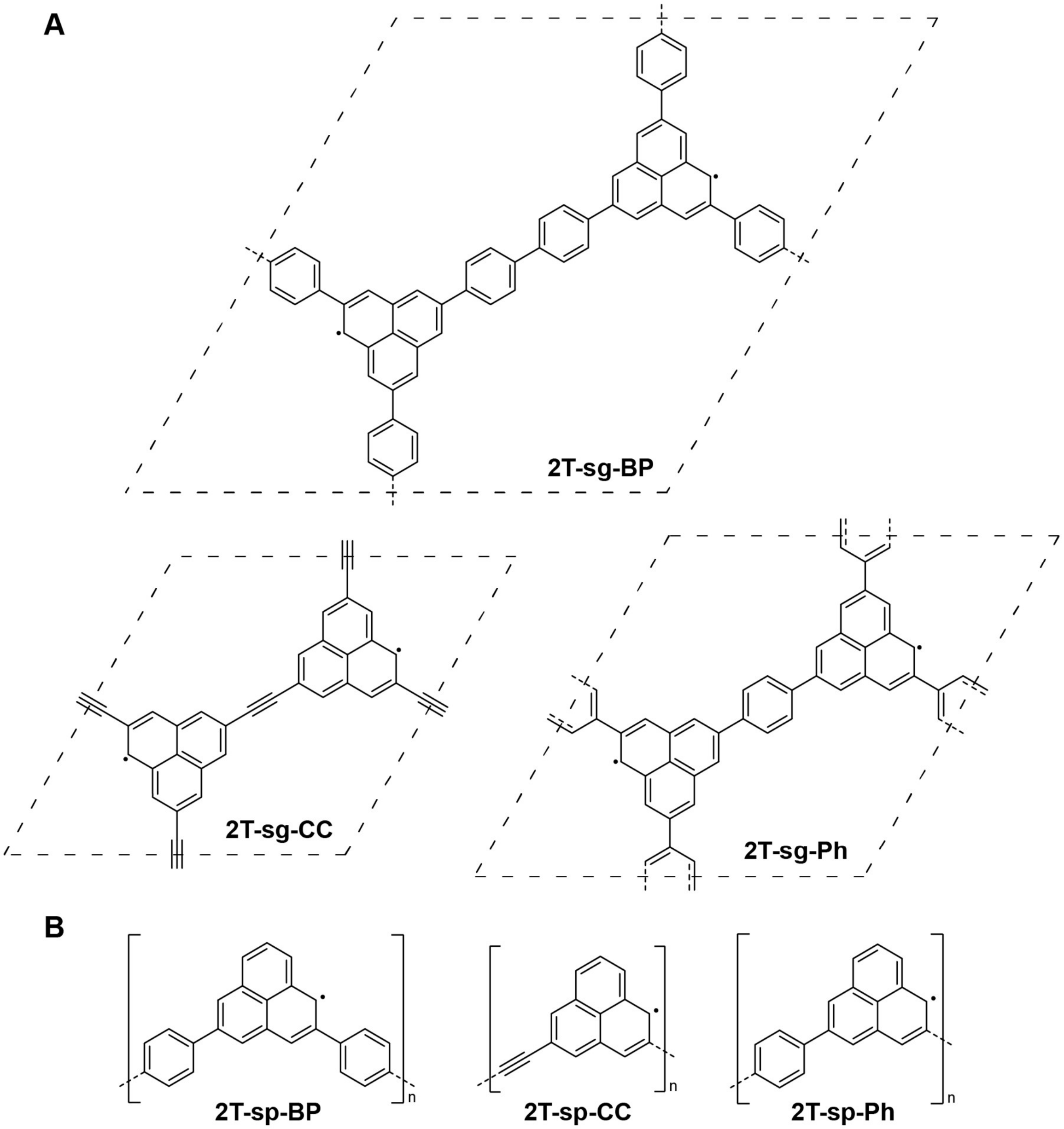

Figure 2.6 divergent **2T** supergraphene **(A)** and superpolyacetylene **(B)** structures accessible from intermediate **1-1**

Initial targets for modular 1-D and 2-D covalent organic frameworks (COFs) were limited to those with 1,1’-biphenyl-4,4’-diyl linker (**Figure 2.6**, **2T-sg-BP** and **2T-sp-BP**) due to symmetry requirements and the restriction to Ullman-like coupling on the surface. New developments in the science of OSS during the course of these projects, however, rendered possible new target superstructures, specifically alkynyl-linked structures and phenyl-linked structures (**Figure 2.6**). Note that due to the extreme insolubility of 2,5,8-tribromophenalenone (**2-2**), modular **2T-sp**s (**Figure 2.6B**) were targeted first as proof of concept for the on-surface coupling reactions between these species. The discussion of the 1-D chains will therefore be the focus for now.

The generation of [2]triangulene-superpolyacetylene with biphenyl linker (**Figure 2.6B, 2T-sp-BP**) was targeted by replacing the bromide cross-coupling handle with a 4-iodophenyl moiety (**Scheme 2.2**). This was achieved by Suzuki coupling using a masked halide on a phenylboronic ester coupling partner. First, 4-iodoaniline was converted to the corresponding dialkyl triazene, 1-(4-iodophenylazo)pyrrolidine (**2-6**) using Sandmeyer-like conditions. The iodide, **2-6**, was converted to the corresponding boronic ester via an organometallic intermediate to generate N-pyrrolidinyl-4-phenyl-azo-boronic acid neopentyl glycol ester (**2-7**). Two equivalents of boronic ester **2-7** were then used in a Suzuki coupling with dibromide **2-4**, generating bisphenyl derivative, **2-8**, in surprisingly high 85% yield for a double Suzuki reaction. Unmasking the triazenyl moiety using methyl iodide in a sealed flask at 100 °C yielded the desired product, 2,5-bis(4-iodophenyl)phenalenone (**BP-2-1**). Reduction to the corresponding phenalene was not performed because developments in the OSS literature led us to believe that the reduction could be performed on-surface using cracked hydrogen after generating polymers of the phenalenone species. This technique did succeed for this system (**Section 2.4**).

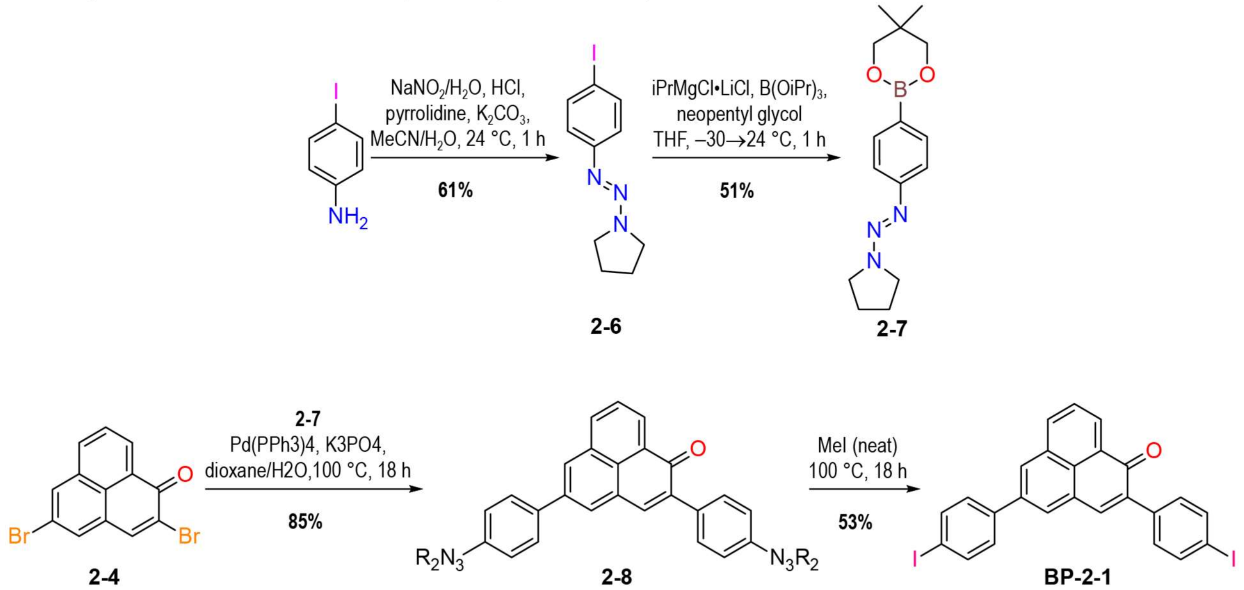

Scheme 2.2 Synthesis of 2,5-bis(4-iodophenyl)phenalenone, precursor to 1-dimensional, biphenyl-linked **2T-sp**

During synthesis of monomers **2-1** and **BP-2-1**, researchers published a technique for the OSS of alkynes from trihalomethylated precursors.[208] This technique was employed to target [2]triangulene superpolyacetylene with ethynyl linker (**Figure 2.6B**, **2T-sp-CC**). On paper, the synthesis of 2,5-bis(dibromomethyl)phenalenone was facile. First, 2,5-dibromophenalenone, **2-4**, was subjected to double Suzuki coupling using trimethyl boroxine to generate 2,5-dimethylphenalenone (**2-9**) in good yield. Benzylic bromination using a radical initiator and N-bromosuccinimide as bromine source, however, did not lead to the desired bis-tribromomethylated product. Instead, 2,5-bis(dibromomethyl)phenalenone (**CC-2-1**) was formed as the most brominated product. Increasing the time, temperature, or equivalents of bromine in the reaction did not appear to drive tribromination of the methyl groups but did result in diminished yields. It is possible that substituting the fifth and sixth bromines was indeed possible, and that this reaction led not to an unstable product, but rather one that became invisible to the characterization techniques used (mass spectrometry and thin layer chromatography), however we were ultimately unable to confirm its formation. We hypothesized that the bis(dibromomethyl) species, **CC-2-1**, could still lead to ethynyl-linked structures if heated to sufficiently oxidize the as-formed alkene to the subsequent alkyne. Regardless, the ethenyl-linked spin chain would provide an interesting data point as well. As above, we also intended to attempt an on-surface reduction to the corresponding phenalene, although we are wary of potential side reaction in additionally reducing the alkyne bonds,

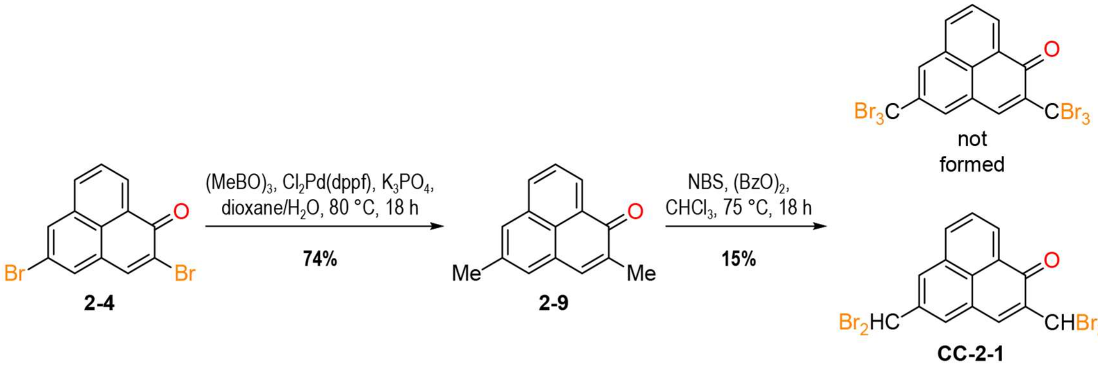

Scheme 2.3 Synthesis of 2,5-bis(dibromomethyl)phenalenone, precursor to 1-dimensional, ethynyl-linked **2T-sp**

The final target modular monomer was designed after a 2022 report of on-surface cycloaromatization between isopropyl substituents.[209] This technique required the isopropyl substitution to occur in a position from which undesired five-membered ring formation was not possible, which fortunately was the case for the **2T-sp** system. Repeated attempts were made to Negishi couple isopropyl groups onto 2,5-dibromophenalenone, **2-4**, since Suzuki coupling of isopropyl substituents is known to work poorly or not at all. Negishi coupling could not be driven either, however, due to the presence of the electrophilic ketone functionality and the ability of phenalenone to undergo conjugate 1,4-, 1,6-, and 1,8-addition on top of standard 1,2-nucleophilic addition. Conditions using CPhos were used to promote cross-coupling over nucleophilic addition which reportedly worked for 2-bromobenzonitrile and 2-bromobenzaldehyde, among other phenyl bromides with electrophilic functionality. This technique did not, however, work for the bromophenalenone system. Instead, a reroute was planned using the initial logic of generating the 5-bromophenalenone (**2-3**) system of pre-installing functionality before performing the double-condensation elimination to form the phenalenone core in one step (**Figure 2.2B**).

To synthesize a diisopyopylated, phenalenone, in pursuit of a [2]triangulene-superpolyacetylene with phenyl linker (**2T-sp-Ph**), a 5,8-substitution pattern was chosen instead. Target monomer 5,8-diisopropylphenalenone (**Ph-2-1**) was synthesized by first generating an isopropylated glycerol, 2-isopropyl-propane-1,2,3-triol (**2-11**). This was achieved generating a *t*-butyl-dimethylsilyl-protected 1,3dihydroxyacetone (**2-10**) from commercially available dihydroxyacetone dimer. The protected dihydroxyacetone was subjected to nucleophilic substitution using two equivalents of an isopropyl Grignard reagent before acid workup and TBAF deprotection. Note: the literature preparation for the isobutyl analogue calls for a TMS-protected dihydroxyacetone. This mistake might account for the poor yield of **2-11**. The glycerol derivative,

2-11, was also synthesized via another protected dihydroxyacetone, 2,2-didmethyl-1,3-dioxan-5-one. Commercial starting material 6-bromo-2-naphthol was used to generate 6-isopropyl-2-naphthol in a Kumada coupling in favorable yield. Finally, the isopropylated glycerol and isopropylated naphthol were condensed into 5,8-diisopropylphenalenone (**Ph-2-1**) in yield similar to the first attempts to synthesizing 5-bromo-phenalenone, which was later improved up to 41%. It is also possible that the alkylated glycerol interferes with the elimination reaction, causing the decreased yield. On-surface reduction of phenalenones was likewise planned for this monomer.

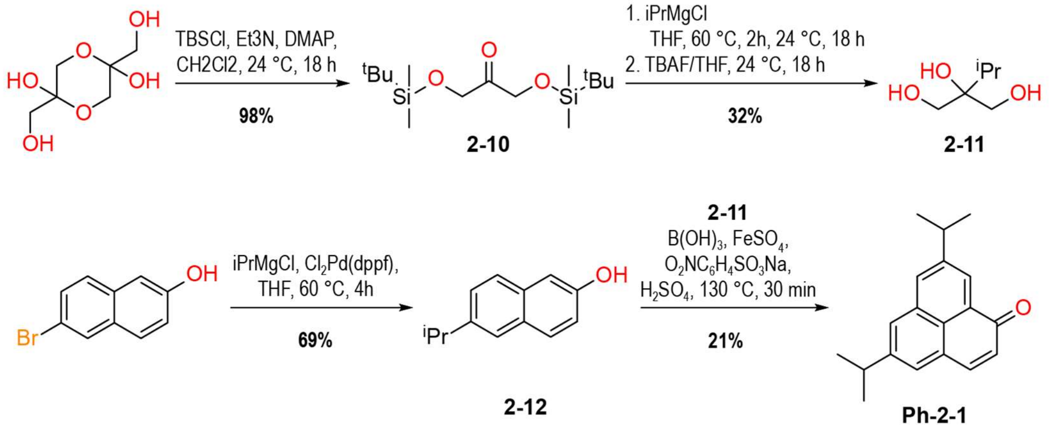

Scheme 2.4 Synthesis of 5,8-diisopropylphenalenone, precursor to 1-dimensional, phenyl-linked **2T-sp**

A solution synthesis of an alternating copolymer of phenalenone-2,5-diyl and 1,4-phenylene was also completed for matrix-assisted direct contact (MAD) transfer to the gold STM substrate. This material was achieved by Suzuki polymerization between 2,5-dibromophenalenone and benzene 1,4-diboronic acid bispinacol ester. The presence of the desired polymer was confirmed by matrix-assisted laser-desorption ionization mass spectrometry, however the purity of the sample was indeterminate due to its extreme insolubility. Furthermore, due to the sensitivity of MAD transfer to polymer type, STM operators prefer evaporable samples when possible.

2.4 Superpolyacetylenes: growth and characterization

With target **2T-sp** precursors in hand, on-surface growths on a Au(111) were performed in the STM. The general mechanism for the Ullman-like on-surface cross-coupling mechanism is: homolytic cleavage of halide bonds, diffusion of surface-stabilized radicals, and recombination of carbon-centered radicals to form σ-bonds. It was predicted that STM tip manipulation would be required to provide a voltage pulse to homolytically cleave the C–H bond at the methylene functionality of phenalene units to activate them to the corresponding **2T** unit, but this hydrogen atom dissociation was found to happen spontaneously—no intact methylene units were observed after polymerization. Finally, STM and STS characterization allowed us to map the energy landscape of the material: its bands and the presence or absence of Kondo or inelastic electron tunneling features and to map these energy states spatially. For monomers that were deposited in the phenalenone form, deposition of cracked hydrogen likewise yielded activated **2T** species and the spin-inert phenalenes were not observed.

The first experiments were performed on dibromophenalene (**2-1**, mixture of isomers, **Figure 2.4**). Monomers were evaporated from a Knudsen cell onto a Au(111) surface held at 24 °C. Annealing the metal surface to 180 °C promoted polymerization, leading to **2T-sp** chains of various lengths (**Scheme 2.1**).

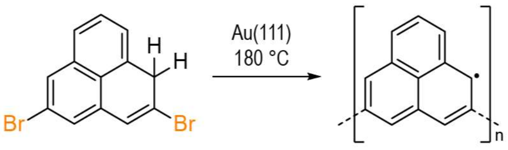

2-1 **2T-sp**

Scheme 2.5 On-surface growth of **2T-sp** from monomer precursor dibromophenalene (**2-1**)

As-deposited monomer monolayers self-assembled into two distinct phases (overview **Figure 2.7A**, closeups **Figure 2.7B,C**), which likely resulted from the two dominant regioisomers resulting from the reduction reaction (**Figure 2.4**, **2-1a,b**). After annealing to 180 °C, monomer units polymerized as desired, yielding spin-active polymer **2T-sp**. Recall that manual abstraction of hydrogen atoms using a voltage pulse from the STM tip was not required, as hypothesized.

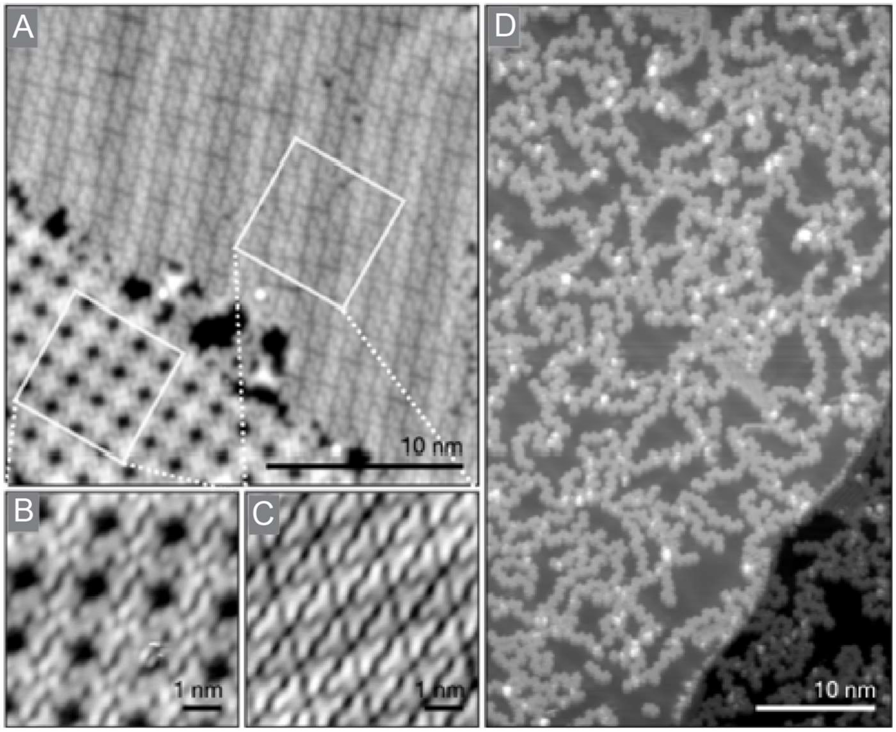

Figure 2.7 STM topographic images of deposition and growth of monomer **2-1**. **(A)** Large area image of monomer self-assembly, clearly divided into two phases; **(B)** One phase of monomer self-assembly; **(C)** Other phase of monomer self-assembly; **(D)** Networks of entangled chains that form after annealing to 180 °C

It was observed that occasional defects in chain growth led to quenching of low energy states that were apparent from analysis of topological scans. Bond-resolved STM imaging revealed that it was possible for chains to cross-couple in a corner-to-edge fashion, instead of the preferred apex-to-apex (**Figure 2.8A,B**). We hypothesize that this results from concomitant cleavage of the methylene C–H and C–Br bonds, allowing a bonding interaction to take place between an apex and an edge (**Figure 2.8B**). This furthermore brings two edges in proximity to cyclodehydrogenate, forming a five-membered ring and quenching the radical state of both [2]triangulenes through a pathway reminiscent of σ-dimerization of [2]triangulenes commonly explored in the phenalenyl literature.[109,210] Nonetheless, longer oligomers (up to eight repeat units) of pristine polymers were located and characterized. The type II defects that occurred actually provided useful for experiments because the large bandgap of type II connections means that spin-active segments separated by type II defects can be studied as isolated spin systems, thus allowing us to characterize a range of oligomer lengths.

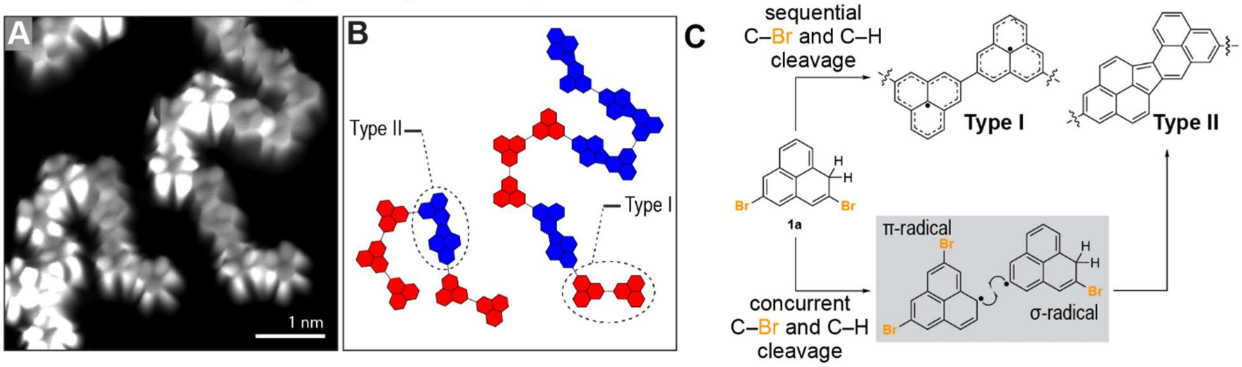

Figure 2.8 Preferred (Type I) and defective (Type II) cross-coupling between **2T** units: **(A)** STM topographic image; **(B)** Schematic diagram of panel (A); **(C)** Hypothesized mechanism for defective cross-coupling

Analysis of an isolated **2T** on the surface and a type I **2T** dimer confirm one hypothesis and reject another. As predicted, an isolated **2T** displays a Kondo resonance, typical of a magnetic impurity on the gold surface. This indicates not only that the **2T** is in the activated open-shell state with one hydrogen abstracted from the methylene site, but also that the radical electron resides in the **2T** species and is not doped into the gold by thermodynamic driving force. Imaging the species using d*I*/d*V* mapping reveals the threefold symmetric six lobes expected from the predicted distribution of the nonbonding orbital. Analyzing the **2T** dimer, however, revealed surprising behavior. We predicted either elastic electron tunneling spectroscopy (EETS) at high energy ranges, resulting from resonant tunneling through bonding modes, or otherwise we expected inelastic electron tunneling spectroscopy (IETS) at low energy ranges, resulting from the excitation of magnonic states. What we observed, however, was elastic transitions at low energy ranges (**Figure 2.9D**). The states corresponding to the elastic transitions were imaged using d*I*/d*V* mapping, revealing what appears to be a bonding-like and anti-bonding like state between adjacent **2T** units with density on non-neighboring carbons. This observation was astounding for the observation of a bonding state across 3rd-nearest-neighbor (3NN) carbons with implied δ-bond symmetry due to its being the result of a bonding/antibonding interaction formed between π systems. The phenomenon was explored more thoroughly using tight binding (TB) analysis.

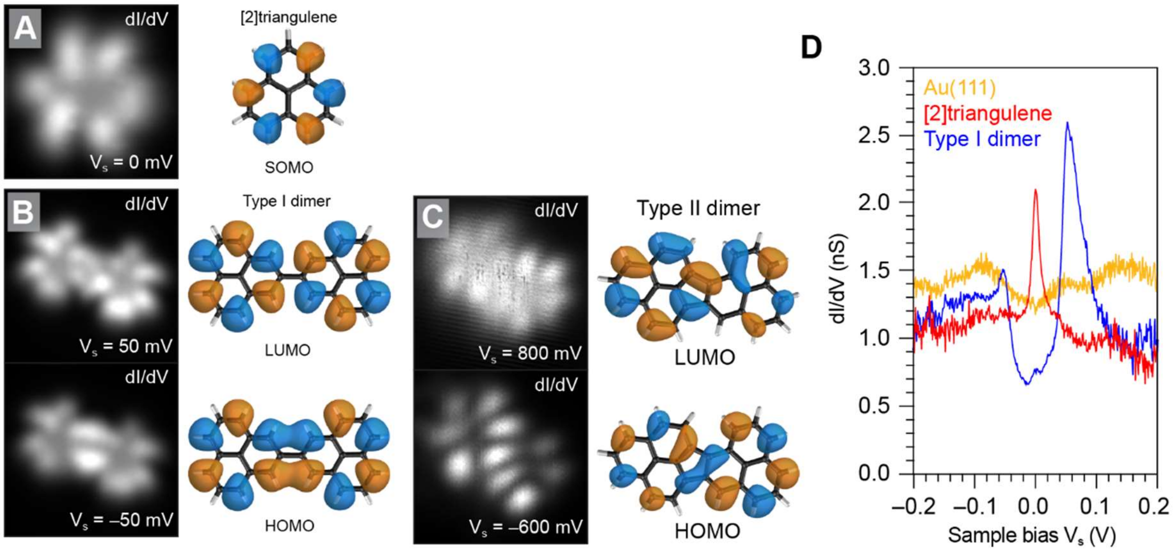

Figure 2.9 Analysis of **2T** and **2T** dimer. **(A)** STM d*I*/d*V* map of isolated **2T** on the Au(111) surface at 0 V bias and tight binding simulation of the SOMO; **(B)** STM d*I*/d*V* map of a type I **2T** dimer at the HOMO/LUMO voltages of ±50 mV and tight binding simulation of the HOMO/LUMO; **(C)** STM d*I*/d*V* map of a type II **2T** dimer at the HOMO/LUMO voltages of -600 and +800 mV and tight binding simulation of the HOMO/LUMO; **(D)** STS of lone **2T**, the type I **2T** dimer, and the gold background

Tight binding analysis initially supported the original hypothesis—antiferromagnetic orientation of spins in degenerate orbitals. Because this did not align with experimental observations, it was clear that more rigorous theoretical treatment was required. Based on the observation of the 3NN hybridization behavior that was observed (i.e. bonding and anti-bonding combinations of molecular orbitals), a 3NN hopping parameter, t_3, was added to the TB model. The 3NN hopping parameter has only a small change on **2T**, lifting the degeneracy of the HOMOs and LUMOs, while leaving the SOMO at zero energy. For the type I dimer, however, the degeneracy of the SOMOs is lifted. In addition to the standard literature value of t_1 (–2.7 eV) for graphene, the magnitude of t_3 (–150 meV) was chosen such that the TB model fit the experimental observations. This model was further validated by comparing experimental observations with modeled behavior for longer oligomers. Note that the 3NN TB model also accounts for the large-gap closed shell behavior of the type II **2T** dimer that was also observed in STM experiments.

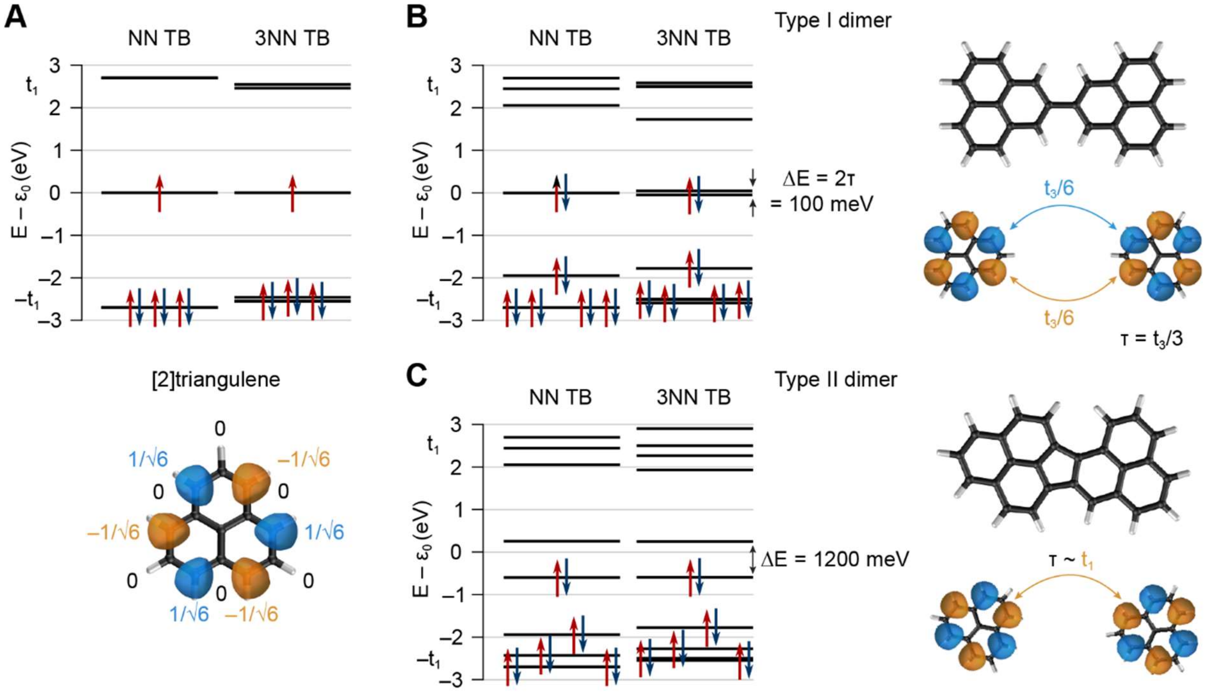

Figure 2.10 Tight binding model using nearest neighbor and 3rd nearest neighbor terms to model the molecular orbitals of (A) **2T**; **(B) 2T** type I dimer; **(C) 2T** type II dimer

By identifying larger oligomeric (heptamer and octamer) species on the surface (**Figure 2.11E**), the TB model was validated. The TB energy band model for an infinitely long **2T-sp** chain (**Figure 2.11B**) reveals emergent metallic behavior resulting from the linear array of zero-modes, thus quenching magnetic order. This behavior is termed diamagnetism (**Section 1.3.2**). A type I **2T** dimer has its HOMO and LUMO at energies corresponding to the bottom edge and top edge of the infinitely long chain, respectively. As a **2T-sp** chain gets longer, its MOs are predicted to lie in evenly spaced intervals within that energy range until at infinite length, the states become continuous, hence metallicity. The TB prediction of the MOs of the heptamer and octamer lie along the metallic band of the infinite chain, as predicted (**Figure 2.11C**). Comparing these predicted states with STS of the heptamer and octamer reveal good agreement between experiment and theory (**Figure 2.11D**). The octamer is gapped, while the heptamer shows a zero-mode. Furthermore, the density of states of each species increases at energies father from zero, with step-increases in d*I*/d*V* corresponding to each MO predicted by the TB model. Mapping the structures using d*I*/d*V* signals at the bottom (–100 mV) and top (100 mV) edges of the metallic band reveal the antibonding- and bonding-like states, respectively (**Figure 2.11F,H**). Mapping at zero bias voltage reveals the localization of the zero-bias peak on odd members of the odd-membered chain and no density on the even-membered chain (**Figure 2.11G**), in good agreement with TB calculations (**Figure 2.11I**). It should be noted that this behavior is influenced by the underlying gold substrate and that claims about the electronic and magnetic structure of **2T-sp** in the vacuum phase cannot be made. It is instructive to look at superpolyacetylene itself, which demonstrates gapped semiconductor properties in solution and solid states, as well as on an insulator surface, but metallic properties when adsorbed on a metallic surface.^{166}

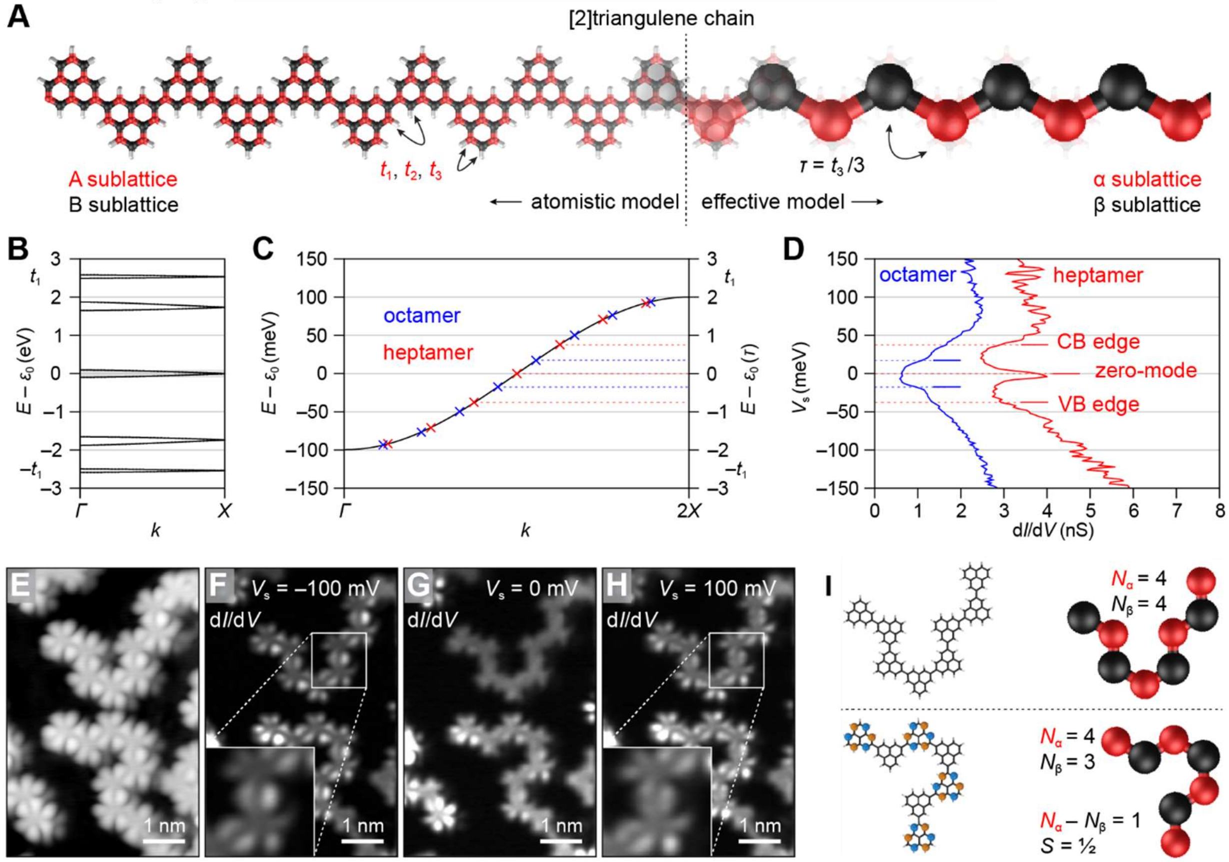

Figure 2.11 Analysis of **2T** oligomers: **(A)** superatom analogy depicting the reiteration of the bipartite physics of graphene replicated in the 1-D superstructure; **(B)** TB-calculated band structure of infinitely long **2T-sp**, depicting the emergent metallic band that results from interaction of neighboring zero-modes through a 3NN interaction; **(C)** zoom-in of the emergent metallic band with TB-calculated MO energies for the heptamer and octamer; **(D)** experimental STS of a **2T** heptamer and octamer, demonstrating good alignment with TB-calculated energy levels; **(E)** STM topographic image of the heptamer and octamer species on the Au(111) surface; (**F–H**) dI/dV maps of the heptamer and octamer chains at bias voltages corresponding to the bonding (–100 mV), gapped (octamer) or nonbonding (heptamer) (0 mV), and antibonding (100 mV) energy levels; **(I)** TB simulations and supermolecule cartoons of the zero energy gapped (octamer) or nonbonding (heptamer) states

Having observed unexpected diamagnetic behavior that violated topological frustration to quench magnetic behavior and form a metallic band between 3rd-nearest-neighbors in bimolecular bonds with δ-symmetry, we went on to study **2T-sp** with biphenyl linkages (**2T-sp-BP**). The biphenyl-linked superpolyacetylene was synthesized from the 2,5-bis(4-iodophenyl)phenalenone (**BP-2-1**) (**Scheme 2.6**). First, Ullman-like cross-coupling on the surface yielded **poly-BP-2-1**, which was then reduced *in situ* using cracked hydrogen on the metallic surface to reduce the phenalenone to the corresponding **2T**. We did not determine whether the corresponding phenalene is an intermediate in the reaction pathway with spontaneous hydrogen atom extrusion or whether the radical species is generated directly through a phenalenol or some otherintermediate.

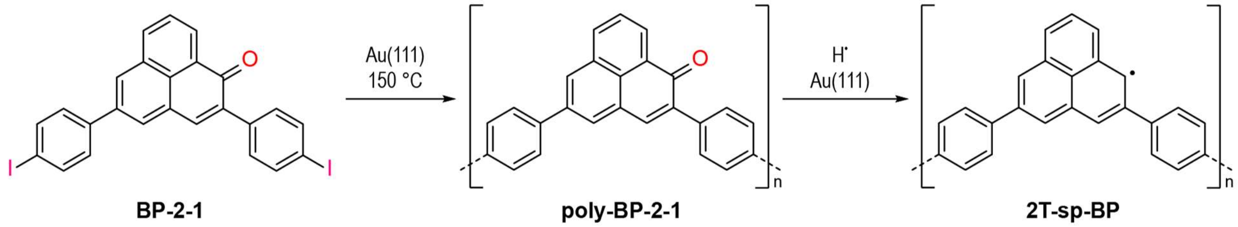

Scheme 2.6 On-surface growth of **2T-sp-BP** from monomer precursor 2,5-bis(4-iodophenyl) phenalenone (**BP-2-1**)

As-deposited monomers self-assembled into pinwheel-like structures on the surface due to halogen-halogen interactions between iodide functionalities. At low coverage, individual pinwheels were observed (**Figure 2.12A**), while at higher coverage, the monomer self-assembled into linear arrays of the pinwheel motif (**Figure 2.12B**). Annealing to 150 °C led to Ullman-like cross-coupling on the surface. The extent of cross-coupling, yielding short oligomers, likely due either to insufficient monomer coverage, low monomer mobility, or the presence of excess hydrogen resulting from troubleshooting the hydrogen cracking apparatus. Oligomers were subsequently reduced *in situ* using the hydrogen cracker and imaged by STM topography at low, non-zero tip bias (**Figure 2.12C**). A zoom-in of this image is provided (**Figure 2.12D**), as well as a zoom-in of a scan that was performed at a tip bias of 0 V, which reveals the lobed structure of the zero-modes of the individual **2T** units. Unlike in **2T-sp**, there does not appear to be hybridization between neighboring zero-modes. Furthermore, it is apparent that not all **2T** units were reduced and activated by the on-surface reduction technique.

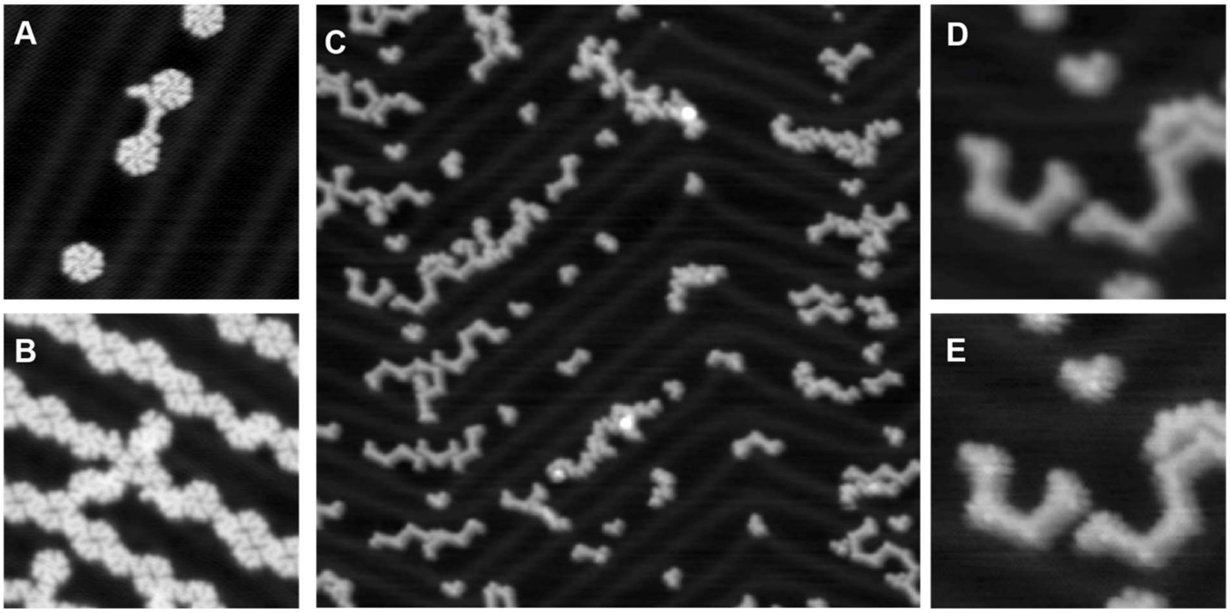

Figure 2.12 STM topographic images of monomer **BP-2-1** and oligomers **2T-sp-BP**: **(A)** low-coverage monomer self-assembly; **(B)** high-coverage monomer self-assembly; **(C)** large-area scan at low, non-zero STM tip bias of **2T-sp-BP** oligomers after annealing to 150 °C; **(D)** zoom-in of oligomers scanned at low, non-zero STM tip bias; **(E)** zoom-in of oligomers scanned at 0 V STM tip bias, revealing lobed structure of **2T** zero-modes

Measuring STS of the **2T-sp-BP** oligomers revealed that inactivated segments showed no unique features distinct from the gold background state (**Figure 2.13B**, red) and that activated units showed Kondo resonances (**Figure 2.13B**, green), consistent with the presence of a magnetic impurity on the metal substrate. A tetramer made up of three active **2T** units and one inactive phenalenone unit was characterized (**Figure 2.13A**). Despite the fact that the left two units of the tetramer are spin-activated compounds, they both display Kondo resonance. This indicates a total lack of magnetic exchange, or at least that the spin interactions with the substrate are stronger than any potential exchanges between neighboring **2T** units. This demonstrated that **2T-sp-BP** is paramagnetic on the gold surface. When monomer synthesis was first begun, we anticipated magnetic order from this structure, but after more recent developments in the literature on **3T** systems, paramagnetism became our preferred hypothesis for this system.[72] This hypothesis was supported in these experiments.

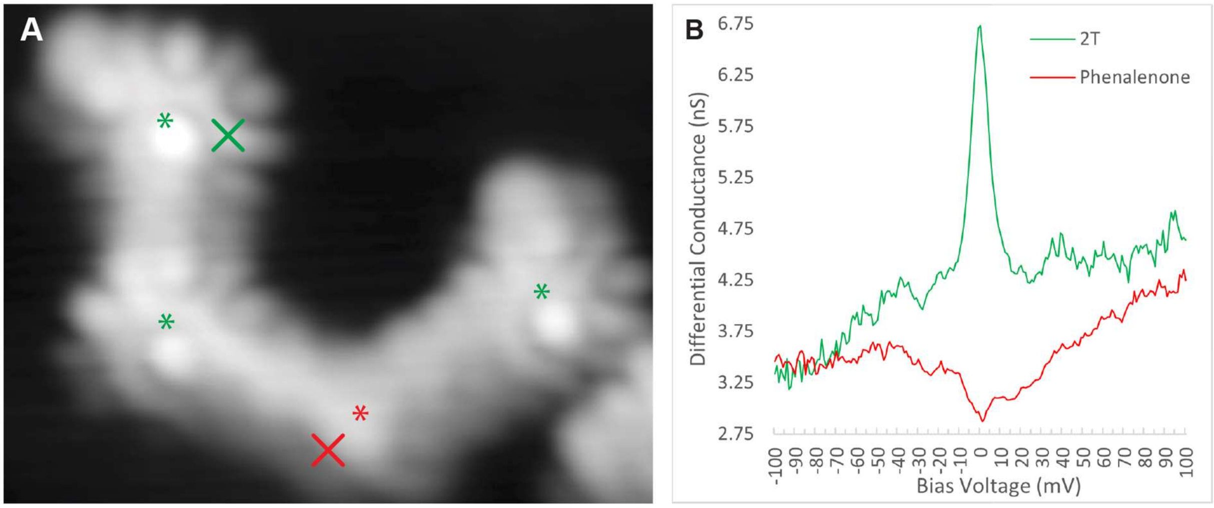

Figure 2.13 **(A)** Tetramer species of **2T-sp-BP** with asterisks indicating activated **2T** (green) and inactivated phenalenone (red) units; **(B)** STS point spectra over the activated **2T** (green) and in inactivated phenalenone (red) units, corresponding to the X marks in panel (A)

2.5 Conclusion and Outlook

Further experiments are anticipated, as two more monomers have been successfully synthesized: 2,5-bis(dibromomethyl)phenalenone (**CC-2-1**) and 5,8-diisopropylphenalenone (**Ph-2-1**). As of writing, these molecules are awaiting study by an STM operator. A single attempt of the reduction reaction to yield 2,5,8-tribromophenalene (**2-2**) was attempted, but the target product could not be isolated due possibly to any of: impure starting material, insufficiently air-free conditions, or the need for more careful purification conditions of the product. Besides these, the groundwork has been laid for a host of other **2T-sp**s and -**sg**s. We hope that other researchers will take up these projects to illuminate the nature of these fascinating all-carbon spin superstructures.

To summarize, a concise synthesis of **2T** precursor phenalenone with di- or tribromination on the apical carbons was completed. This provides the groundwork to generate a modular range of all-carbon superpolyacetylene and supergraphene structures based on the spin doublet

[2]triangulene. Two such superpolyacetylenes were synthesized at the vacuum-gold interface. One directly bonded system was synthesized that demonstrated 3rd-nearest neighbor bonding interactions between molecular orbitals of π-symmetry, leading to δ-bonding and -antibonding interactions—an impressive display of electronic frustration that still eludes the goal of carbon magnetism in this system. The 1-dimensional system with biphenyl linkers between **2T** units displayed paramagnetism due to insufficient magnetic exchange interaction strength between neighboring radicals, at least as long as the structure resides on the metallic substrate. Characterizing these structures on insulator substrates would provide valuable insight as well.

The projects described herein and future inquiries in this realm will provide fascinating insight on the nature of carbon magnetism, a phenomenon that has been largely unattainable using traditional wet chemistry. The implementation of scanning probe techniques has launched the field of carbon magnetism into a new era, providing a means to generating otherwise supremely unstable materials as well as a powerful characterization method to probe their material properties. Spin polarized STM, electron spin resonance, and *in situ* magnetic fields can provide further understanding of these materials, though it was not conducted in this work. Generating an understanding of magnetic carbon materials will make possible the rational design of 2-dimensional materials for use in advanced spintronic logic architectures.

3 Triangulene, *S* = 1 supergraphenes

3.1 Abstract

Triangulene, dubbed "Clar's hydrocarbon" is the namesake of the [*n*]triangulenes and the second homologue in the family, systematically referred to now as [3]triangulene (**3T**). Erich Clar was fascinated with **3T**'s frustrated nature but was unable to isolate or detect the species. In 2001, kinetically stabilized, tri-*tert*-butyl-substituted **3T** was synthesized and studied in a frozen matrix. Aside from this, there has been little inquiry into **3T** and its derivatives until very recently. Its longer and more reactive edges make it a more challenging subject of study than **2T**. In 2017, researchers at IBM Zurich synthesized dihydrotriangulene, deposited it on a copper surface, and used a scanning probe tip to abstract hydrogen atoms to generate **3T** for imaging and electronic characterization. This represented the first ever isolation and characterization of an unsubstituted member of the [*n*]triangulene family. In the same vein as described in **Chapter 2**, we targeted 2-D networks and 1-D chains of **3T**. Although dihydrotriangulene is air sensitive, more so than phenalene, utilizing the toolbox of on-surface synthesis permits a facile synthesis. A surface-assisted cyclodehydrogenation with pendant methyl group permits formation of **3T** from a 9-(*m*-xyl-2-yl)anthracene. Substitution of the anthracene at the 3- and 6-positions yields a monomer that will polymerize on the surface before cyclodehydrogenation into the target polymer. Unfortunately, we discovered while attempting growths of the target monomer that another research group in our field had completed synthesis and begun characterization of the structure. Therefore, the project was abandoned, as well as growths of the 2-dimensional trihalogenated analogue targeted for achieving the 2-dimensional network. Although the 2-dimensional network has mysteriously not yet been published, despite being a logical follow-up to the 1-dimensional chain.

3.2 [3]triangulene

Characterizing unsubstituted triangulene at the vacuum-solid interface was a great realization in the field of physical organic chemistry—a long sought prize.[68] The chemistry of triangulene, dihydrotriangulene, and related compounds is not as well understood as that of phenalenes, phenalenones, and phenalenyls, due to its higher reactivity and spatially extended reactive edges. However, the traditional synthetic toolkit is not needed, as current techniques in on-surface synthesis (OSS) make the triangulene scaffold more easily achievable by making use of a methyl-aryl ring-closing cyclodehydrogenation (**Figure 3.1**). Rather than work with air-sensitive substituted dihydrotriangulenes, the 9-xyl-2-ylanthracene base structure provides a much simpler handhold into a range of substituted **3T** precursors.

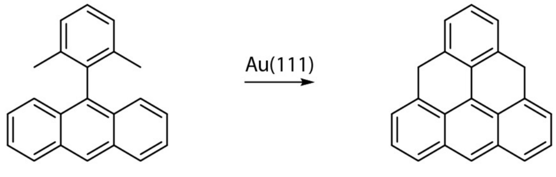

Figure 3.1 Methyl-aryl ring-closing cyclodehydrogenation reaction from xylyl-anthracene to dihydrotriangulene

The properties of **3T** are highly analogous to those of **2T**. **3T** is an open-shell, high-spin nanographene with two degenerate states at zero energy. Its properties can be well understood by Hückel molecular orbital theory, density functional theory, and its properties have been supported by ESR measurements and more recently, by direct STM characterization on a metallic substrate. Its spin density is localized to edge carbons, with no density on apical or interior carbons. The only difference between **3T** and **2T**, besides their size, is the multiplicity of their spin state, with 3T being a spin triplet diradical. By taking the same approach as with the **2T** project described above, **3T** monomers with apical bromide substitution was planned to generate precursors to 1-dimensional chains and 2-dimensional networks of **3T** superstructures via a modular synthesis that could likewise generate superstructures with a variety of linking moieties between spin centers. Once again, 1-dimensional chains were targeted first, due to the more facile nature of the synthesis of monomer precursors and to validate the linear growth before attempting a 2-dimensional growth, which are already significantly more challenging to optimize towards a pristine structure.

Physically speaking, a linear chain of spin triplets is classified as a Haldane chain, as opposed to the spin-½ , which are termed Heisenberg chains. Generating chains of the high-spin, $S = 1$ nanographene 3T presents a desirable target for the understanding of carbon spin dynamics and the realization of an all-carbon Haldane chain. The case for describing poly-[3]triangulene (**poly-3T**) as a superpolyacetylene is less precise than the case for **poly-2T** due to the biradical, triplet nature of the monomer unit; the superatom analogy no longer applies. While working towards these structures, it became apparent that we were not alone, as the synthesis and characterization of dimers of **3T** was published. In this case, we were unfortunately not speedy enough and another research group published a study of **poly-3T** before we could get data on the system. Work on this whole class of projects was subsequently dropped and therefore their discussion here will be kept brief.

3.3 Monomer design and synthesis

Poly-([3]triangulene-2,6-diyl) (**poly-3T**) and **3T** surface covalent organic framework (**3T-sCOF**) were targeted via a dibromo-xylyl anthracene (**3-1**) and dibromo-(bromo-xylyl)anthracene (**3-2**) (**Figure 3.2**). These monomer designs evade the air-sensitive structural components present in the precursors used to achieve unsubstituted [3]triangulene[68] and poly-[2]triangulene (**Chapter 2.3**). The symmetry permitted by the repeat unit allows this design to take advantage of the methyl-closure OSS technique. Monomers **3-1** and **3-2** can be synthesized via a common intermediate, 3,6-dibromo-9-anthrone (**3-6**) and can be further functionalized with isopropyl and 4-iodophenyl substituents, as described in **section 2.3**. Alkynyl-linked structures generated by targeting dibromomethylated precursors may be possible, but the methyl groups of the xylyl components may inhibit solution synthesis of the desired monomer(s) or OSS of the target structure, possibly leading to highly defective structures. The phenyl-linked structure is also attainable via the Kumada coupling to cross-couple on isopropyl groups, as was used to generate the 6-isopropyl-2-naphthol used in the **2T** analogue.

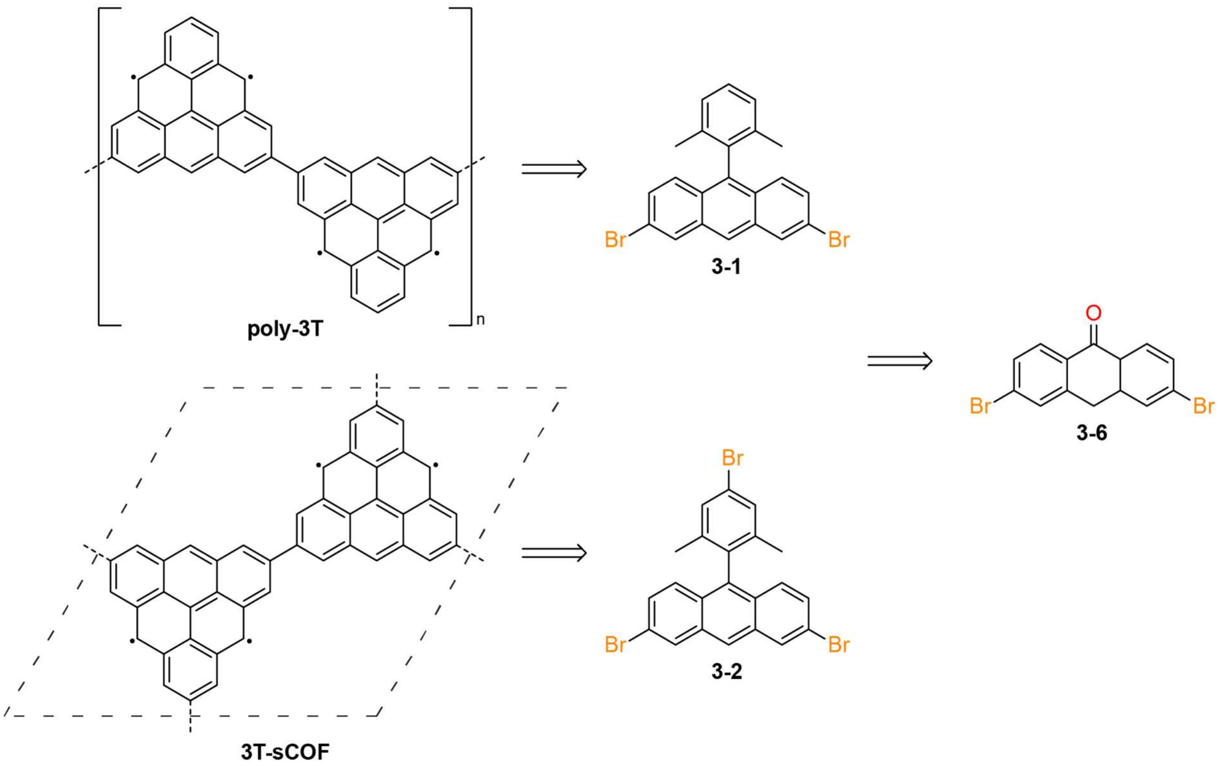

Figure 3.2 Retrosynthesis of **poly-3T** and **3T**-surface COF from brominated xylyl anthracenes

Synthesis of precursor **3-6** was achieved via a route that makes use of two regioselective reactions to achieve bromination in the desired position relative to the anthrone oxygen (**Scheme 3.1**). First, anthrone was doubly nitrated using fuming nitric acid in acetic acid solvent with concomitant oxidation to anthraquinone, which, after recrystallization from acetic acid/nitrobenzene, yielded 2,7-dinitroanthraquinone (**3-3**). Reduction by sodium sulfide under basic conditions yielded 2,7-diaminoanthraquinone (**3-4**). Double Sandmeyer reaction using *tert*-butylnitrite and copper (II) bromide yielded 2,7-dibromoanthraquinone (**3-5**) in good yield, before regioselective reduction of the 9-position of anthraquinone yielded the key intermediate3,6-dibromo-9-anthrone (**3-6**).

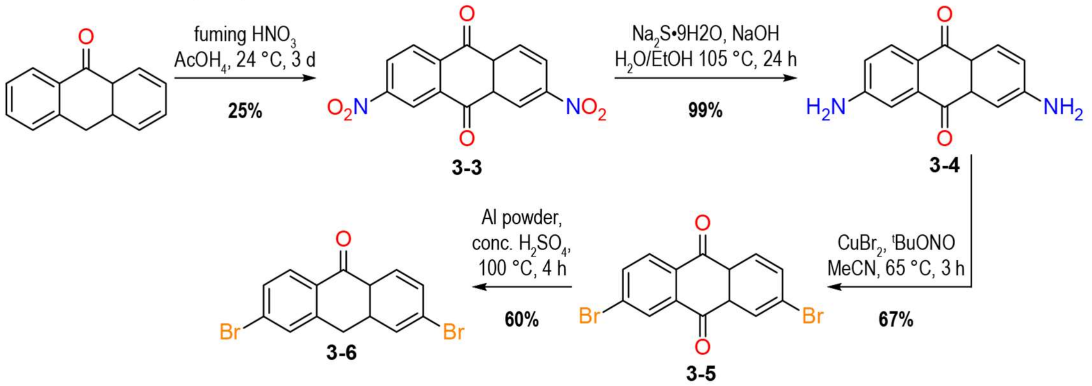

Scheme 3.1 Synthetic route to key intermediate 3,6-dibromo-9-anthrone (**3-6**)

To achieve precursor monomers for poly-[3]triangulene, lithiation of 2-bromo-xylene and quenching with anthrone **3-6** yielded the desired target 3,6-dibromo-9-(*m*-xyl-2-yl)anthracene (**3-1**). The yield of **3-1** was low due to its mild air sensitivity. Repeating the reaction, work-up, and purification with this in mind could lead to improved yields. To generate tribrominated monomer **3-2**, first 4-bromo-2-iodo-*m*-xylene (**3-8**) was synthesized in one step from the corresponding bromoaniline according to a literature-reported Sandmeyer reaction.[211] Selective lithiation at the iodine position was attempted using the same conditions as in the synthesis of **3-1**. Under these conditions, however, it appears that there is sufficient thermal energy for the lithiate species to undergo a further lithium-halogen exchange with itself. The rate of this exchange must be higher than the rate of nucleophilic attack by the nucleophile lithiated at the 2-position (between the methyl groups) because the undesired regioisomer 3,6-dibromo-9-(2-bromo-*m*-xyl-5-yl)anthracene (**3-9**) was generated as the exclusive product, which was confirmed by mass spectrometry and single crystal X-ray diffraction analysis. This reaction was attempted only once before publication of the synthesis and characterization of poly([3]triangulene-2,6-diyl) was published and all related projects in progress in our group were abandoned.

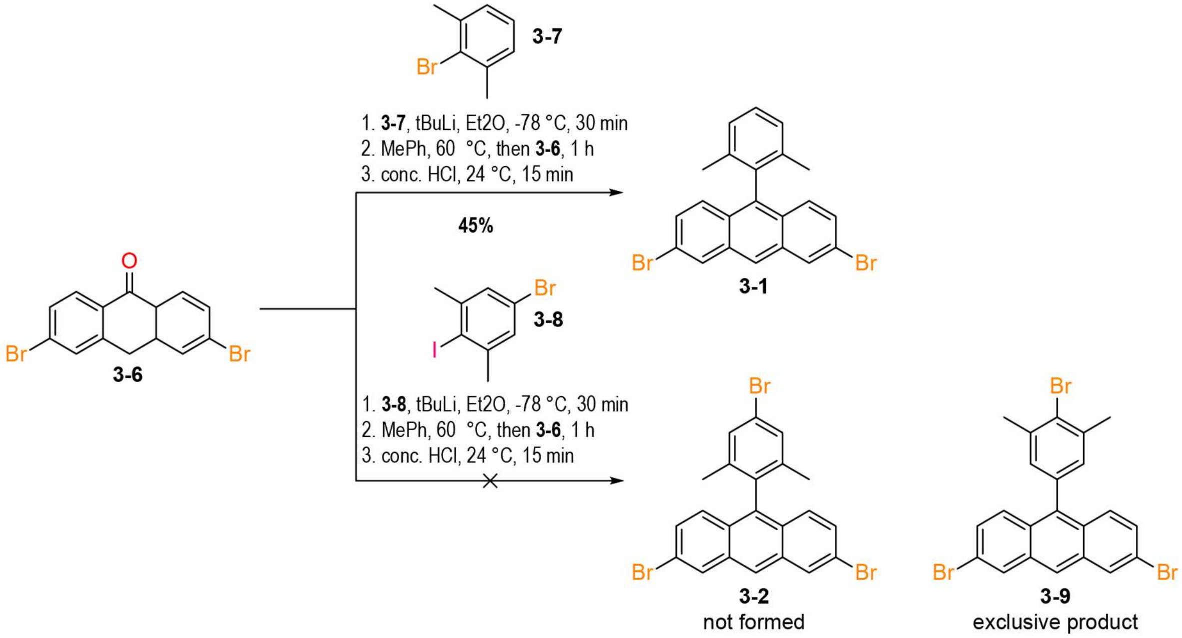

Scheme 3.2 Divergent synthesis from 3,6-dibromo-9-anthrone (**3-6**) to 3,6-dibromo-9-(*m*-xyl-2-yl)anthracene (**3-1**) and 3,6-dibromo-9-(5-bromo-*m*-xyl-2-yl)anthracene (**3-1**)

3.4 Poly-[3]triangulene growth and characterization

Monomer **3-1** was delivered to an STM operator to load into the system for deposition, growth, and characterization. A single growth of the **poly-3T** was attempted, but the topographic maps of the sample did not show the expected product of a chain of triangles. Instead, we observed chains of an oblong species that after some consideration were presumed to be poly-(anthracene-2,7-diyl). Higher resolution STM topographical imaging was not performed on the sample. These results suggested that the annealing temperature was too high, causing cleavage of the somewhat labile phenyl groups, a common and to-be-expected OSS reaction pathway. The monomer was declared to grow poorly, the project deemed a failure, and further optimization was not attempted.

Figure 3.3 STM topographical image of the first and only growth of monomer **3-1**. The identity is presumed to be poly-(anthracene-2,7-diyl), though higher resolution characterization was not performed

Nearly two years later, synthesis and characterization of **poly-3T** was reported in the literature.[50] The reported material was grown from the same monomer, **3-1** via the same route as described here. The authors note that in their experiments, growth of **3-1** was too effective, yielding very long chains. In order to study the size-dependent properties of the material, cogrowths were performed using a singly brominated 3-bromo-9-(*m*-xyl-2-yl)anthracene capping agent at various loading ratios. Spectroscopically, the authors performed thorough characterization of a variety of as-grown structures. Theoretically, they developed a rigorous bilinear-biquadratic (BLBQ) $S = 1$ Hamiltonian model that accurately describes all observations.

The authors discovered a discrepancy between experimental observations in their **poly-3T** sample when they applied the 1-dimensional Heisenberg model using the value of the magnetic exchange coupling (J) determined by their previous study of **3T** dimers (14 meV).[72] This led to their determination of the BLBQ model using J = 18 meV and a weighting factor for the biquadratic portion of $\beta = 0.09$. Using this model, the authors describe a new picture of the $S = 1$ Haldane chain, which demonstrates fractionalization, a long-sought and elusive property of materials in which the material shows transitions with quantum numbers absent from its constituent building block(s). In this picture, each $S = 1$ **3T** unit fractionalizes into two $S = ½$ virtual spins localized on either side of a repeat unit. In a cyclic structure, therefore, these virtual spins pair up into a valence bond solid, and each unit shows a magnetic excitation spectrum that depends only on the size of the macrocycle. For linear chains, however, STS characterization of the repeat units display a unique magnetic excitation spectrum that depends on the position in the chain in addition to the length of the overall chain. In linear chains, there is a length-dependent coupling between terminal $S = ½$ virtual spins corresponding to the singlet-triplet transition that decays with increasing chain length. At length $n \geq 9$, the interactions weaken to such an extent that at the vacuum-gold interface, the Kondo interaction dominates, and a Kondo resonance appears as a spectral feature at the terminal units. The BLBQ model predicts and the authors observed experimentally higher energy transitions associated with spin waves that span the entire material and spin waves that hybridize to the edge states. The authors validate their BLBQ model with extensive characterization of seventeen open-ended chains and eight macrocyclic structures.[50]

In light of this publication, it was decided that all [3]triangulene projects should be halted since our fellow researchers had already carved out this area of study and had a head start on growing and characterizing the materials. This includes: copolymers (e.g. with biphenyl, ethynyl, and phenyl linking units), the 2-dimensional network from target monomer **3-2**, and an anisotropic linear poly-([3]triangulene-2,10-diyl) resulting from a 9-bromo-10-(5-bromo-*m*-xyl-2-yl)anthracene precursor.

3.5 Conclusion and outlook

Surprisingly, there have been no further studies of modular (co)poly-3T materials published in the literature nearly two years later. The original authors mention extension to 2-dimensional networks as a future direction of the project. The monomer **3-2** is surely accessible. It is possible that a tribrominated molecular precursor leads to highly defective growths due to overlapping temperature ranges of on-surface reactions. This was the case for a [4]triangulene sCOF that was initially targeted by a tribrominated monomer, but conversion via aromatic Finkelstein reaction to the corresponding triiodinated molecular precursor allowed growth of reasonably pristine patches.[118] This technique may be necessary for the growth of **3T-sCOF** as well, which material would provide a fascinating ground for the study of quantum spin liquid behaviors.

Copolymers of **3T** would provide a method for validating the BLBQ model further in terms of modulating the β quadratic weighting parameter. The [3]triangulene dimer containing 1,4-phenylene spacer demonstrated a reduced magnetic exchange interaction of 2 meV compared to 14 of the directly bonded dimer. 4,4’’-biphenylene linker would likely lead to lack of magnetic exchange and a paramagnetic material, as was observed for poly([2]triangulene-alt-[1,1’-biphenyl-4,4’’-diyl]) (**Chapter 2.4**). The alkyne-linked structure via a di- or tri-halomethylated monomer precursor may prove inaccessible due to the presence of methyl groups in the base structure of the **3T** precursor molecule. A Kumada coupling to substitute the bromides with isopropyl groups to generate the phenyl-linked structure would be most interesting, as the dimer structure is already known to maintain magnetic exchange, albeit near the limit of detection. We earnestly await future publications resulting from this line of inquiry to further expose the physics of these modular periodic **3T** materials.

4 Regioregular sublattice-imbalanced graphene nanoribbons

4.1 Abstract

Stable (poly)radical molecules have presented an attractive and elusive field of study for synthetic chemists since the beginning of the twentieth century. With progressive study, a growing toolkit for driving a high degree of radical character has grown. Aside from those listed in **Chapter 1.2**, systems using push-pull dynamics, donor-acceptor moieties, donor-acceptor-donor moieties, and other tricks making use of the thermodynamic stabilization made possible by heteroatom functional groups. With this expanding toolbox has come an expanded range of target structures and higher degrees of open-shell radical nature, from radicals to diradicals, to tetra- and hexa-radicals, and the race to the higher degrees continues. As higher degrees of radical nature are achieved, the open-shell structures in question appear more and more as large polyaromatic hydrocarbons (PAHs), making use of the stabilization and radical-driving techniques described in **Chapter 1.2**. Graphene nanoribbons (GNRs) provide an obvious landing-place for the natural limit of such studies. The projects described in this section target GNRs with high degrees of radical character, driven by aromatic stabilization energy, and kinetic protection of unpaired spin density by sterically bulky substituents. Two specific classes of polyradical solution-synthesized graphene nanoribbons were targeted in these projects, regioregular metallic GNR and *m*-indenofluorene-edged GNRs. Solution-synthesis and characterization of these GNRs shifts the toolset from the powerful but restrictive realm of STM to a wider set of methods, such as electron spin resonance (ESR), cyclic voltammetry (CV), UV-Vis spectroscopy, including pump-probe-measurements, and break junction experiments. Tandem STM studies on polymers transferred to the substrate using direct contact methods could permit study of structures that have been otherwise inaccessible due to poor growth or undesired cross-linking.

4.2 Regioregular metallic 9-AGNRs

4.2.1 Introduction

The regioregular metallic 9-armchair graphene nanoribbon (M9-AGNR) targets metallicity. A method for eliciting metallicity from GNRs was developed and published in 2020.[98] Graphene is a zero bandgap semiconductor. Graphene nanoribbons become semiconducting due to quantum confinement in one direction. By evenly spacing additional zero-modes across the ribbon, these zero-modes hybridize into a metallic band.[98,212] This contrasts with the case where zero-modes are unevenly spaced and hybridize into a valence band (VB) and conduction band (CB) according to the Su-Shrieffer-Heeger (SSH) model. These zero-modes can be achieved by sublattice-imbalanced unit cells, in which case topological frustration implies a fully polyradical state. The M9-AGNR targeted herein, however, includes a five-membered ring and sublattice mixing precludes this description. Although sublattice mixing subverts a potentially high-spin periodic material, the aromatic stabilization energy bestowed by the 9-AGNR scaffold is hypothesized to drive the radicals to an open-shell unit cell and facilitate hybridization of zero-modes into a metallic band.

4.2.2 Monomer design and synthesis

The 9-AGNR scaffold was chosen for its ability to stabilize the polyradical structure by the large amount of aromatic stabilization energy. For a tetramer segment of the GNR ribbon, representing two unit cells, the tetraradical structure contains twelve aromatic Clar sextets (**Figure 4.1**, middle). The closed-shell quinoidal structures breaks eight of these sextets in order to form two π-bonds from these four radicals, incurring a significant energetic penalty (**Figure 4.1**, left, right). *Tert*-butyl-xylyl groups provide plural functionality: solubilizing the PAH precursors throughout the synthetic route, solubilizing the final polymer and graphitized structure, and providing kinetic stabilization of radical density by sterically protecting 9-position of the fluorene moiety.

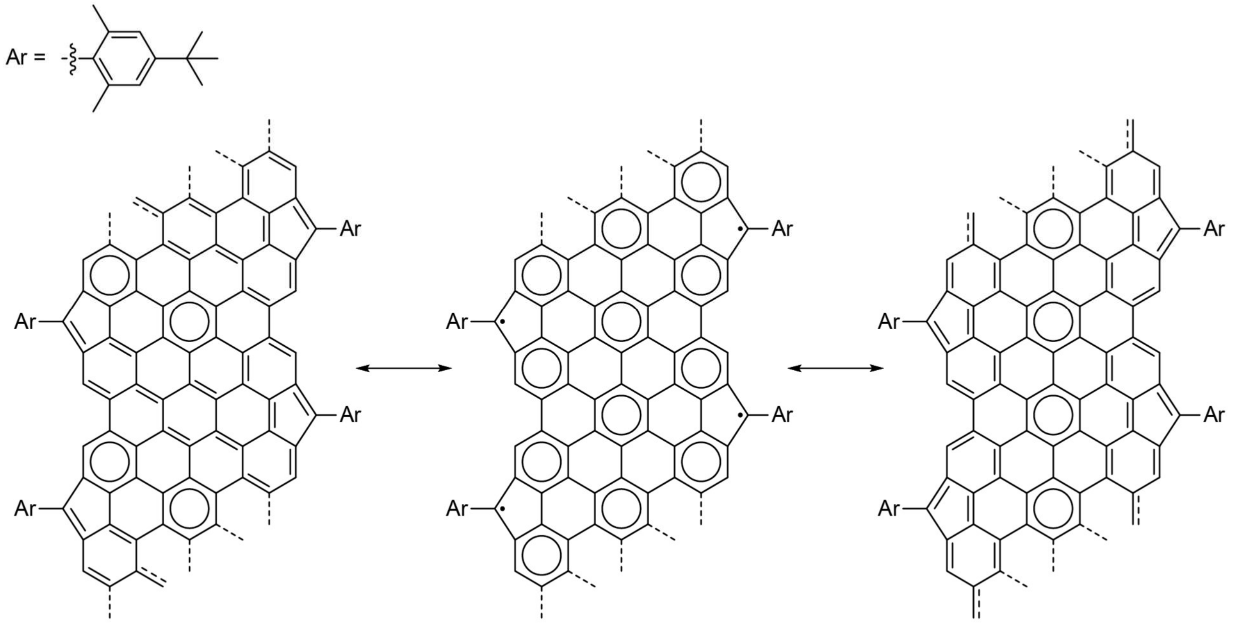

Figure 4.1 Resonance structures of two unit cells of the M9-AGNR, showing highly quinoidal, closed-shell structures (left, right) and highly aromatic tetraradical structure (middle)

The regioregular GNR has been a long-sought material in our group. Its on-surface synthesis was attempted first via a methylated *o*-terphenyl monomer (**MG-g1**) to generate the metallic 9-AGNR described here. Then, a regioregular metallic chevron GNR was targeted by a triphenylene-type monomer with methylated biphenyl moiety (**MG-g2**) and finally by a triphenylene-type monomer with preformed five-membered ring (**MG-g3**). These latter two monomers formed the same cross-linked product on the surface, leading to a porous GNR network with rubicene-type linkages.[213] The former led to highly defective growths and did not generate any regular material.

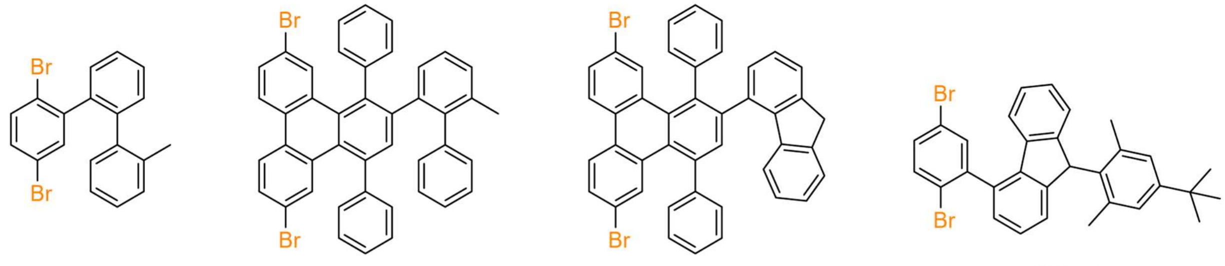

MG-g1 **MG-g2** **MG-g3** MG-g4 **4-1**

Figure 4.2 Previous generations of the M9-AGNR monomer

The fourth generation MG-monomer described herein targets a solution synthesis of the GNR. This permits a different toolset for characterization, such as electron spin resonance (ESR), cyclic voltammetry (CV), UV-Vis spectroscopy, including pump-probe-measurements, and break junction experiments. The material design also lends itself to the possibility of on-surface STM experiments. Dissociation of pendant phenyl groups is a persistent source of defects in bottom-up synthesized GNRs. Methylated phenyl groups are sometimes used for on-surface cyclodehydrogenation with pendant methyl group, leading to cyclodehydrogenation into graphitic structures. The xylyl functionality of the monomer permits solution-phase study of the target GNR but lends as well the possibility of controlled cleavage on the Au (111) surface of the STM substrate. The xylyl group's position on the 9-carbon of fluorene spatially inhibits its methyl groups' ability to fuse with the core GNR structure, promoting cleavage and dissociation. By depositing the pre-formed polymer using matrix-assisted direct contact transfer (MAD transfer) developed in our group, generation of isolated M9-AGNRs was predicted to be possible. The large size of pre-formed polymers inhibits surface diffusion, thus inhibiting the formation of cross-linked networks.

Synthesis of monomer precursor **4-1** began with the generation of two small building blocks. First, 5-*tert*-butyl-*m*-xylene-2-carboxaldehyde (**4-4**) was synthesized by electrophilic aromatic substitution of 5-*t*-butyl-*m*-xylene to generate 2-bromo-4-*t*-butyl-*m*-xylene (**4-3**). Bromide **4-3** was then lithiated using *n*-BuLi and quenched with N,N-dimethylformamide, yielding the aldehyde **4-4**. Both reactions proceeded nearly quantitatively. Separately, 2,2'-dibromobiphenyl (**4-5**) was synthesized from *o*-dibromobenzene using half an equivalent of *n*-BuLi via a benzyne mechanism. Dibromide **4-5** was then singly lithiated using *n*-BuLi, followed by quenching with benzaldehyde **4-4** to generate α-(5-*t*-butyl-*m*-xyl-2-yl)-(2'-bromo-[1,1'-biphenyl])-2-methanol (**4-6**). Alcohol **4-6** was carried forward without purification to a Friedel-Crafts ring closure using boron trifluoride diethyl etherate, yielding 4-bromo-9-(5-*t*-butyl-*m*-xyl-2-yl)fluorene (**4-7**) in 45% yield over two steps. The bromide **4-7** was converted to the boronic ester by palladium-catalyzed Miyaura borylation, yielding 9-(5-*t*-butyl-*m*-xyl-2-yl)fluorene-4-boronic acid pinacol ester (**4-8**) in 65% yield. Selective Suzuki cross-coupling with 1,4-dibromo-2-iodobenzene (**4-9**), which was synthesized in one step from the corresponding dibromoaniline via Sandmeyer reaction, was then performed on boronic ester **4-8**, yielding target product 4-(2,5-dibromophenyl)fluorene (**4-1**) as a colorless viscous oil. Drying fluorene monomer **4-1** under vacuum caused the resin to bubble into a sticky foam. Freezing the resiny foam allowed it to be broken up into a workable, flaky, colorless solid.

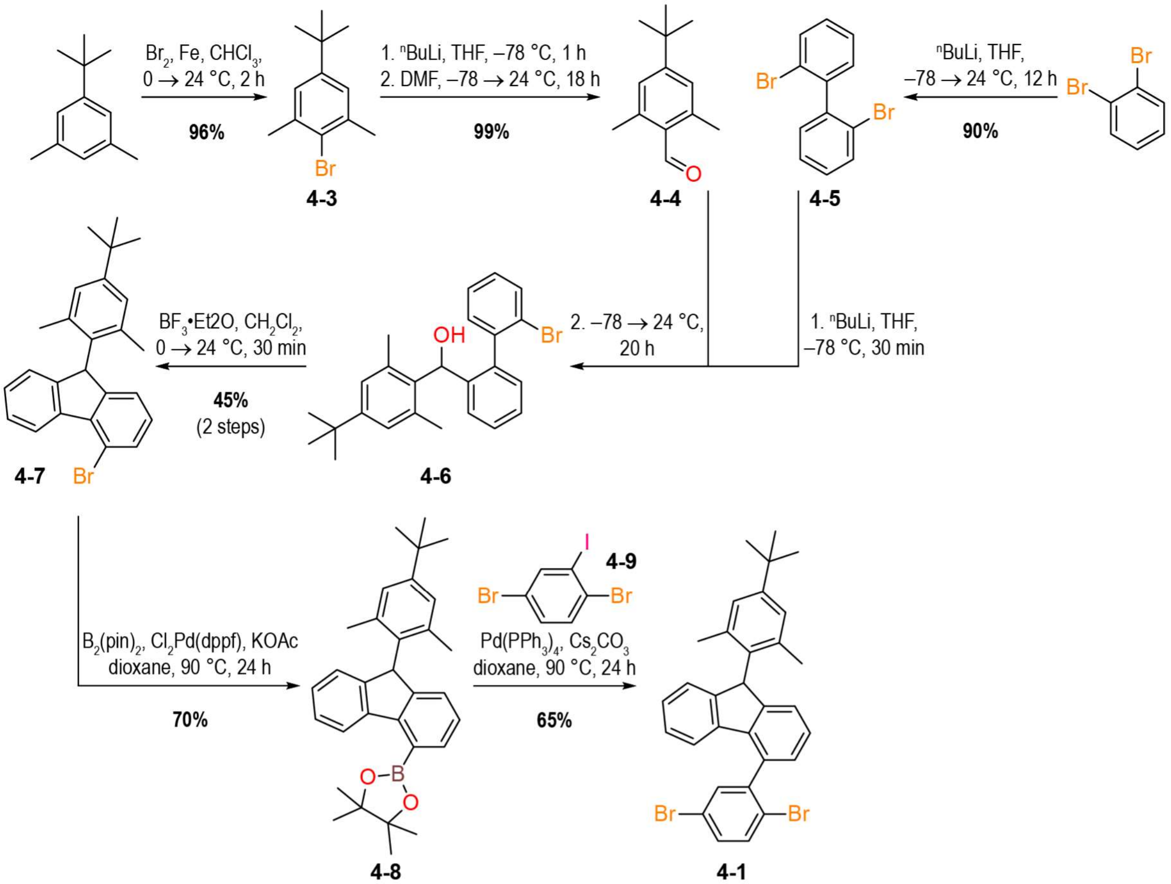

Scheme 4.1 Synthesis of 4-(2,5-dibromophenyl)-9-(5-*t*-butyl-*m*-xyl-2-yl)fluorene, monomer precursor to **M9-AGNR**

With monomer **4-1** in hand, it was thought useful to test the Scholl reaction on the monomer as a model system. Because the five-membered ring of fluorene draws the ring system away from the pendant dibromophenyl group, the Scholl reaction was expected to be challenging due to geometry. The transformation was thought to be attainable, however, due to report on similar systems in the literature.[81] Scholl cyclodehydrogenation indeed failed, however, the geometry could not be pinned as the culprit due to electronic considerations and competing reaction pathways. Under iron trichloride conditions, the fluorene moiety polymerizes at the 2- and 7-positions, yielding an undesired polymeric byproduct (**Figure 4.3**). Triflic acid and 2,3-dichloro-5,6-dicyano-1,4-benzoquinone (DDQ) Scholl conditions also led to undesirable side products, presumably because these conditions abstract a hydrogen atom from fluorene. Performing the reaction with additional equivalents of DDQ and quenching with a silane hydrogen atom donor failed, we predict due to the bulky aryl protecting group on the fluorene and the bulk of the silane hydrogen atom donor inhibiting sufficient proximity for hydrogen atom transfer. Furthermore, density functional theory (DFT) calculations revealed insufficient electron density at the 5-positions of the fluorene moiety or dibromophenyl moiety to promote ring closure, regardless of geometric distance. Finally, a dimer model system was designed and targeted to improve electron density by removing bromide functionality and introducing more sites to initiate graphitization (**Figure 4.3**). This method also failed because borylation of dibromide **4-1** could not be achieved under Miyaura borylation conditions. Organometallic borylation also failed, as expected, due to the presence of the acidic fluorene proton.

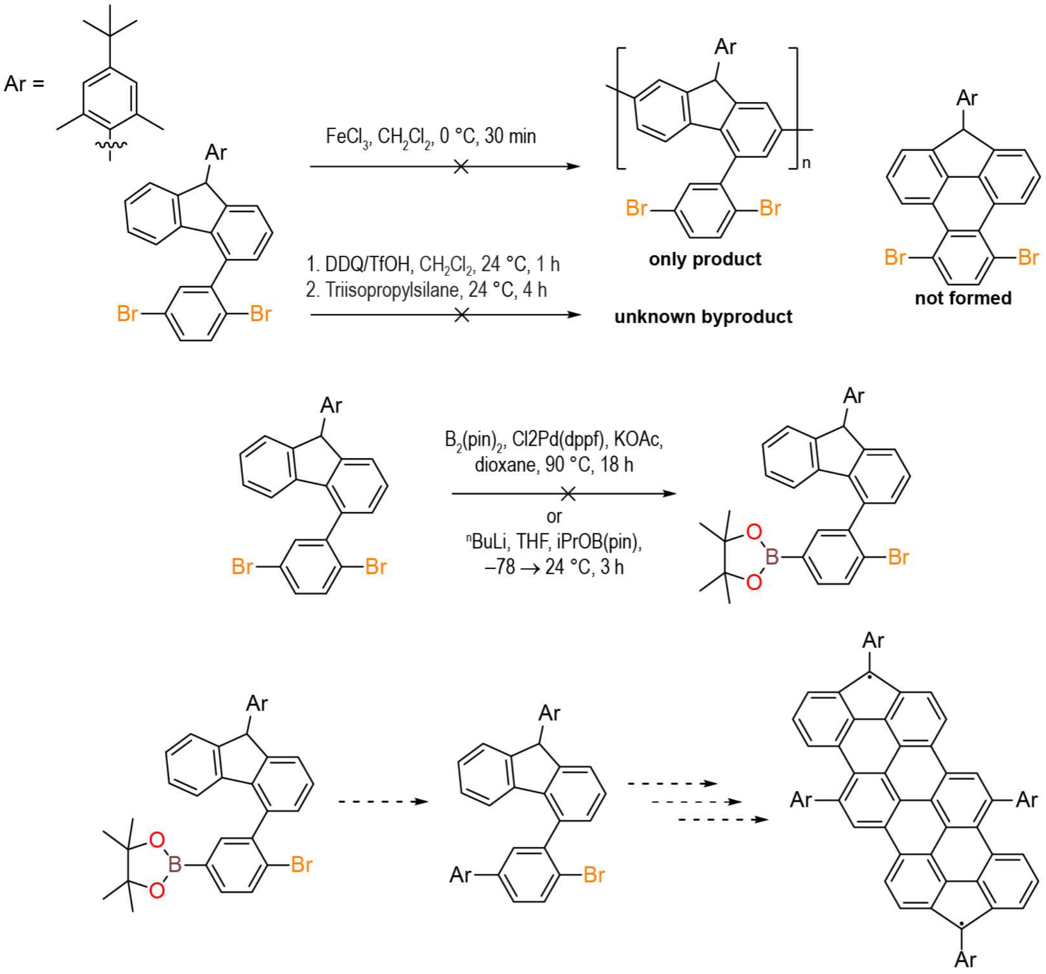

Figure 4.3 Attempts to use monomer precursor **4-1** as model system for experiments

The borylation of monomer **4-1** was initially targeted to promote efficient polymer growth, as a Suzuki polymerization was hypothesized to proceed more effectively than a Yamamoto polymerization, based on group experience. Inability to generate useful model systems for testing the Scholl reaction and failing to produce the singly borylated analogue of **4-1**, however, left Yamamoto as the obvious next choice for proceeding towards the target GNR. Yamamoto polymerization of substituted fluorene, **4-1** (**Scheme 4.2**Scheme 2.1) proceeded with high efficiency, yielding polymers with molecular weights exceeding 100,000 mass units. Length-dependent solubility permitted isolation of two samples: one hexane-soluble sample with lengths up to 25,000 mass units and one chloroform-soluble sample with the larger chains, each sample with moderate polydispersity due to partitioning of the as-synthesized dispersity into two samples. Scholl reaction of the polymers yielded an insoluble plasticky brown substance that was impossible to characterize by any means; Raman spectroscopy gave weak signal, but the pre-polymers were simply too large. The extent of Scholl reaction could not be determined. It is noted, however, that initial iron (III) chloride of the monomer **4-1** as a model system revealed the undesired fluorene polymerization along the 2,7-axis, which should assist graphitization of **poly-4-1**. Cross-linking between fluorenes of different polymer chains, however, cannot be ruled out.

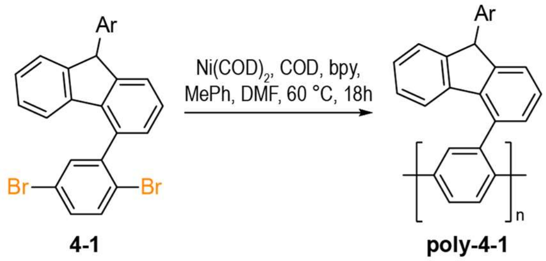

Scheme 4.2 Yamamoto of polymerization of precursor monomer **4-1** to GNR precursor polymer **poly-4-1**

Upon realization that the Yamamoto conditions proceed with high efficiency, the synthetic route towards the dimer model system was reimagined. A Suzuki coupling was attempted between the M9-AGNR monomer **4-1** and the boronic acid pinacol ester of the aryl protecting group. This reaction proceeded in modest yield to generate 4-(2-bromo-5-(5-*tert*-butyl-*m*-xyl-2-yl)phenyl)-9-(5-*tert*-butyl-*m*-xyl-2-yl)fluorene. The two bromide sites of **4-1** are not identical, however cross-coupling appears to have proceeded selectively by NMR. The NMR presents a doubled spectrum with approximately 1:1.5 ratio between the two enantiomers (**4-1** also shows a doubled NMR spectrum due to its enantiomeric nature) We did not determine which bromide was substituted, but the 5-position is less sterically hindered than the 2-position. The Yamamoto dimerization of **4-9** to generate model system **di-4-1** was not completed due to time constraints. This model system would provide useful for determining conditions for the Scholl cyclodehydrogenation, characterizing the graphitic product, and radicalizing the structure to generate the diradicaloid PAH. The tetramer model system may be more valuable in this regard, however, as it represents two unit cells of the target GNR and therefore maybe worth the endeavor of synthesizing.

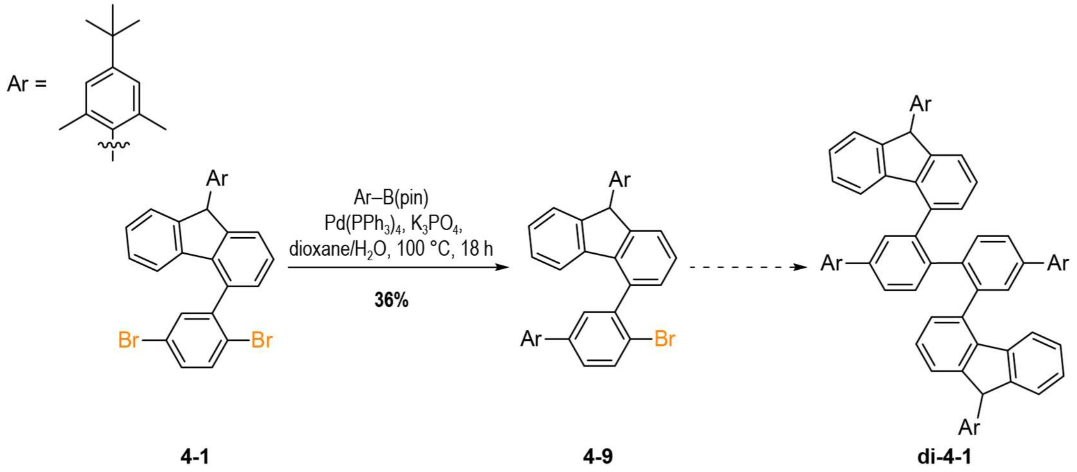

Scheme 4.3 Synthetic route towards dimer model (**di-4-1**) system of the **M9-AGNR**

4.2.3 Material growth and characterization

On-surface studies of the as-formed **poly-4-1** was performed using MAD transfer from a flash-frozen pyrene matrix. Overnight annealing of the deposited sample permitted diffusion of polymer chains. Scanning the sample revealed two types of polymer: type I polymers in which aryl protecting groups appear to remain intact, demonstrated by the zig-zag appearance of the polymer from a large area scan (**Figure 4.4A**) and type II polymers, in which aryl protecting groups appear entirely cleaved (**Figure 4.4B**). These samples were destroyed due to prioritization of other experiments. Further MAD deposition experiments have been completed, but the high variability of this technique means that these pristine structures have not been identified again. Continued depositions and scanning for the target structure are in progress. The evaporation and growth of the monomer precursor **4-1** is also planned.

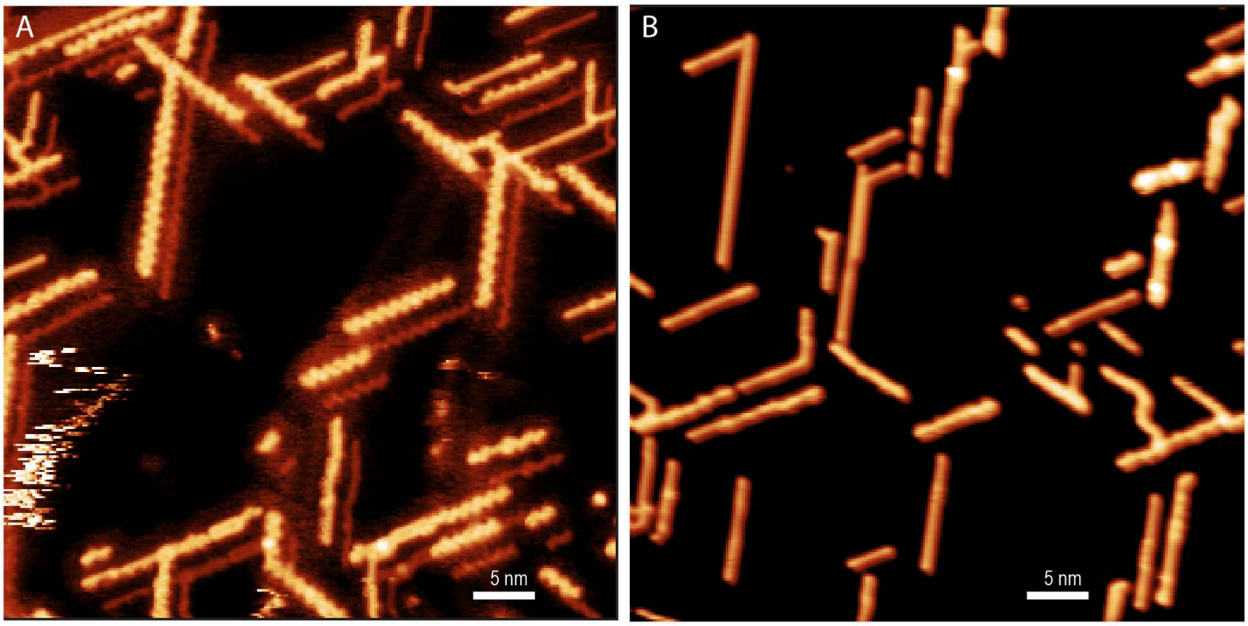

Figure 4.4 STM topographical images of as-deposited M9-AGNR MAD sample. **(A)** Type I: aryl protecting groups appear intact, **(B)** Type II: aryl protecting groups appear to have cleaved entirely on some polymers (top-left), with residual aryl groups remaining on others (bottom-right)

4.2.4 Future directions

Besides, the pending STM analysis of MAD-transferred polymers, the proposed next steps for this project to troubleshoot the solution phase studies are: dimerize precursor **4-9** to generate **di-4-1** and synthesize tetramer **tetra-4-1** (**Scheme 4.4**). The tetramer model system provides a better model system for the full **M9-GNR** because it contains two unit cells of the target GNR instead of just one. This permits validation of the hypothesis that the neighboring fluorene units in the tetramer will promote graphitization via 2,7-polymerization under iron (III) chloride conditions. The graphitized form can also be characterized by Raman spectroscopy, which should give a signal similar to that of the target GNR. Radicalization and ESR spectroscopy should happen next, and it would furthermore be interesting to grow a single crystal of the tetraradicaloid species for XRD analysis.

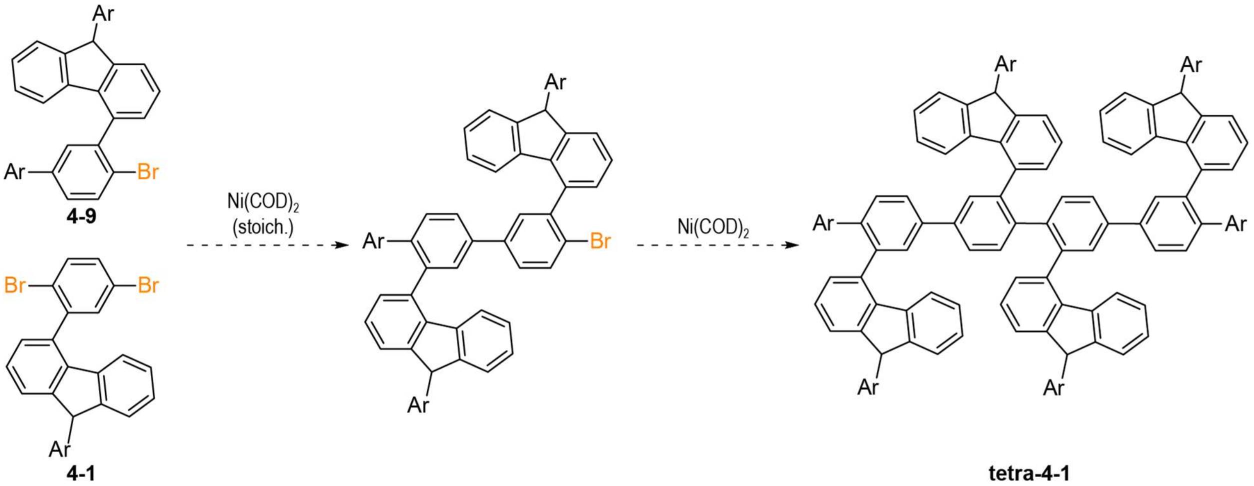

Scheme 4.4 Proposed synthesis to generate tetramer model system **tetra-4-1** from precursors **4-1** and **4-9**

After validating the Scholl, Raman spectroscopy, radicalization, and ESR characterization of **di-4-1** and **tetra-4-1**, the Yamamoto polymerization of **4-1** should be optimized to generate polymers in the range of 5–10 repeat units by running the polymerization with various ratios of capping agent **4-9**. These oligomers should be hexane soluble and can likely be roughly size-separated by column chromatography using a combination of hexanes and diethyl ether or tetrahydrofuran or by preparatory gel-permeation chromatography (GPC). Graphitization, Raman spectroscopy, radicalization, and ESR analysis of these oligomers represent the completion of this project.

Finally, one of the most exciting applications of this scaffold would be to generate GNR heterojunctions. For example, implementing a living polymerization to generate a GNR that is a semiconducting 9-AGNR in the middle with two m9-AGNRs on either end could permit contacting the semiconducting portion in a smaller physical footprint than is possible by depositing gold contacts directly over semiconducting GNRs. The discovery of an easily workable metallic GNR scaffold that is compatible with other GNR geometries is one step towards the ultimate goal of generating molecular integrated circuits.

4.3 *m*-Indenofluorene GNR

4.3.1 Introduction

The second class of polyradical GNRs targeted bear a *m*-indenofluorene moiety integrated periodically in the edge structure of the ribbon. This class is inherently based on a sublattice-mixed moiety and therefore deals with polyradical *character* rather than a polyradical *state*. Indenofluorenes are a highly studied class of polyaromatic hydrocarbons (PAHs). Biradical character is measured as a ratio of the occupancy of the natural orbitals and is termed y_0, which ranges from 0–1, with 0 corresponding to closed-shell and 1 corresponding to a fully diradical state. *M*-indenofluorene is notable for its high y_0 of 0.68. A periodic solution-synthesized and sterically protected/solubilized GNR bearing repeat *m*-indenofluorenes should demonstrate interesting open-shell properties.

4.3.2 Monomer design and synthesis

The 6-zigzag GNR (6-ZGNR) monomer scaffold was chosen due to the ability to incorporate *m*-indenofluorene units and achieve a highly benzenoid structure by deletion of a few carbon atoms per unit cell. One unit cell of the *m*-indenofluorene chevron-type GNR (**miF-chGNR**, **Figure 4.5A**) contains eight Clar sextets in the open-shell tetraradical structure. The closed-shell quinoidal structure breaks six of these sextets to form two π-bonds between these four radicals, incurring a significant energy penalty. One unit cell of the *m*-indenofluorene cove-type GNR (**miF-coGNR**, **Figure 4.5B**) is identical to that of the **miF-chGNR** with the addition of two benzenoid rings that remain untouched in the closed-shell resonance structure. Once again, *tert*-butyl-xylyl groups provide dual functionality that solubilizes the PAH precursors throughout the synthetic route, solubilizes the final polymers and graphitized structures, and provide kinetic stabilization of radical density by sterically protecting the radical-bearing sites of the *m*-indenofluorene five-membered rings.

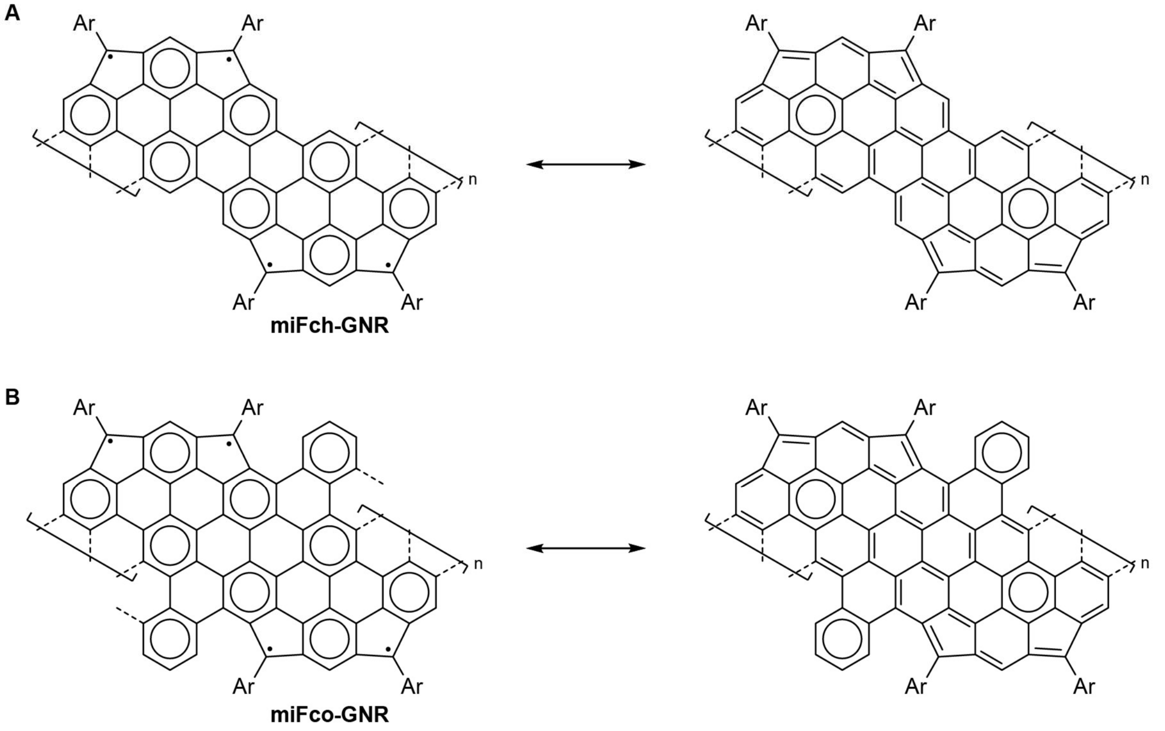

Figure 4.5 Resonance structures of one unit cell of the iF-GNRs, showing highly quinoidal, closed-shell structures (right) and highly aromatic tetraradical structure (left)

The *m*-indenofluorene GNRs were targeted via a "U-shaped" monomer with on-surface cross-coupling handles that point in the transverse direction of ribbon growth. This architecture was used to synthesize 6-ZGNRs using OSS.[92] In this case, however, the dibenzo[a,j]anthracene moiety (**4-0**, **Figure 4.6**) was substituted with a *m*-indenofluorene moiety (**4-3a,b**, **Figure 4.6**). Aryl protecting groups were incorporated for solubility and spin protection for solution experiments. Once again, it was hypothesized that these groups would cleave, rather than cyclodehydrogenate with neighboring pendant methyl groups on the surface, permitting STM characterization in a tandem study.

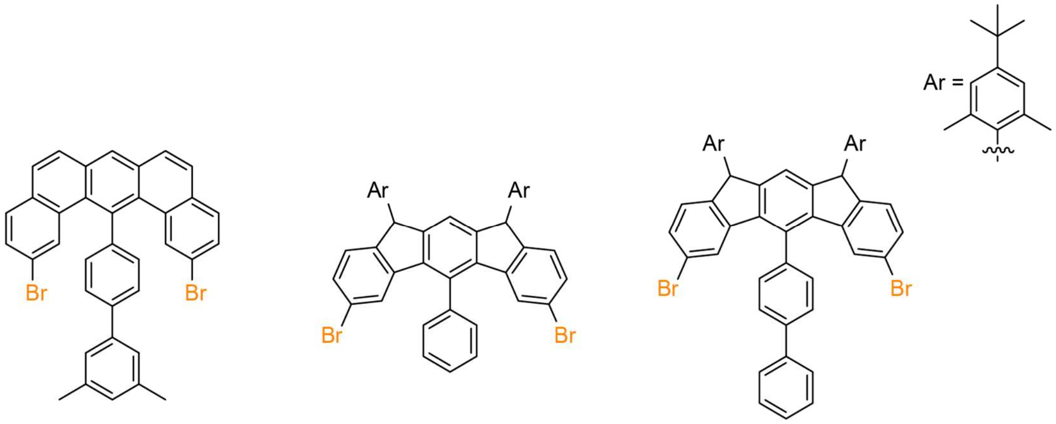

4-0 **4-3a** **4-3b**

Figure 4.6 "U-shaped" monomers used to achieve 6-ZGNRs (**4-0**)[92] and to target iFch-GNR (**4-3a**) and iFco-GNR (**4-3b**)

Synthesis of precursor monomers **4-3a** and **4-3b** were targeted according to a divergent synthesis that was begun by undergraduate assistant, Maggie Khoury. The route begins with synthesis of two small building blocks: 4-methoxy-benzaldehyde-2-boronic acid (**4-12**) and 2,6-dibromo-1,1-biphenyl (**4-13a**) or 2,6-dibromo-1,1:4',1''-terphenyl (**4-13b**) (**Scheme 4.5**). First, 2-bromo-4-methoxy-benzoic acid was reduced by borane to 2-bromo-4-methoxy-benzyl alcohol (**4-10**), which was then oxidized to 2-bromo-4-methoxy-benzaldehyde (**4-11**) using pyridinium chlorochromate (PCC). Borylation of benzaldehyde **4-11** yielded a complex mixture of products that could not be identified (see below for discussion). Biphenyl **4-13a** was synthesized using a one-pot Negishi reaction between 1,3-dibromobenzene and iodobenzene. The corresponding terphenyl, **4-13b**, was not synthesized and has been an elusive compound for our group to isolate. The remainder of the planned route consists of a double Suzuki palladium-catalyzed cross-coupling between building blocks **4-12** and **4-13a**/**b** to generate the substituted triphenylbenzene **4-14a**,**b**. Nucleophilic addition by two equivalents of the lithiate of 2-bromo-5-*t*-butyl-*m*-xylene yielding diol **4-15a**,**b**, followed by Friedel-Crafts cyclization, likely by boron trifluoride diethyl etherate, should give the desired *m*-indenofluorene structure (**4-16a**,**b**). A four-step conversion of the halogen-placeholder methoxy groups yields dibrominated indenofluorene monomers **4-3a**,**b** in a multi-step but reliable series of transformations.

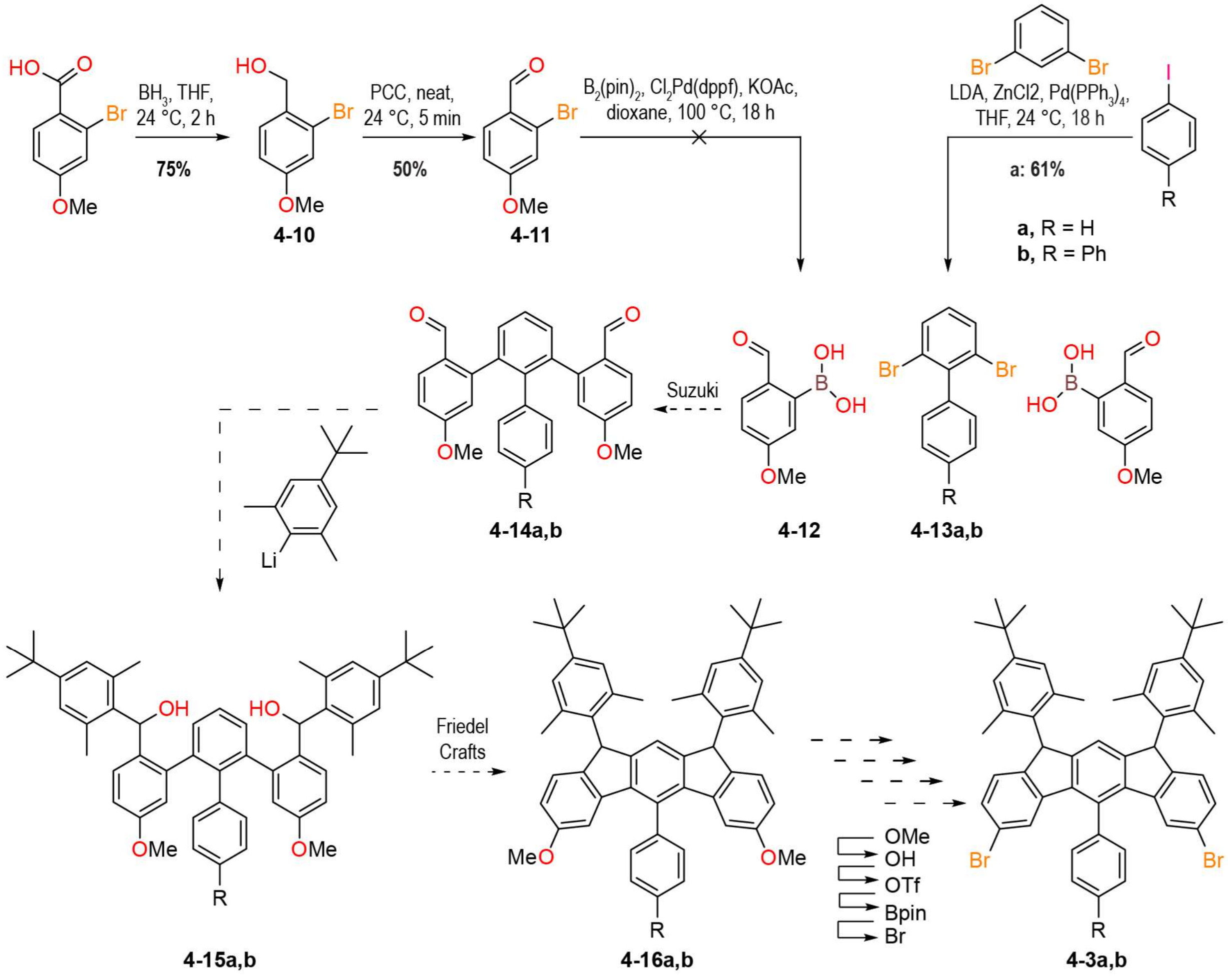

Scheme 4.5 Divergent synthesis towards precursor monomers to **iFch-GNR** and **iFco-GNR**, **4-3a** and **4-3b**

Despite that only a few reactions in **Scheme 4.5** were completed, the compounds generated were already the result of multiple reroutes. Benzaldehyde **4-11** was first targeted by a Vilsmeier-Haack formylation from 3-bromoaniline, which yielded an inseparable mixture of regioisomers. Borylation of benzaldehyde **4-11** using palladium-catalyzed Miyaura borylation conditions failed, possibly due to intramolecular ring formation between the boronate ester and the neighboring aldehyde functionality. Borylation of the preceding benzyl alcohol **4-10** also failed to yield product cleanly, as well as the corresponding *t*-butyl-dimethylsilyl ether-protected benzyl alcohol with two equivalents and one equivalents of *n*-butyllithium, respectively. Due to this trouble, a reroute was planned by reversing the polarity of the Suzuki reaction and the diboronic acid analogue of biphenyl **4-13a** was targeted instead. The diboronic acid could not be isolated before Maggie left the group, however this material has been generated in our group before, so this cross-coupling with bromobenzaldehyde **4-11** towards substituted triphenyl-benzene **4-14a** should be considered by future researchers.

4.3.3 Future directions

In addition to completion of the synthesis, graphitization, radicalization, and characterization, plus on-surface study by MAD transfer, it would be interesting to generate analogous GNRs without the five-membered rings (i.e. chevron and cove-type analogues) in both soluble and surface-ready forms. This would provide a unique one-to-one comparison of the additional properties provided by the indenofluorene moieties and any impact on the energy band structure of the rest of the material, besides the additional bands introduced by the additional lattice sites from the five-membered rings. The 6-ZGNR does not provide this benchmark comparison because of the subtle but impactful deviations in the GNR backbone and the resultant differences in Clar sextet structure.

4.4 Conclusion and outlook

Although no physical characterization results were obtained for the final target materials in these projects, significant progress was made on their syntheses. These materials remain very much viable and an interesting realm of steady left to be explored by other experimentalists. These materials offer valuable insight into metallic, polyradical, sublattice mixed materials to add to the limited body of work already published on the subject. Aside from fundamental interrogations of all-carbon systems, they also provide a platform for novel heterojunctions and hierarchical assembly of molecular circuits.

5 0-D spin systems

5.1 Bi[2]triangulene

5.1.1 Introduction

While surveying the phenalenyl literature, it was observed that despite a variety of studies on bi[2]triangulene,[40,111–113] there has never been a solution synthesis of a kinetically stabilized 2,2’-bi[2]triangulene. This bi[2]triangulene was characterized using STM in the project described in **Chapter 2.4**, but the vacuum-gold interface forces this dimer into a planar configuration. In a solution-phase system, the steric interaction between protons would likely dominate the electronic stabilization provided by π-system overlap found in the planar structure. Electron spin resonance (ESR) and cyclic voltammetry (CV) measurements would provide fascinating insight on this system. UV-Vis spectroscopy alongside computation models could provide evidence for the geometric conformation of the dimer. X-ray diffraction (XRD) of single crystals grown from the diradical would provide certain evidence of the geometric conformation in the solid state, which could feasibly take on a planar geometry due to the possibility for growth of slip-stacked lamellae.

The proposed synthesis was not completed due to prioritization of other projects. The route, however, seems feasible based on literature precedent and related reactions that were completed in pursuit of other projects. If completed, this system would offer valuable insight to the understanding of all-carbon spin systems and the growing body of [*n*]triangulene literature.

5.1.2 Design and synthesis

The synthetic scheme towards 5,8,5’,8’-tetra-*t*-butyl-2,2’-bi[2]triangulene (**5-1**) was conceived of due to the findings that the 2-position of phenalenone is easily and quantitatively brominated and that transition metal-catalyzed cross-coupling at the 2-bromide site takes place efficiently. Therefore, a route was planned by adapting reactions used in **Chapter 2.3** using building blocks with pre-installed kinetically-stabilizing *tert*-butyl groups (**Figure 5.1**). Precedent for the initial building blocks was found in the literature, so some route towards the final target seems achievable.

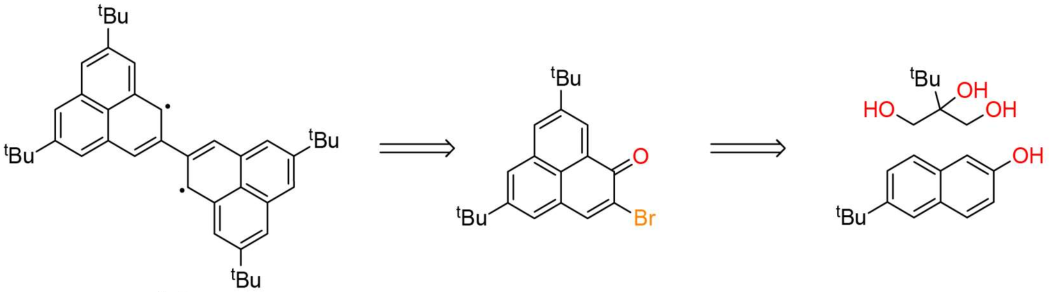

5-1

Figure 5.1 Retrosynthetic analysis of 5,8,5’,8’-tetra-*t*-butyl-2,2’-bi[2]triangulene

The forward synthesis of 2,2’-biphenalenyl was initiated according to the route depicted below (**Scheme 5.1**). First, 2-*t*-butyl-propane-1,2,3-triol (**5-6**) was targeted via a protected dihydroxyacetone. Tris-(hydroxymethyl)aminomethane hydrochloride was condensed with the methyl ketal of acetone, 2,2-dimethoxypropane using an acid catalyst, yielding (5-amino-2,2-dimethyl-1,3-dioxan-5-yl)methanol (**5-3**). Methanol **5-3** was oxidized with sodium periodate, yielding 2,2-dimethyl-1,3-dioxan-5-one (**5-4**) in 39% yield across two steps. The dioxanone **5-4** underwent nucleophilic addition with *tert*-butyl magnesium chloride to generate 5-*t*-butyl-2,2-

dimethyl-dioxan-5-ol (**5-5**), which was then deprotected under acidic conditions to yield the desired propane-triol, **5-6**, in 11% yield over two steps. The poor yield of the target intermediate was expected due to the steric bulk of the Grignard reagent. Separately, 6-*tert*-butyl-2-napthol was targeted by a literature preparation, however only one attempt was made, and the reaction was not performed under sufficiently dry conditions. The rest of the route was not completed due to time constraints but based on other experiments (5,8-diisopropylphenalenone **Ph-2-1**, **Chapter 2.3**), this project seems viable. Addition-elimination bromination of **5-8** to generate 2-bromo-5,8-di-*tert*-butylphenalenone (**5-9**) is expected to proceed efficiently, as it did for the bromination of 5-bromophenalenone. Likewise, was anticipated analogous reduction of phenalenone **5-9** to the corresponding 2-bromo-5,8-di-*tert*-butylphenalene (**5-10**) (mixture of equally useful regioisomers, with **5-10** being the major isomer). The reduction of phenalenone to corresponding phenalene as the penultimate step instead of ultimate poses a challenge in purifying the compound and preparing it for use in the subsequent Yamamoto coupling, but the disproportionation mechanism for the reduction demands this sequence to ensure good yield of 5,5',8,8'-tetra-*t*-butyl-2,2'-biphenalene (**5-11**). Finally, a chloranil oxidation was planned to abstract hydrogen atoms and yield the diradical species for characterization by ESR, crystal growth, and single crystal X-ray diffraction measurements, among other measurement techniques, such as CV and UV-Vis pump-probe spectroscopy.

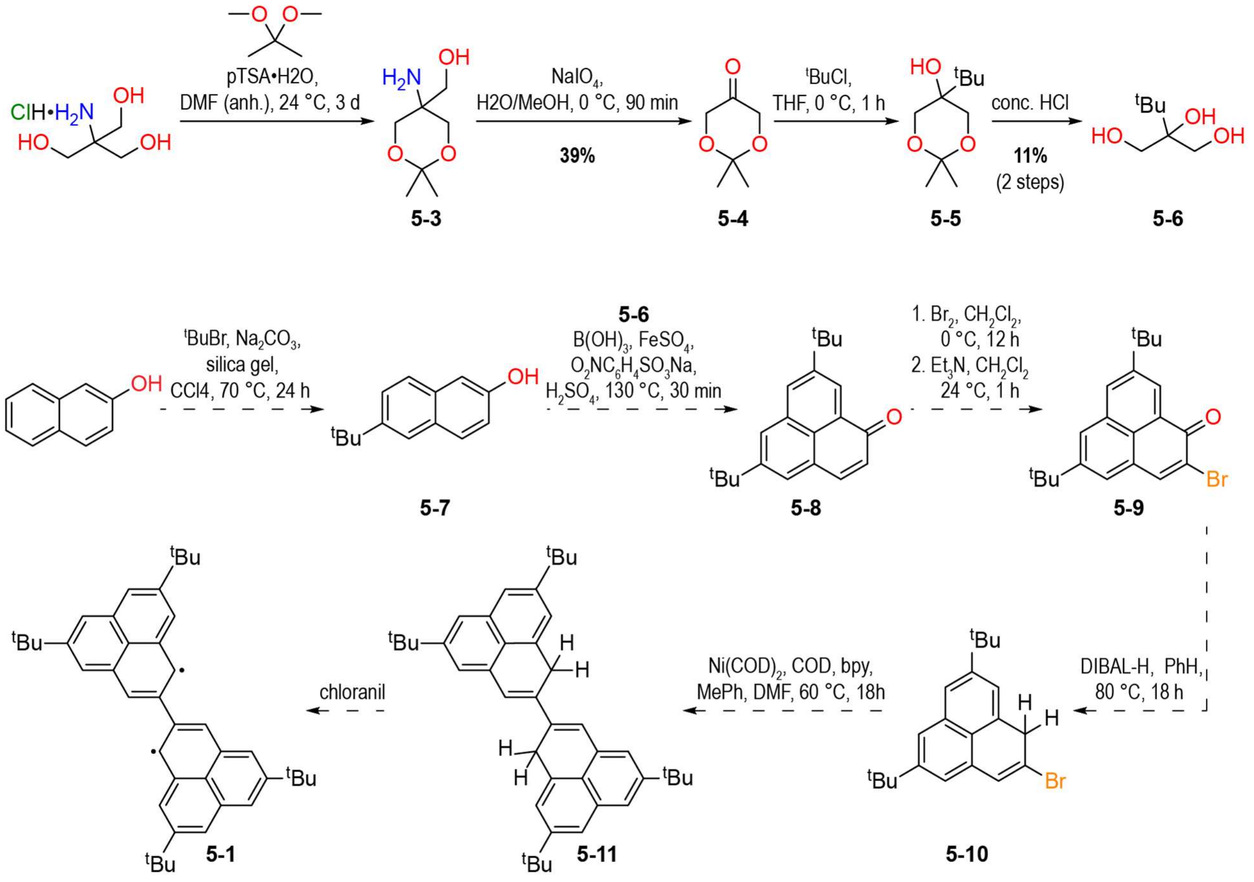

Scheme 5.1 Proposed route towards 5,8,5',8'-tetra-*t*-butyl-2,2'-bi[2]triangulene

5.1.3 Future outlook

Based on other completed projects, the feasibility of this project remains high. Targeting the *tert*-butylated glycerol may proceed more efficiently through 1,3-bis(trimethylsilyloxy)acetone, as was reported for other bulky nucleophiles like isobutane. This project holds the potential for a two-fold contribution: both to the work on biphenalenyls as diradical species, work that has been ongoing since *circa* 2000, as well as to the study of the triangulene class of molecules at the solid-vacuum interface that kicked off in 2019. Uniquely, this work could contribute additional information about biphenalenyl that cannot be determined from on-surface studies, where structures are forced into a flat conformation. An orthogonal conformation that prohibits overlap of neighboring π orbitals is more likely in solution, though as a single crystal, packing forces could hypothetically contribute to a more planarized structure. More broadly, this line of inquiry has direct implications to quantum computing and organic qubits, due to the two-level nature of the correlated diradical system.

5.2 Nitrogen-vacancy center

5.2.1 Introduction

Nitrogen vacancy centers (NV centers) are magnetic defects in diamond that result from the inclusion of a nitrogen atom. The nitrogen atom substitutes a carbon atom, and its lone pair precludes an atom from occupying the neighboring lattice site. This causes dangling bonds from each of the three carbon atoms that neighbor the site of the vacancy. Two of the dangling electrons pair up in a bonding-like interaction, resulting in a doublet ground state. The NV center accepts an electron from the environment, giving it negative charge and a spin triplet ground state with electronic excitations lying in the visible range, hence they are also called color centers.[202] NV centers occur naturally in diamond and are generally rendered my grinding diamond into a fine powder in a top-down method. In this project, we aimed to use our methodology of bottom-up synthesis of unique and structure-dependent carbon nanomaterials to target the smallest functional unit of an NV center. Such a material would be useful for spin-polarized STM experiments and as a sensitizing agent in nuclear magnetic resonance (NMR) experiments, besides interest in its fundamental properties when isolated from the bulk insulator of the diamond structure.

5.2.2 Design and synthesis

The smallest functional unit of an NV center was selected for bottom-up synthesis. The triketone-tertiary amine **5-2** was targeted as a key intermediate with the three ketone groups installed to be used as handles for a Wittig reaction to cap the carbonaceous structure surrounding the NV center. Three ester groups were incorporated into the target structure at the three carbons that each contribute a dangling bond to the NV center electronic structure. Alkaloid **5-2** was not the final target of the synthesis but was hypothesized to be a key intermediate of the project. When the planned synthesis of **5-2** stalled far before reaching the “key intermediate,” the project was abandoned. The work completed thus far is presented for other researchers who want to target this fascinating structure.

Alkaloid **5-2** was targeted by the synthesis depicted (**Scheme 5.2**). First, 1,1,3,3-tetrabromoacetone (**5-12**) was synthesized from acetone via an enol route using hydrobromic acid and elemental bromine. Tetrabromide **5-12** underwent Diels-Alder cycloaddition with cyclopentadiene in the presence of zinc-copper couple followed by zinc-catalyzed debromination to yield bicyclo[3.2.1]oct-6-en-3-one (**5-13**). The bicycle was found to be highly unstable, rendering challenging its isolation, purification, and subsequent reaction. The material degraded into an uncharacterizable black residue. We hypothesize interaction between the occupied π bonding orbitals of the alkene and the unoccupied π* antibonding orbitals of the ketone functionality, leading to either polymerization or oxidation. Using carefully air-free and dark conditions, bicycle **5-13** was successfully reductively aminated using ammonia in anhydrous ethanol and sodium borohydride to synthesize 3-amino-bicyclo[3.2.1]oct-6-ene (**5-14**). For the purposes of achieving structure **5-2**, the endo isomer of the bicyclic amine was desired. NMR spectroscopy revealed formation of a single endo/exo isomer, and the desired endo isomer was hypothesized to be preferred by sterics. Conversion of the ketone to the amine was poor and the project was abandoned without determining the stereochemistry of the bicyclic primary amine.

The intention for the remainder of the synthetic route was to iterate the reductive amination between the amine **5-14** and the ketone **5-13** to generate first the secondary bis(bicyclic) amine **5-15** and then tertiary tris(bicyclic) amine **5-16**. Ozonolysis of the tertiary amine **5-16** was planned to generate the tris(cyclohexyl-dial) **5-17**, permitting catalyzed esterification to generate tertiary amine **5-18** followed by Dieckmann cyclization to synthesize target key intermediate alkaloid **5-2**.

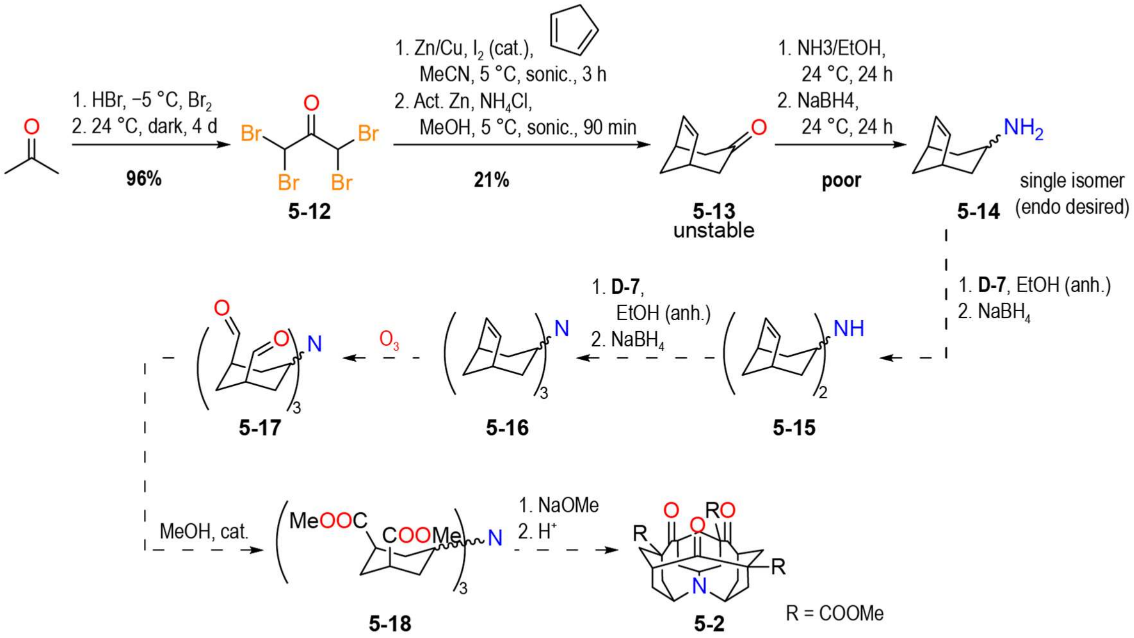

Scheme 5.2 Synthetic route towards key intermediate alkaloid **5-2**, precursor to bottom-up synthesized NV center

5.2.3 Future outlook

Synthesis toward key intermediate **5-2** was challenging from the first step. The idea and work thus far are presented here for any chemist interested in taking on this Herculean task. If successful, ultimately nanoscopic NV centers would be an extremely useful tool in experiments in a wide range of fields for their use as hyperpolarizing agents and potential as magnetic probes.

6 Supplementary information

6.1 Materials and methods

Unless otherwise stated, all manipulations of air and/or moisture sensitive compounds were carried out in oven-dried glassware, under an atmosphere of N_2. All solvents and reagents were purchased from Alfa Aesar, Spectrum Chemicals, Acros Organics, TCI America, and Sigma-Aldrich and were used as received unless otherwise noted. Organic solvents were dried by passing through a column of alumina and were degassed by vigorous bubbling of N_2 through the solvent for 20 min. Flash column chromatography was performed on SiliCycle silica gel (particle size 40–63 µm), unless otherwise noted. Thin layer chromatography was performed using SiliCycle silica gel 60 Å F-254 precoated plates (0.25 mm thick) and visualized by UV absorption. All ^{1}H and ^{13}C NMR spectra were recorded on Bruker AVB-400, AV-600, AV-700, and Neo-500 MHz spectrometers, and are referenced to residual solvent peaks ($CDCl_3$ ^{1}H NMR = 7.26 ppm, ^{13}C NMR = 77.16 ppm; CD_2Cl_2 ^{1}H NMR = 5.32 ppm, ^{13}C NMR = 53.84 ppm). ESI mass spectrometry was performed on a Finnigan LTQFT (Thermo) spectrometer in positive ionization mode. MALDI mass spectrometry was performed on a Voyager-DE PRO (Applied Biosystems Voyager System 6322) in positive mode using a matrix of dithranol. Gel permeation chromatography (GPC) was carried out on a LC/MS Agilent 1260 Infinity set up with a guard and two Agilent Polypore 300 × 7.5 mm columns at 35 °C. All GPC analyses were performed on a 0.2 mg mL^{-1} solution of polymer in $CHCl_3$. An injection volume of 25 µL and a flow rate of 1 mL min^{-1} were used. Calibration was based on narrow polydispersity polystyrene standards ranging from M_w = 100 to 4,068,981 au. Raman spectroscopy was performed on a Horiba Jobin Yvon LabRAM ARAMIS confocal Raman microscope with 532 nm excitation wavelength.

6.2 Chapter 2 supplement

6.2.1 Previously synthesized compounds

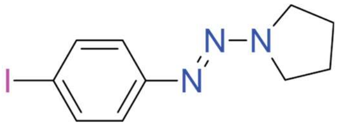

2-6

1-((4-iodophenyl)diazenyl)pyrrolidine (**2-6**),[214] 52% yield. ^{1}H NMR (400 MHz, $CDCl_3$) δ = 7.66–7.55 (m, 2H), 7.19–7.11 (m, 2H), 3.78 (br s, 4H), 2.07–1.97 (m, 4H) ppm.

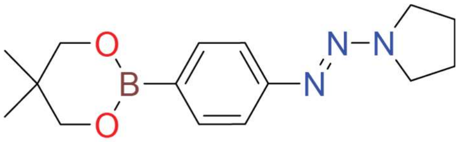

2-7

N-pyrrolidinyl-4-phenyl-azo-boronic acid neopentylglycol ester (**2-7**),[214] 29% yield. ^{1}H NMR (500 MHz, $CDCl_3$) δ = 7.77 (d, J = 8.4 Hz, 2H), 7.42 (d, J = 8.1 Hz, 2H), 3.83 (br s, 4H), 3.76 (s, 4H), 1.02 (s, 6H) ppm.

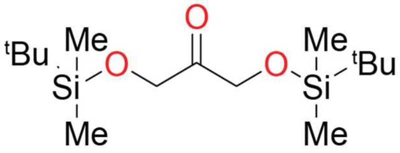

2-10

1,3-bis(tert-butyl-dimethyl-silyloxy)acetone (**2-10**),[215] 92% yield. ^{1}H NMR (700 MHz, $CDCl_3$) δ = 4.41 (s, 4H), 0.92 (s, 18H), 0.09 (s, 12H) ppm.

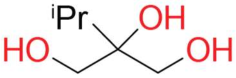

2-11

2-isopropyl-propane-1,2,3-triol (**2-11**) adapted procedure,[215] 24% yield. ^{1}H NMR (700 MHz, DMSO-d6) δ = 4.28 (t, *J* = 5.6 Hz, 2H), 3.68 (s, 1H), 3.37 (dd, *J* = 10.7, 5.2 Hz, 2H), 3.32 (dd, *J* = 10.8, 6.0 Hz, 2H), 1.78 (hept, *J* = 6.9 Hz, 1H), 0.85 (d, *J* = 7.0 Hz, 6H) ppm.

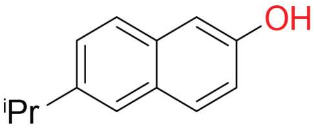

2-12

2-isopropyl-6-naphthol (**2-12**),[216] 78% yield. ^{1}H NMR (400 MHz, $CDCl_3$) δ = 7.74 (d, *J* = 8.8 Hz, 1H), 7.67 (d, *J* = 8.5 Hz, 1H), 7.61 (d, *J* = 1.8 Hz, 1H), 7.39 (dd, *J* = 8.5, 1.8 Hz, 1H), 7.16 (d, *J* = 2.5 Hz, 1H), 7.11 (dd, *J* = 8.8, 2.5 Hz, 1H), 5.04 (s, 1H), 3.08 (hept, *J* = 6.9 Hz, 1H), 1.37 (d, *J* = 6.9 Hz, 6H) ppm.

6.2.2 Synthetic procedures

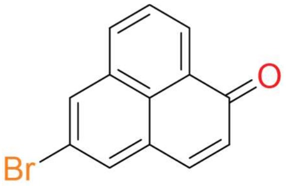

2-3

5-bromophenalenone (**2-3**) A 20 mL microwave tube was charged with a stir bar, glycerol (1.52 g, 16.5 mmol), 6-bromo-2-naphthol (736 mg, 3.3 mmol), boric acid (286 mg, 4.62 mmol), sodium 3-nitrobenzenesulfonate (743 mg, 3.3 mmol), iron sulfate heptahydrate (183 mg, 0.66 mmol), and concentrated sulfuric acid (2.5 mL). The microwave tube was sealed and heated with stirring to 130 °C by microwave irradiation for 30 min. The dark, viscous crude material was diluted with water and neutralized to pH 7 with aqueous potassium hydroxide (20% w/v). The inhomogeneous aqueous mixture was filtered under vacuum overnight. The aqueous filtrate was extracted with Et_2O (2 × 100 mL), and the dark filter cake was Soxhlet extracted with Et_2O (400 mL) for 48 h. The liquid-liquid extract was combined with the golden Soxhlet extract solution and polar impurities were removed by filtration over a short plug of silica gel using Et_2O as eluent. The filtrate was then concentrated on a rotary evaporator. Column chromatography (SiO_2; hexane/chloroform 1:2, 44 °C) yielded 5-bromophenalenone (**2-3**) (351 mg, 1.35 mmol, 41%) as a yellow powder. ^{1}H NMR (500 MHz, $CDCl_3$) δ = 8.60 (dd, *J* = 7.3, 1.2 Hz, 1H), 8.18 (d, *J* = 1.8 Hz, 1H), 8.12 (dd, *J* = 8.2, 1.2 Hz, 1H), 7.83 (d, *J* = 1.8 Hz, 1H), 7.80 (t, *J* = 7.7 Hz, 1H), 7.68 (d, *J* = 9.8 Hz, 1H), 6.75 (d, *J* = 9.8 Hz, 1H) ppm; ^{13}C {^{1}H} NMR (101 MHz, $CDCl_3$) δ = 185.3, 140.6, 134.0, 133.8, 133.4, 133.3, 130.6, 130.5, 129.7, 129.6, 128.3, 126.3, 120.5 ppm; HRMS (EI) *m/z*: $[^{12}C_{13}{}^{1}H_{7}{}^{16}O^{81}Br]^{+}$ calcd. 259.9660, found 259.9654.

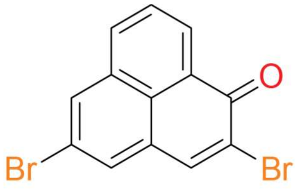

2-4

2,5-dibromophenalenone (**2-4**) A 250 mL round bottom flask was charged with a stir bar, 5-bromophenalenone (**2-3**) (1.21 g, 4.7 mmol), and CH_2Cl_2 (75 mL). The reaction mixture was cooled to 0 °C and bromine (0.97 g, 6.1 mmol) dissolved in CH_2Cl_2 (10 mL) was added over the course of 5 min with stirring. The mixture was stirred overnight, allowing the reaction to warm to 24 °C. Triethylamine (0.85 g, 8.4 mmol) dissolved in CH_2Cl_2 (10 mL) was added over the course of 5 min and the reaction was stirred at 24 °C for 1 h. The reaction mixture was diluted with CH_2Cl_2 (50 mL), quenched with aqueous sodium sulfite (10% w/v), and the organic phase separated. The aqueous phase was extracted with CH_2Cl_2 (50 mL), and the combined organic phases were washed with aqueous sodium sulfite (10% w/v), saturated aqueous sodium bicarbonate, saturated aqueous sodium chloride, dried over magnesium sulfate, and filtered over a short plug of silica gel using CH_2Cl_2 as eluent. The solution was concentrated on a rotary evaporator, yielding 2,5-dibromophenalenone (**2-4**) (1.57 g, 4.6 mmol, quant.) as a yellow powder. ^{1}H NMR (500 MHz, $CDCl_3$) δ = 8.69 (dd, *J* = 7.4, 1.2 Hz, 1H), 8.21 (d, *J* = 1.8 Hz, 1H), 8.14 (dd, *J* = 8.3, 1.3 Hz, 1H), 8.13 (s, 1H), 7.81 (t, *J* = 7.8 Hz, 1H), 7.80 (d, *J* = 1.8 Hz, 1H) ppm; $^{13}C\ \{^{1}H\}$ NMR (126 MHz, $CDCl_3$) δ = 178.4, 141.8, 134.7, 133.7 (2C), 133.3, 132.5, 129.6, 128.7, 128.6, 127.4, 125.4, 120.7 ppm; HRMS (ESI-FTMS) *m/z*: $[^{12}C_{13}{}^{1}H_{6}{}^{16}O^{79}Br^{81}Br]^{+}$ calcd. 337.8765, found 337.8766.

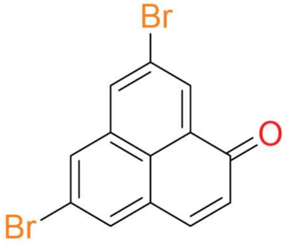

2-4a

5,8-dibromophenalenone (**2-4a**) A 2–5 mL microwave reaction tube was charged with a stir bar, 5-bromophenalenone (**2-3**) (259 mg, 1 mmol), N-bromosuccinimide (169 mg, 0.95 mmol), and sulfuric acid (concentrated, 2.5 mL). The reaction tube was sealed and heated to 105 °C in an oil bath for 18 h. The reaction mixture was then cooled, poured over ice, and extracted with CH_2Cl_2. The combined organic phase was washed with saturated aqueous sodium bicarbonate, dried over magnesium sulfate, and filtered over a plug of silica gel using CH_2Cl_2 as eluent. The solution was concentrated on a rotary evaporator. Column chromatography (SiO_2, dichloromethane/hexanes 11:9) yielded 5,8-dibromophenalenone (**2-4a**) (40 mg, 0.12 mmol, 12%) as a yellow powder. ^{1}H NMR (700 MHz, $CDCl_3$) δ = 8.62 (s, 1H), 8.24 (d, *J* = 2.3 Hz, 1H), 8.08 (d, *J* = 2.1 Hz, 1H), 7.82 (d, *J* = 2.1 Hz, 1H), 7.66 (dd, *J* = 9.8, 1.8 Hz, 1H), 6.72 (dd, *J* = 9.8, 1.8 Hz, 1H) ppm; ^{13}C NMR (151 MHz, $CDCl_3$) δ 184.0, 140.5, 135.3, 134.6, 133.9, 133.2, 132.0, 130.6, 130.1, 129.7, 124.7, 122.7, 121.6 ppm.

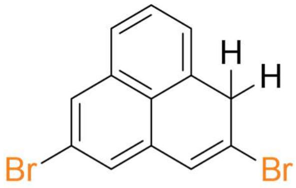

2-1

2,5-Dibromophenalene (**2-1**) A 100 mL oven-dry Schlenk flask was charged under N_2 with a stir bar, 2,5-dibromophenalenone (**2-4**) (1.35 g, 4 mmol), and degassed benzene (anhydrous, 25 mL). DIBAL-H (1 M in heptane, 8 mL, 8 mmol) was added over 30 min by syringe pump with stirring, during which the inhomogeneous yellow suspension became brownish, then a homogeneous reddish, before reaching deep red. A cold finger was affixed to the Schlenk flask, and the reaction mixture heated to 80 °C overnight. After heating for 18 h, the reaction was cooled, the cold finger replaced with a rubber septum and the reaction was quenched by addition via syringe of degassed saturated aqueous ammonium chloride (10 mL), yielding a brown suspension and gelatinous salts. The mixture was diluted with degassed hexane (10 mL) and stirred for 30 min to promote disproportionation of phenalenol into phenalene and phenalenone. The reaction was extracted with degassed hexane 4 × 15 mL by vigorous stirring in the reaction vessel followed by cannulating off the organic layer into a 100 mL Schlenk tube under N_2. The organic phase was washed under N_2 with degassed saturated aqueous ammonium chloride and the organic phase taken up by syringe and then dispensed through syringe filter (PTFE, 0.20 μm) into a separate N_2-purged 100 mL Schlenk tube with stir bar. The solution was concentrated by in-line distillation under nitrogen. Column chromatography (florisil; degassed hexane; nitrogen gas) yielded dibromophenalene (**2-1**) (178 mg, 0.55 mmol, 27%) as a fluffy colorless solid. Due to the disproportionation reaction of phenalenol into phenalene and phenalenone, the theoretical yield of this reaction is half as many moles as phenalenone starting material and furthermore, leads to a mixture of 3 regioisomers in a roughly 10:10:1 ratio. NMR peaks are reported for the 2 dominant regioisomers, hence double the expected protons and carbons. ^{1}H NMR (500 MHz, $CDCl_3$) δ = 7.75 (q, J = 1.5 Hz, 1H), 7.72 (d, J = 1.9 Hz, 1H), 7.52 – 7.49 (m, 1H), 7.47 (dd, J = 8.4, 1.1 Hz, 1H), 7.43 – 7.37 (m, 1H), 7.34 (q, J = 1.9 Hz, 1H), 7.30 (dd, J = 8.4, 7.0 Hz, 1H), 7.24 (q, J = 1.7 Hz, 0H), 7.06 (q, J = 1.6 Hz, 1H), 6.98 (dt, J = 6.9, 1.3 Hz, 1H), 6.92 (t, J = 1.9 Hz, 1H), 6.87 (t, J = 1.9 Hz, 1H), 4.41 (q, J = 1.5 Hz, 2H), 4.37 (q, J = 1.4 Hz, 2H) ppm; ^{13}C {^{1}H} NMR (151 MHz, $CDCl_3$) δ = 136.3, 134.9, 134.8, 134.2, 134.0, 132.2, 129.7, 129.5, 129.1, 128.8, 128.1, 128.0, 127.7, 127.4, 126.5, 126.3, 126.2, 125.6, 125.4, 125.3, 125.1, 122.9 (2C), 120.4, 41.2, 40.8 ppm; HRMS (EI) *m/z*: $[^{12}C_{13}{}^{1}H_{8}{}^{79}Br^{81}Br]^+$ calcd. 323.8972, found 323.8975.

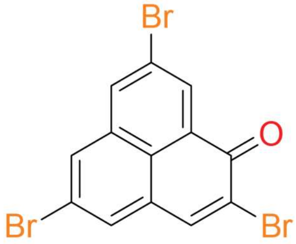

2-5

2,5,8-tribromophenalenone (**2-5**) A 25 mL round bottom flask was charged with a stir bar, 5,8-dibromophenalenone (**2-4a**) (40 mg, 118 μmol), and dichloromethane (4 mL). The reaction mixture was cooled to 0 °C and bromine (25 mg, 154 μmol, 25 mg/mL in CH_2Cl_2) was added over the course of 5 min with stirring. The mixture was stirred overnight, allowing the reaction to warm to 24 °C. Triethylamine (22 mg, 213 μmol, 1 g/mL in CH_2Cl_2) was added at once and the reaction was stirred at 24 °C for 1 h. The reaction mixture was diluted with CH_2Cl_2 (5 mL), quenched with aqueous sodium sulfite (10% w/v), and the organic phase separated. The aqueous phase was extracted with CH_2Cl_2 (50 mL), and the combined organic phases were washed with aqueous sodium sulfite (10% w/v), saturated aqueous sodium bicarbonate, saturated aqueous sodium chloride, dried over magnesium sulfate, and filtered over a short plug of silica gel using CH_2Cl_2 as eluent. The solution was concentrated on a rotary evaporator. Column chromatography (SiO_2, 40% CH_2Cl_2) to isolate the product from trace impurities and starting material yielded 2,5,8-tribromophenalenone (**2-5**) (49 mg, 118 μmol, quant.) as a yellow powder. ^{1}H NMR (700 MHz, $CDCl_3$) δ = 8.74 (d, J = 2.0 Hz, 1H), 8.30 (d, J = 2.0 Hz, 1H), 8.21–8.09 (m, 2H), 7.83 (d, J = 1.8 Hz, 1H) ppm; ^{13}C {^{1}H} NMR (151 MHz, $CDCl_3$) δ 177.6, 141.9, 136.1, 135.0, 134.6, 134.0, 132.6, 129.8, 129.7, 127.1, 124.0, 123.0, 121.9 ppm.

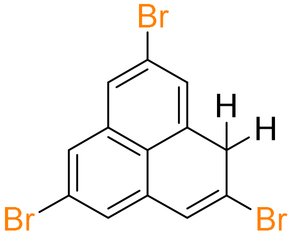

2-2

2,5,8-tribromophenalene (**2-2**) A 100 mL oven-dry Schlenk flask was charged under N_2 with a stir bar, 2,5,8-tribromophenalenone (**2-5**) (86 mg, 206 μmol), and degassed benzene (anhydrous, 15 mL). DIBAL-H (1 M in heptane, 1 mL, 1 mmol) was added dropwise over 6 min by syringe stirring, during which the inhomogeneous yellow suspension became brownish, then a homogeneous pale yellow after approximately one equivalent of DIBAL-H was added, then transitioned to a pale pink solution. A cold finger was affixed to the Schlenk flask, and the reaction mixture heated to 80 °C overnight. After heating for 18 h, the reaction was cooled, the cold finger replaced with a rubber septum and the reaction was quenched by addition via syringe of degassed saturated aqueous ammonium chloride (10 mL), yielding a brown suspension and gelatinous salts. The mixture was stirred for 30 minutes to promote disproportionation of phenalenol into phenalene and phenalenone. The reaction was extracted with degassed Et_2O 4 × 15 mL by vigorous stirring in the reaction vessel followed by cannulating off the organic layer into a 100 mL Schlenk tube under N_2 with stir bar. The solution was concentrated by in-line distillation under N_2. The crude mixture was transferred to a glovebox for analysis. NMR spectroscopy revealed more than two components, though it was expected that the spectrum would be clearly distinguishable into phenalenone peaks and phenalene peaks. Thin layer chromatography under nitrogen atmosphere using florisil TLC plates revealed a dark, UV-active spot with $R_f = 0$ in hexanes and a faintly UV active spot (dark orange, longwave irradiation) with $R_f \approx 0.25$. The crude material was dissolved in hexanes and filtered over a short plug of florisil under N_2 atmosphere. TLC of the eluent revealed only the dark baseline spot and NMR spectroscopy revealed a nearly identical spectrum. In hindsight it was determined that the residual oxygen in the glovebox (30 ppm) was too high for the small scale, micromolar reaction and that Schlenk technique should have been used instead, as was used in the synthesis of 2,5-dibromophenalene (**2-1**). In addition to phenalene and phenalenone, the NMR samples likely contained intermediates in the oxidation of the target product, 2,5,8-tribromophenalene, which is hypothesized in the literature to proceed via a peroxide intermediate.

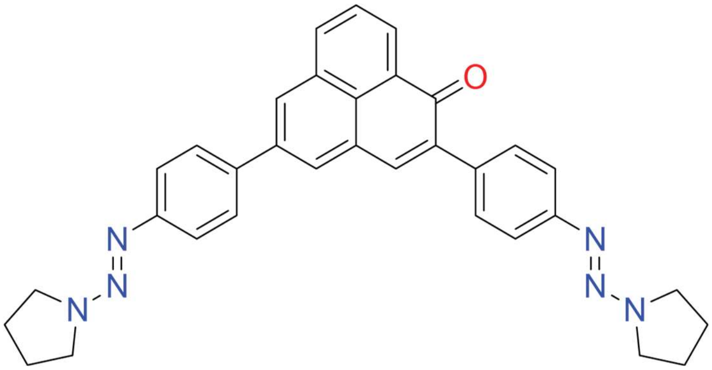

2-8

2,5-bis(N-pyrorrolidinyl-4-phenyl-azo)phenalenone (**2-8**) A 100 mL Schlenk tube was charged with a stir bar, 2,5-dibromophenalenone (**2-4**) (338 mg, 1 mmol), N-pyrrolidinyl-4-phenyl-azo-boronic acid pinacol ester (**2-7**) (3 mmol, 861 mg), and tribasic potassium phosphate (4 mmol, 849 mg). The tube was evacuated and backfilled with N_2 three times. Dioxane (30 mL) and water (3 mL) were added by syringe and the mixture was sparged with N_2 for 30 min. Tetrakis(triphenylphosphine)palladium(0) was added and a cold finger was affixed. The reaction was heated with stirring to 100 °C with flow of 24 °C water through the cold finger for 18 hours, during which time the inhomogeneous yellow mixture transitioned to a homogeneous red. The reaction was cooled to 24 °C and quenched with aqueous ammonium chloride (1 M, 30 mL). The reaction was extracted with CH_2Cl_2 3 × 50 mL. The combined organic phase was washed with saturated aqueous sodium bicarbonate and saturated aqueous sodium chloride, then dried over sodium sulfate and filtered over a short plug of silica gel using CH_2Cl_2 as eluent. The filtrate was concentrated on a rotary evaporator. Column chromatography (SiO_2; hexane/ CH_2Cl_2/Et_2O gradient 50:50:0 to 35:65:5 then 325:625:50 to 295:625:80) yielded 2,5-bis(N-pyrorrolidinyl-4-phenyl-azo)phenalenone (**2-8**) (418 mg, 0.793 mmol, 79%) as a red powder. ^{1}H NMR (500 MHz, $CDCl_3$) δ = 8.68 (d, J = 7.3 Hz, 1H), 8.25 (d, J = 8.0 Hz, 1H), 8.19 (d, J = 1.7 Hz, 1H), 8.08 (d, J = 1.7 Hz, 1H), 7.94 (s, 1H), 7.82 (t, J = 7.7 Hz, 1H), 7.73 (dd, J = 10.0, 7.9 Hz, 4H), 7.57 (d, J = 8.5 Hz, 2H), 7.52 (d, J = 8.3 Hz, 2H), 3.83 (br s, 8H), 2.05 (q, J = 6.3, 5.5 Hz, 8H) ppm;^{13}C {1H} NMR (151 MHz, $CDCl_3$) δ = 184.5, 151.5 (2C), 139.8, 139.4, 139.0, 136.5, 134.8, 133.5, 132.7, 130.8, 130.6, 130.1, 129.8, 128.9, 128.1, 127.9, 127.7, 126.3, 121.2, 120.3, 24.0 ppm.

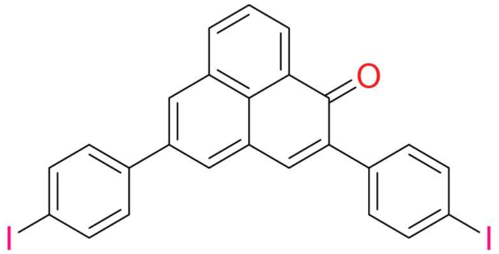

BP-2-1

2,5-bis(4-iodophenyl)phenalenone (**BP-2-1**) A 10 mL oven-dry sealable tube was charged with a stir bar and 2,5-bis(N-pyrorrolidinyl-4-phenyl-azo)phenalenone (**2-8**) (1.5 mmol, 790 mg). The tube was flushed with a continuous stream of N_2 for 30 min. Methyl iodide was degassed separately and an excess quantity (3 mL) was added to the sealable tube by syringe. The sealable tube was sealed and heated with stirring to 100 °C behind a blast shield for 24 h. During heating, the inhomogeneous yellow mixture transitioned to a homogeneous red. Methyl iodide was removed by in-line vacuum distillation and quenched with aqueous sodium hydroxide. The solid reaction residue was extracted with CH_2Cl_2 and filtered over a short plug of silica gel using CH_2Cl_2 as eluent. Column chromatography (SiO_2; hexane/ CH_2Cl_2 45:55) yielded 2,5-bis(4-iodophenyl)phenalenone (**BP-2-1**) in two portions: 125 mg >97% purity and 246 mg ~70% purity. The primary contaminant was a species equivalent to the desired product with an additional methyl group on the periphery of the phenalenone core, based on NMR analysis. The two samples were subjected to recrystallizations in hot toluene (~0.4 mL/mg, 95 °C). After cooling slowly to 24 °C, the samples were cooled further to 5 °C, filtered, and rinsed with small portions of toluene (5 °C). The less pure sample was subjected to recrystallization conditions twice. This process afforded pure 2,5-bis(4-iodophenyl)phenalenone (**BP-2-1**) (206 mg, 0.353 mmol, 23%) as yellow needle-like crystals. ^1H NMR (500 MHz, $CDCl_3$) δ = 8.70 (dd, J = 7.3, 1.2 Hz, 1H), 8.29 (dd, J = 8.2, 1.2 Hz, 1H), 8.19 (d, J = 1.7 Hz, 1H), 8.02 (d, J = 1.7 Hz, 1H), 7.91 (s, 1H), 7.90 – 7.83 (m, 3H), 7.83 – 7.79 (m, 2H), 7.50 (d, J = 8.4 Hz, 2H), 7.46 (d, J = 8.4 Hz, 2H) ppm; ^{13}C $\{^1H\}$ NMR (151 MHz, $CDCl_3$) δ 183.7, 139.5, 139.4, 139.0 (2C), 138.4, 137.5, 136.0, 135.1, 132.6, 131.2, 131.0, 130.8, 129.8, 129.2, 129.1, 128.8, 128.1, 126.7, 94.4, 94.2 ppm; HRMS (ESI FTMS) *m/z*: $[^{12}C_{25}{}^1H_{16}{}^{16}O^{127}I_2]^+$ calcd. 584.9207, found 584.9204.

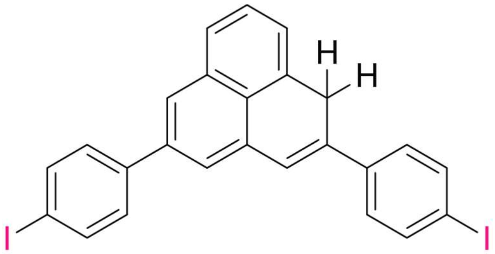

2,5-bis(4-iodophenyl)phenalene A 50 mL oven-dry Schlenk tube was charged under N_2 with a stir-bar and 2,5-bis(4-iodophenyl)phenalenone (**BP-2-1**) (0.25 mmol, 146 mg). Degassed benzene (8 mL) was added by syringe. DIBAL-H (1 M in heptane, 0.5 mL, 0.5 mmol) was added slowly over 20 min by syringe pump. The yellow inhomogeneous mixture transitioned to a rusty brown, then to a homogeneous red solution, then eventually reverted to an inhomogeneous yellow. A cold finger was affixed to the Schlenk flask, and the reaction mixture heated with stirring to 80 °C overnight. After heating for 18 h, the reaction was cooled, the cold finger replaced with a rubber septum and the reaction was quenched by addition via syringe of degassed saturated aqueous ammonium chloride (10 mL), yielding a brown suspension and gelatinous salts. The mixture was diluted with degassed hexane (10 mL) and stirred for 30 min to promote disproportionation of phenalenol into phenalene and phenalenone. The reaction was extracted with degassed hexane 4 × 15 mL by vigorous stirring in the reaction vessel followed by cannulating off the organic layer into a 100 mL Schlenk tube under N_2. The organic phase was washed under N_2 with degassed saturated aqueous ammonium chloride and the organic phase taken up by syringe and then dispensed through syringe filter (PTFE, 0.20 µm) into a separate N_2-purged 100 mL Schlenk tube with stir bar. The solution was concentrated by in-line vacuum distillation under N_2. Column chromatography (florisil; degassed hexane; nitrogen gas) revealed that unlike 2,5-dibromophenalene (**2-1**), hexane eluent did not separate the reduced product from the oxidized portion of the disproportionate. Adding small amounts of Et_2O and monitoring elution by longwave UV did not allow separation of the product, as the phenalenone and phenalene ran together. In retrospect, it is possible that a faulty pump resulted in failure to exclude oxygen from the reaction and workup and phenalene product may have been present in only small amounts (its presence was confirmed by characteristic signals in the measured ^{1}H NMR spectrum. Ultimately, on-surface synthesis was used to chemically reduce the cross-coupled poly[phenalenone-2,5-diyl-*alt*-[1,1'-biphenyl]-4,4'-diyl] *in situ* at the gold-vacuum interface in the preparatory chamber of the scanning tunneling microscope. If 2,5-bis(iodophenyl)phenalene is a desired material, it may be worth repeating this experiment.

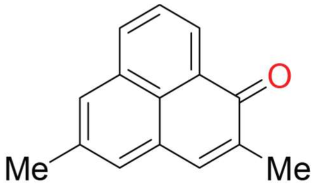

2-9

2,5-dimethylphenalenone (**2-9**) A 25 mL Schlenk flask was charged with 2,5-dibromophenalenone (**2-4**) (0.75 mmol, 254 mg), tribasic potassium phosphate (3 mmol, 637 mg), and a stir bar. The system was evacuated and backfilled with N_2 twice. Trimethylboroxine (7.5 mmol, 1.05 mL), dioxane (7.5 mL) and water (0.75 mL) were added by syringe and the system degassed by two freeze-pump-thaw cycles. [1,1′-Bis(diphenylphosphino)ferrocene]-dichloropalladium(II), complex with CH_2Cl_2 (0.075 mmol, 61 mg) was added and the system degassed by three additional freeze-pump-thaw cycles. The reaction flask was heated with stirring to 80 °C for 18 h, over which period the reaction remained an inhomogeneous yellow mixture. The reaction mixture was cooled, quenched by the addition of water, and extracted with CH_2Cl_2 (3 × 25 mL). The combined organic phase was washed with aqueous hydrochloric acid (2 M, 50 mL), saturated aqueous sodium chloride (50 mL), dried over magnesium sulfate, and filtered over a short plug of silica using CH_2Cl_2 as eluent. The filtrate was concentrated on a rotary evaporator. Column chromatography (SiO_2; hexane/ CH_2Cl_2 1:3) yielded 2,5-dimethylphenalenone (**2-9**) as a yellow powder (0.552 mmol, 115 mg, 74%). ^{1}H NMR (500 MHz, $CDCl_3$) δ = 8.57 (dd, J = 7.3, 1.2 Hz, 1H), 8.09 (dd, J = 8.0, 1.2 Hz, 1H), 7.76 – 7.71 (m, 1H), 7.73 (t, J = 7.7 Hz, 1H), 7.56 (q, J = 1.4 Hz, 1H), 7.51 (d, J = 1.6 Hz, 1H), 2.56 (d, J = 1.0 Hz, 3H), 2.23 (d, J = 1.4 Hz, 3H) ppm; ^{13}C {^{1}H} NMR (126 MHz, $CDCl_3$) δ 186.1, 138.4, 137.1, 136.5, 134.0, 132.5, 132.4, 129.8, 129.6, 129.2, 128.2, 127.2, 126.1, 21.7, 16.3 ppm.

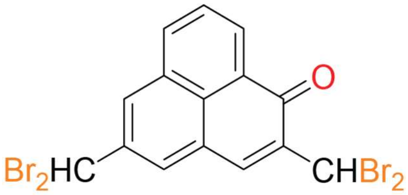

CC-2-1

2,5-bis(dibromomethyl)phenalenone (**CC-2-1**) A 10 mL Schlenk flask was charged with 2,5-dimethylphenalenone (**2-9**), (0.15 mmol, 31 mg), N-bromosuccinimide (0.96 mmol, 171 mg), dibenzoyl peroxide (catalytic amount, 2 mg), and a stir bar. A jacketed reflux condenser was affixed and capped with a septum. The system was evacuated and backfilled with N_2 three times. Degassed $CHCl_3$ (3 mL) was added by syringe. 24 °C water was cycled through the jacketed reflux condenser, the Schlenk arm of the flask was closed, and N_2 flow was established through the septum of the reflux condenser via syringe needle. The reaction was heated with stirring to 75 °C for 18 h, over which time the reaction transitioned from an inhomogeneous yellow to an inhomogeneous yellow-orange. The reaction mixture was cooled, diluted with $CHCl_3$ (10 mL), and washed with aqueous sodium bisulfite (0.1 M, 25 mL), then dried with magnesium sulfate, filtered over a short plug of silica using $CHCl_3$ as eluent, and concentrated on a rotary evaporator. Column chromatography (SiO_2; hexane/CH_2Cl_2 1:1, 500 mL; 11:0, 1 L) yielded 2,5-bis(dibromomethyl)phenalenone (**CC-2-1**) as a yellow powder (0.0218 mmol, 11.4 mg, 14.5%).^{1}H NMR (400 MHz, $CDCl_3$) $\delta = 8.70$ (dd, $J = 7.4, 1.2$ Hz, 1H), 8.45 (s, 1H), 8.27 (s, 1H), 8.27 – 8.23 (m, 1H), 8.10 (d, $J = 1.8$ Hz, 1H), 7.87 (t, $J = 7.8$ Hz, 1H), 7.14 (s, 1H), 6.85 (s, 1H) ppm;^{13}C {^{1}H} NMR (126 MHz, $CDCl_3$) $\delta = 180.3$, 141.6, 140.7, 140.4, 135.6, 132.5, 131.9, 131.2, 128.8, 128.7, 128.6, 128.2, 127.6, 39.5, 35.1 ppm; HRMS (ESI FTMS) *m/z*: $[^{12}C_{15}{}^{1}H_{9}{}^{16}O^{79}Br_{4}]^{+}$ calcd 520.7381, found 520.7380.

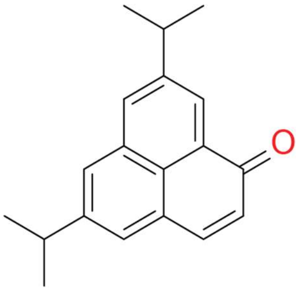

Ph-2-1

5,8-diisopropylphenalenone (**Ph-2-1**) A 2–5 mL microwave tube was charged with a stir bar, 2-isopropyl-propane-1,2,3-triol (**2-11**), (403 mg, 3 mmol), 6-isopropyl-2-naphthol (**2-12**) (112 mg, 0.6 mmol), boric acid (52 mg, 0.84 mmol), sodium 3-nitrobenzenesulfonate (135 mg, 0.6 mmol), iron sulfate heptahydrate (33 mg, 0.12 mmol), and concentrated sulfuric acid (0.6 mL). The microwave tube was sealed and heated with stirring to 130 °C by microwave irradiation for 30 min. The dark, viscous crude material was diluted with water and neutralized to pH 7 with aqueous potassium hydroxide (20% w/v). The inhomogeneous aqueous mixture was filtered under vacuum overnight. The aqueous filtrate was extracted with Et_2O (2 × 100 mL), and the dark filter cake was Soxhlet extracted with Et_2O (400 mL) for 72 h. The liquid-liquid extract was combined with the golden Soxhlet extract solution and polar impurities were removed by filtration over a short plug of silica gel using Et_2O as eluent. The filtrate was then concentrated on a rotary evaporator. Column chromatography (SiO_2; CH_2Cl_2) yielded 5-bromophenalenone (**Ph-2-1**) (33 mg, 0.12 mmol, 21%) as an orange oily solid. ^{1}H NMR (700 MHz, $CDCl_3$) $\delta = 8.50$ (d, $J = 1.8$ Hz, 1H), 7.99 (d, $J = 1.8$ Hz, 1H), 7.81 (d, $J = 1.6$ Hz, 1H), 7.73 (d, $J = 9.7$ Hz, 1H), 7.61 (d, $J = 1.6$ Hz, 1H), 6.72 (d, $J = 9.7$ Hz, 1H), 3.20 (hept, $J = 6.9$ Hz, 1H), 3.12 (hept, $J = 6.9$ Hz, 1H), 1.39 (t, $J = 7.4$ Hz, 12H) ppm.

6.3 Chapter 3 supplement

6.3.1 Previously synthesized compounds

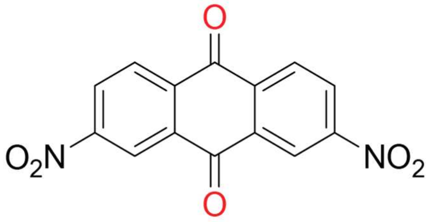

3-3

2,7-dibromoanthraquinone (**3-3**),[217] 33% yield. ^{1}H NMR (500 MHz, $CDCl_3$) δ = 9.19 (d, *J* = 2.3 Hz, 2H), 8.68 (dd, *J* = 8.5, 2.3 Hz, 2H), 8.58 (d, *J* = 8.4 Hz, 2H) ppm.

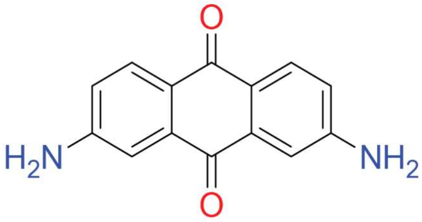

3-4

2,7-dinitroanthraquinnone (**3-4**),[217] 98% yield.^{1}H NMR (500 MHz, DMSO) δ = 7.83 (d, *J* = 8.5 Hz, 2H), 7.22 (d, *J* = 2.4 Hz, 2H), 6.88 (dd, *J* = 8.5, 2.4 Hz, 2H), 6.39 (s, 4H) ppm.

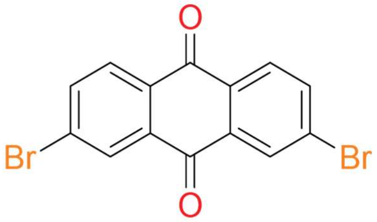

B3

2,7-dibromoanthraquinone (**3-5**),[217] 70% yield. ^{1}H NMR (500 MHz, $CDCl_3$) δ = 8.43 (d, *J* = 2.1 Hz, 2H), 8.18 (d, *J* = 8.3 Hz, 2H), 7.95 (dd, *J* = 8.3, 2.0 Hz, 2H) ppm.

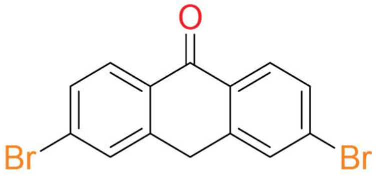

3-6

3,6-dibromo-9-anthrone (**3-6**),[218] 60% yield.^{1}H NMR (500 MHz, $CDCl_3$) δ 8.20 (dd, *J* = 8.6, 1.4 Hz, 2H), 7.64 (d, *J* = 1.6 Hz, 2H), 7.61 (ddd, *J* = 8.3, 2.1, 1.1 Hz, 2H), 4.31 (s, 2H) ppm.

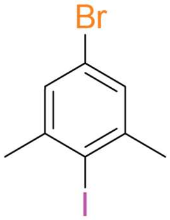

3-6

4-bromo-2-iodo-m-xylene (**3-6**),[211] 71% yield. ^{1}H NMR (500 MHz, $CDCl_3$) δ = 7.20 (s, 2H), 2.44 (s, 6H) ppm.

6.3.2 Synthetic procedures

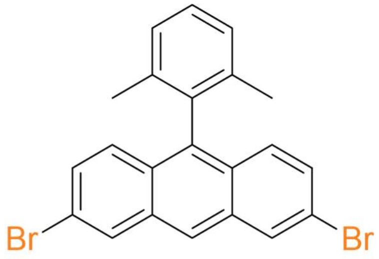

3-1

2,7-dibromo-10-(m-xyl-2-yl)anthracene (**3-1**),[219]adapted procedure. A 100-mL Schlenk flask was charged with 2-bromo-*m*-xylene (279.12 mg, 1.5 mmol) and a stir bar. Et_2O (anhydrous, 10 mL). The solution was cooled to –78 °C and *t*-butyllithium (1.7 M in hexanes, 1.76 mL, 3 mmol) was added dropwise by syringe and the mixture stirred at –78 °C for 15 min. To the colorless mixture was added toluene (anhydrous, 10 mL) and the mixture heated to 60 °C, over which period the colorless mixture transitioned to green-yellow. 3,6-dibromo-9-anthrone (**3-6**) (352 mg, 1 mmol) was dissolved in toluene (anhydrous, 20 mL), and added to the hot mixture over the course of 20 min, during which time the green-yellow mixture transitioned to an orange hue before reaching a darker orange-brown. The reaction was stirred at 60 °C for 1 h before cooling to 24 °C. Aqueous hydrochloric acid (concentrated, 2 mL) was added dropwise by pipette, over which time the mixture lightened from orange to yellow and became at first turbid, and then less turbid as addition of hydrochloric acid was completed. The mixture was stirred vigorously for 10 min under N_2 to promote dehydration and aromatization. The reaction mixture was diluted with water and extracted with hexanes (3 × 30 mL). The combined organic phase was washed with saturated aqueous sodium bicarbonate (100 mL) and saturated aqueous sodium chloride (100 mL), dried over magnesium sulfate, and concentrated on a rotary evaporator, yielding an orange solid. Column chromatography (SiO_2, hexanes, N_2 gas) yielded 2,7-dibromo-10-(*m*-xyl-2-yl)anthracene (**3-1**) as a colorless powder (0.51 mmol, 225 mg, 51%). ^{1}H NMR (500 MHz, CDCl3) $\delta = 8.28$ (s, 1H), 8.22 (d, J = 1.9 Hz, 2H), 7.39 (dd, J = 9.3, 2.0 Hz, 2H), 7.37 (t, J = 7.7 Hz, 1H), 7.31 (d, J = 9.2 Hz, 2H), 7.26 (d, J = 7.7 Hz, 2H), 1.72 (s, 6H) ppm.

6.4 Chapter 4 supplement

6.4.1 Previously synthesized compounds

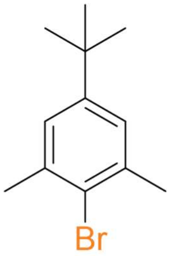

4-3

2-bromo-4-t-butyl-m-xylene (**4-3**),[220] 63% yield. ^{1}H NMR (400 MHz, $CDCl_3$) $\delta = 7.09$ (s, 2H), 2.41 (s, 6H), 1.29 (s, 9H) ppm.

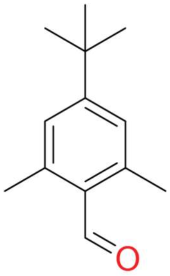

4-4

4-t-butyl-m-xylene-2-carbaldehyde (**4-4**), 97% yield. ^{1}H NMR (400 MHz, CDCl$_3$) δ = 10.58 (s, 1H), 7.09 (s, 2H), 2.62 (s, 6H), 1.32 (s, 9H) ppm.

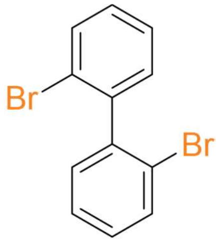

4-5

2,2'-dibromo-[1,1'-biphenyl] (**4-5**),[221] 86% yield.^{1}H NMR (400 MHz, CDCl$_3$) δ = 7.67 (dd, *J* = 8.2, 1.1 Hz, 2H), 7.38 (td, *J* = 7.5, 1.2 Hz, 2H), 7.30–7.22 (m, 4H) ppm.

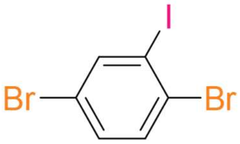

4-9

1,4-dibromo-2-iodobenzene (**4-9**), 63% yield,[222] 31% yield.[223] ^{1}H NMR (500 MHz, CDCl$_3$) δ = 7.99 (d, *J* = 2.3 Hz, 1H), 7.47 (d, *J* = 8.5 Hz, 1H), 7.33 (dd, *J* = 8.5, 2.3 Hz, 1H) ppm.

6.4.2 Synthetic procedures

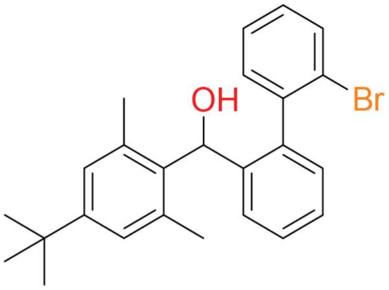

4-6

α-(5-t-butyl-m-xyl-2-yl)-(2'-bromo-[1,1'-biphenyl])-2-methanol (**4-6**) An oven-dried 500 mL Schlenk flask was charged with 2,2'-[1,1'-dibromobiphenyl] (**4-5**) (25 mmol, 7.80g) and a stir bar. Tetrahydrofuran (anhydrous, 125 mL) was added by syringe and the solution was cooled to –78 °C. *n*-butyllithium (2.5 M in hexanes, 25 mmol,10 mL) was added by syringe over the course of 10 min. The mixture was stirred at –78 °C for 30 min and then 4-*t*-butyl-*m*-xylene-2-carbaldehyde (**4-4**) (26.25 mmol, 5.00 g) dissolved in tetrahydrofuran (anhydrous, 12.5 mL) was added over the course of 8 min. The reaction mixture was stirred for 18 h, allowing the reaction to warm to 24 °C. The reaction was quenched with saturated aqueous ammonium chloride, diluted with water to dissolve the water-soluble precipitate, and the organic phase separated. The aqueous phase was extracted with Et_2O (2 × 80 mL). The combined organic phases were washed with saturated aqueous NaCl solution, dried over sodium sulfate, filtered, and concentrated on a rotary evaporator, yielding a hard, tacky, pale yellow oil. Column chromatography (SiO_2, Et_2O:hexanes 3:17) yielded α-(5-t-butyl-m-xyl-2-yl)-(2'-bromo-[1,1'-biphenyl])-2-methanol (**4-6**) as a hard, tacky, colorless oil (24.8 mmol, 10.52 g, 99%). ^{1}H NMR spectroscopy revealed two diastereomeric rotamers in 1:0.5 ratio and a small amount of debrominated product (1:0.5:0.04). ^{13}C NMR spectroscopy likewise revealed double the number of expected carbons. ^{1}H NMR (700 MHz, $CDCl_3$) δ = 7.91 (dd, J = 8.0, 1.5 Hz, 1H), 7.51 (dd, J = 8.0, 1.4 Hz, 1.5H), 7.48 – 7.42 (m, 1.5H), 7.37 (dd, J = 7.5, 1.7 Hz, 0.5H), 7.35 (td, J = 7.8, 7.6, 1.5 Hz, 0.5H), 7.32 (tdd, J = 7.4, 2.9, 1.4 Hz, 2H), 7.16 – 7.09 (m, 1H), 7.01 (td, J = 7.8, 1.7 Hz, 1H), 6.98 (dd, J = 7.5, 1.4 Hz, 1H), 6.87 (s, 1H), 6.77 (td, J = 7.5, 1.4 Hz, 1H), 6.74 (s, 2H), 6.36 (dd, J = 7.6, 1.7 Hz, 1H), 6.18 (d, J = 4.0 Hz, 0.5H), 6.14 (d, J = 3.6 Hz, 1H), 2.11 (s, 3H), 1.96 (s, 6H), 1.88 (d, J = 3.6 Hz, 1H), 1.81 (d, J = 4.2 Hz, 0.5H), 1.27 (d, J = 1.2 Hz, 4.5H), 1.25 (d, J = 1.1 Hz, 9H) ppm; ^{13}C {^{1}H}NMR (151 MHz, $CDCl_3$) δ = 150.4, 150.2, 142.3, 142.2, 141.6, 140.4, 140.2, 139.2, 136.9 (2C), 136.3, 134.9, 132.8, 131.9, 131.6, 130.9, 130.8, 129.9, 128.7, 128.4, 127.7 (2C), 127.5, 126.9, 126.8, 126.7, 126.6, 126.5, 126.4, 126.1, 123.9, 123.3, 70.9, 70.4, 34.3, 34.2, 31.4 (2C), 21.7, 21.0 ppm.

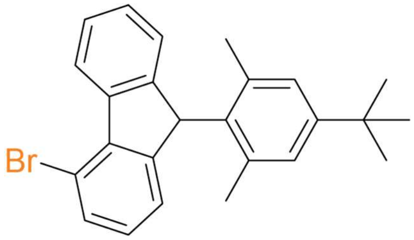

4-7

4-bromo-9-(5-t-butyl-m-xyl-2-yl)fluorene (**4-7**) α-(5-t-butyl-m-xyl-2-yl)-(2'-bromo-[1,1'-biphenyl])-2-methanol (**4-6**) (13.8 mmol), 5.86 g) in a 100 mL round bottom flask was dissolved in CH_2Cl_2 (anhydrous, 50 mL) and cannulated into an oven-dry 1 L Schlenk flask with stir bar. CH_2Cl_2 (anhydrous, 300 mL) was cannulated into the 1 L Schlenk flask. The solution was cooled to 0 °C with stirring and boron trifluoride diethyl etherate (69.2 mmol, 8.54 mL) was added over 10 min by syringe pump. The colorless solution transitioned to a deep purple. The reaction was stirred at 0 °C for 15 min and then the ice bath was removed, and the reaction was stirred at 24 °C for an additional 45 min. The reaction mixture was then cooled to 0 °C and the reaction was quenched with saturated aqueous sodium bicarbonate. The organic phase was separated, and the aqueous phase was extracted with dichloromethane (100 mL). The combined organic phase was washed with saturated aqueous NaCl solution and dried over magnesium sulfate, before being filtered over a short plug of silica using CH_2Cl_2 as eluent. The eluent was concentrated on a rotary evaporator, yielding 4-bromo-9-(5-t-butyl-m-xyl-2-yl)fluorene (**4-7**) (13.0 mmol, 5.26 g) as a colorless powder. ^{1}H NMR (400 MHz, $CDCl_3$) δ = 8.67 (dt, J = 7.8, 0.9 Hz, 1H), 7.54 (dt, J = 7.8, 1.0 Hz, 1H), 7.44 (tt, J = 7.8, 1.1 Hz, 1H), 7.31 (td, J = 7.4, 1.1 Hz, 1H), 7.23 (dq, J = 7.4, 1.0 Hz, 1H), 7.17 (dt, J = 7.4, 1.6 Hz, 1H), 7.16 (s, 1H), 7.08 (t, J = 7.6 Hz, 1H), 6.81 (d, J = 2.2 Hz, 1H), 5.49 (s, 1H), 2.68 (s, 3H), 1.30 (s, 9H), 1.11 (s, 3H) ppm; ^{13}C {^{1}H}NMR (151 MHz, $CDCl_3$) δ = 150.4, 149.7, 147.9, 140.3, 139.2, 137.3 (2C), 133.4, 131.9, 128.0, 127.9, 127.0, 126.7, 125.2, 124.1, 123.7, 123.2, 117.2, 50.1, 34.3, 31.5, 22.2, 19.3 ppm.

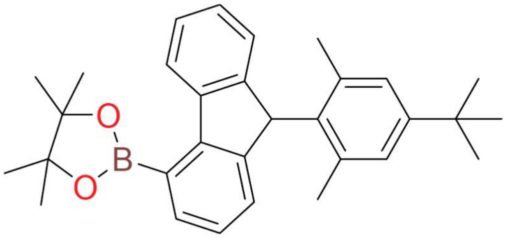

4-8

9-(5-t-butyl-m-xyl-2-yl)fluorene-4-boronic acid pinacol ester (**4-8**) A 100 mL oven-dry Schlenk flask was charged with a stir bar and oven-dry potassium acetate (20 mmol, 1.96 g) and cooled by repeated evacuating and back-filling with N_2 twice. 4-bromo-9-(5-t-butyl-m-xyl-2-yl)fluorene (**4-7**) (10 mmol, 4.05 g), bis(pinacolato)diboron (20 mmol, 5.08 g), and [1,1′-Bis(diphenylphosphino)ferrocene]-dichloropalladium(II), complex with CH_2Cl_2 (0.5 mmol, 408 mg) were added. The flask was evacuated and backfilled with N_2 thrice more. Dioxane (anhydrous, degassed, 25 mL) was added by syringe and the reaction mixture was heated to 90 °C. After 18 h the reaction was cooled to 24 °C and quenched with water (50 mL) and then extracted with CH_2Cl_2 (3 × 50 mL). The combined organic phase was dried over magnesium sulfate and concentrated by rotary evaporator. The crude material was dissolved in hexanes and filtered over a short plug of silica using hexanes as eluent to remove debrominated starting material. Et_2O/hexanes (3:7) was then used to elute the product, yielding a colorless solid that, according to ^{1}H NMR contained bis(pinacolato)diboron in addition to the desired product. The crude mixture was recrystallized by dissolving in hot MeOH (30 mL, 50 °C) and then cooling to 5 °C, yielding 9-(5-t-butyl-m-xyl-2-yl)fluorene-4-boronic acid pinacol ester (**4-8**) (4.46 mmol, 2.02 g, 44.6%) as colorless flaky crystals. ^{1}H NMR (400 MHz, $CDCl_3$) δ = 8.77 (dt, J = 7.9, 0.9 Hz, 1H), 7.83 (dt, J = 7.2, 1.2 Hz, 1H), 7.37 (dddd, J = 7.8, 6.9, 1.7, 0.8 Hz, 1H), 7.29 (dt, J = 7.5, 1.2 Hz, 1H), 7.26 – 7.18 (m, 3H), 7.16 (d, J = 2.2 Hz, 1H), 6.79 (d, J = 2.2 Hz, 1H), 5.42 (s, 1H), 2.69 (s, 3H), 1.49 (s, 6H), 1.48 (s, 6H), 1.30 (s, 9H), 1.09 (s, 3H) ppm; ^{13}C NMR (151 MHz, $CDCl_3$) δ = 149.2, 148.0, 147.7, 145.5, 142.2, 137.4, 137.3, 135.0, 134.1, 127.1, 126.8 (2C), 126.6, 126.1, 125.0, 124.1, 123.9, 84.2, 49.7, 34.3, 31.5, 25.2 (2C), 22.3, 19.4 ppm.

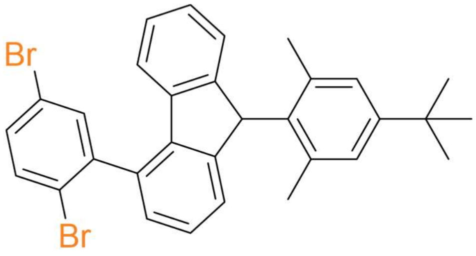

4-1

4-(2,5-diiodophenyl)- 9-(5-t-butyl-m-xyl-2-yl)fluorene (**4-1**) An oven-dried 25 mL sealable tube was charged with oven-dry cesium carbonate (11.8 mmol, 3.83 g) and a stir bar and cooled under vacuum. 9-(5-t-butyl-m-xyl-2-yl)fluorene-4-boronic acid pinacol ester (**4-8**) (4.7 mmol, 2.13 g), 1,4-dibromo-2-iodobenzene (**4-9**) (5.9 mmol, 2.13 g), and tetrakis(triphenylphosphine)palladium(0) were added to the Schlenk flask and the flask was evacuated and backfilled with N_2 thrice. Degassed dioxane (anhydrous, degassed, 16 mL) was added by syringe, and the tube was sealed. The reaction mixture was heated to 110 °C with stirring for 18 h. The reaction mixture was cooled and quenched with water and extracted with CH_2Cl_2 (3

× 50 mL). The combined organic phase was washed with saturated aqueous NaCl solution and dried over magnesium sulfate. Column chromatography (SiO2, Et_2O gradient 0.25% to 0.75% in hexanes) yielded 4-(2,5-diiodophenyl)- 9-(5-t-butyl-m-xyl-2-yl)fluorene (**4-1**) as a tacky, colorless foam (1.69 mmol, 945 mg, 36%) and 858 mg of impure material that co-eluted with impurities. Cooling the solid product to –20 °C allowed the material to be broken up into a workable colorless flaky solid. The product **4-1** exists at an equilibrium between diastereomeric rotamers in approximately 1:0.7 ratio, as reflected in the doubled NMR spectra. ^{1}H NMR (700 MHz, CDCl3) δ 7.64 (d, J = 6.5 Hz, 0.7H), 7.63 (d, J = 6.6 Hz, 1H), 7.61 (d, J = 2.5 Hz, 1H), 7.57 (d, J = 2.4 Hz, 0.7H), 7.50 (dd, J = 2.4, 1.0 Hz, 1H), 7.49 (dd, J = 2.4, 1.0 Hz, 0.7H), 7.32 – 7.27 (m, 3.4H), 7.22 (ddq, J = 7.5, 5.3, 1.1 Hz, 1.7H), 7.20 – 7.16 (m, 3.4H), 7.14 – 7.09 (m, 3.4H), 6.82 (dd, J = 10.3, 2.2 Hz, 1.7H), 6.71 (dt, J = 7.8, 0.9 Hz, 0.7H), 6.68 (dt, J = 7.8, 0.9 Hz, 1H), 5.56 (s, 0.7H), 5.51 (s, 1H), 2.72 (s, 4H), 2.72 (s, 3H), 2.72 (2, 2.1H), 1.31 (s, 6.3H), 1.31 (s, 9H), 1.19 (s, 3H), 1.14 (s, 2.1H) ppm; ^{13}C NMR (126 MHz, CDCl3) δ = 149.5, 149.4, 148.1, 147.9, 147.8, 147.7, 144.0 (2C), 140.4, 140.3, 138.5, 138.3, 137.4, 137.3, 137.2, 135.3, 134.9, 134.3 (2C), 134.0, 133.9 (2C), 133.8, (3C), 132.5, 128.9, 128.7, 128.6, 128.1 (2C), 127.3, 127.0, 126.9 (3C), 126.8, 125.2, 125.1, 124.4, 124.3 (3C), 123.1 (2C), 122.3 (2C), 121.5 (2C), 49.9, 49.7, 34.3 (2C), 31.5, 22.4, 22.3, 19.4, 19.3 ppm; HRMS (EI) *m*/*z*: [$^{12}C_{31}H_{28}{}^{79}Br^{81}Br$]+ calcd 560.0537, found 560.0537.

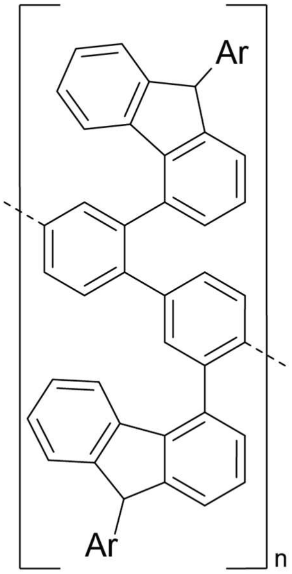

Poly-C8

An oven-dried 2–5 mL sealable microwave tube was charged with a stir bar, $Ni(COD)_2$, 1,4-cyclooctadiene, and 2,2'-bipyrydyl and sealed under N_2 atmosphere. Toluene (2 mL, anhydrous, degassed) and N,N-dimethyl formamide (0.67 mL, anhydrous, degassed) were added by syringe and the mixture heated to 60 °C for 30 min, generating a deep purple mixture. An oven-dry 2-neck pear-shaped flask was charged with a stir bar and 4-(2,5-diiodophenyl)- 9-(5-t-butyl-m-xyl-2-yl)fluorene (**4-1**) (100 µmol, 56 mg) and evacuated and backfilled with N_2 three times. Toluene (1 mL, anhydrous, degassed) and N,N-dimethyl formamide (1 mL, anhydrous, degassed) were added by syringe and the mixture was stirred until the starting material dissolved. The solution was transferred to the catalyst mixture by syringe. Light was excluded from the reaction by an aluminum foil tent and the temperature was increased to 80 °C. The mixture was heated with stirring for 18 h before cooling. The reaction mixture was filtered over celite, and the filter pad was washed with toluene. The solvents were removed by rotary evaporator and dried under vacuum overnight. The pale brown solid was dissolved in minimal CH_2Cl_2 and hexanes were added to induce precipitation. The suspension was filtered over polymer filter paper (0.20 µm, nylon membrane), the solid residue washed with hexanes, and the filtrate was concentrated on a rotary evaporator and dried under vacuum, yielding an off-white solid residue (14 mg). The solid residue was then washed with MeOH, then acetone and these filtrates discarded. The solid residue was then washed with CH_2Cl_2 to dissolve the pale brown residue and the filtrate was concentrated on a rotary evaporator and dried under vacuum, yielding a pale brown solid residue (22 mg). Gel permeation chromatography (GPC) and matrix-assisted laser desorption ionization mass spectrometry (MALDI-MS) revealed that these two samples contained the desired polymer in differing length distributions (hexane wash: lower M_w, dichloromethane wash: higher M_w).

6.5 Chapter 5 supplement

6.5.1 Previously synthesized compounds

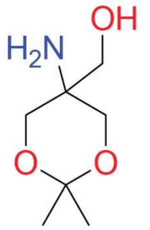

5-3

*(5-amino-2,2-dimethyl-1,3-dioxan-5-yl)*methanol (5-3).[224] ^1H NMR (500 MHz, CDCl3) δ = 3.78 (d, J = 11.9 Hz, 2H), 3.56 (d, J = 11.7 Hz, 2H), 3.51 (s, 1H), 2.70 (s, 3H), 1.43 (s, 3H), 1.40 (s, 3H) ppm.

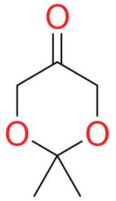

5-4

2,2-dimethyl-1,3-dioxan-5-one (**5-4**),[224] 39% yield (2 steps). ^1H NMR (500 MHz, $CDCl_3$) δ = 4.15 (d, J = 0.7 Hz, 4H), 1.45 (d, J = 0.7 Hz, 6H) ppm.

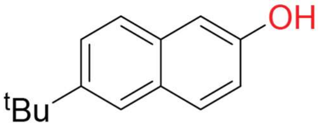

5-7

6-tert-butyl-2-naphthol (**5-7**),[225] reaction failed due to insufficiently anhydrous conditions.

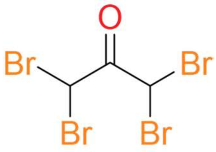

5-12

1,1,3,3-tetrabromoacetone (**5-12**), 96% yield. **Caution:** lachrymator. ^{1}H NMR (500 MHz, CDCl$_3$) δ = 6.30 (s, 2H) ppm.

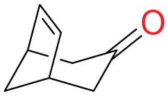

5-13

Bicyclo[3.2.1]oct-6-en-3-one (**5-13**),[226] unstable product. ^{1}H NMR (500 MHz, CDCl$_3$) δ = 6.01 (d, J = 1.5 Hz, 2H), 2.90 (dq, J = 5.2, 2.4 Hz, 2H), 2.44 (dd, J = 17.5, 3.6 Hz, 2H), 2.34 (dt, J = 18.3, 2.5 Hz, 2H), 2.08 (dtt, J = 10.6, 5.3, 2.6 Hz, 1H), 1.76 (d, J = 10.9 Hz, 1H) ppm.

6.5.2 Synthetic procedures

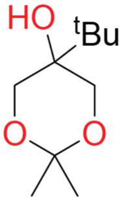

5-5

5-tert-butyl-2,2-dimethyl-1,3-dioxan-5-ol (**5-5**), adapted procedure,[227] 11% yield. ^{1}H NMR (500 MHz, CDCl$_3$) δ = 3.86 (d, J = 11.0 Hz, 2H), 3.78 (d, J = 11.0 Hz, 2H), 0.95 (s, 9H) ppm.

5-14

3-amino-bicyclo[3.2.1]oct-6-ene (**5-14**) An oven-dry 100 mL Schlenk flask was charged with bicyclo[3.2.1]oct-6-en-3-one (**5-13**) and a stir bar and degassed by evacuating and back-filling with N$_2$ three times. Ammonia (2.0 M in ethanol, anhydrous) was added by syringe and the mixture was stirred at 24 °C for 18 h. Sodium borohydride was added at once and the mixture was stirred at 24 °C for an additional 18 h. The reaction mixture was quenched with saturated aqueous ammonium chloride and extracted with Et$_2$O (3 × 25 mL). The combined organic phases were washed with saturated NaCl solution, dried over sodium sulfate, and concentrated on a rotary evaporator. NMR analysis of the crude material revealed that a single endo/exo-isomer was formed. The isomer was not identified, though the desired endo-isomer was predicted by steric considerations. The project was abandoned due to perceived infeasibility.

7 References

(1) Novoselov, K. S.; Geim, A. K.; Morozov, S. V.; Jiang, D.; Zhang, Y.; Dubonos, S. V.; Grigorieva, I. V.; Firsov, A. A. Electric Field Effect in Atomically Thin Carbon Films. *Science* **2004**, *306* (5696), 666–669.

(2) Lee, C.; Wei, X.; Kysar, J. W.; Hone, J. Measurement of the Elastic Properties and Intrinsic Strength of Monolayer Graphene. *Science* **2008**, *321* (5887), 385–388.

(3) Novoselov, K. S.; Geim, A. K.; Morozov, S. V.; Jiang, D.; Katsnelson, M. I.; Grigorieva, I. V.; Dubonos, S. V.; Firsov, A. A. Two-Dimensional Gas of Massless Dirac Fermions in Graphene. *Nature* **2005**, *438* (7065), 197–200.

(4) Novoselov, K. S.; Jiang, Z.; Zhang, Y.; Morozov, S. V.; Stormer, H. L.; Zeitler, U.; Maan, J. C.; Boebinger, G. S.; Kim, P.; Geim, A. K. Room-Temperature Quantum Hall Effect in Graphene. *Science* **2007**, *315* (5817), 1379–1379.

(5) Balandin, A. A.; Ghosh, S.; Bao, W.; Calizo, I.; Teweldebrhan, D.; Miao, F.; Lau, C. N. Superior Thermal Conductivity of Single-Layer Graphene. *Nano Lett.* **2008**, *8* (3), 902–907.

(6) Nair, R. R.; Blake, P.; Grigorenko, A. N.; Novoselov, K. S.; Booth, T. J.; Stauber, T.; Peres, N. M. R.; Geim, A. K. Fine Structure Constant Defines Visual Transparency of Graphene. *Science* **2008**, *320* (5881), 1308–1308.

(7) Geim, A. K. Graphene Prehistory. *Phys. Scr.* **2012**, *2012* (T146), 014003.

(8) Wallace, P. R. The Band Theory of Graphite. *Phys. Rev.* **1947**, *71* (9), 622–634.

(9) THE WORLD ACCORDING TO RICK. *Chem. Eng. News Arch.* **2006**, *84* (41), 13–19.

(10) Buseck, P. R.; Tsipursky, S. J.; Hettich, R. Fullerenes from the Geological Environment. *Science* **1992**, *257* (5067), 215–217.

(11) Cai, J.; Ruffieux, P.; Jaafar, R.; Bieri, M.; Braun, T.; Blankenburg, S.; Muoth, M.; Seitsonen, A. P.; Saleh, M.; Feng, X.; et al. Atomically Precise Bottom-up Fabrication of Graphene Nanoribbons. *Nature* **2010**, *466* (7305), 470–473.

(12) Faraday, M. XX. On New Compounds of Carbon and Hydrogen, and on Certain Other Products Obtained during the Decomposition of Oil by Heat. *Philos. Trans. R. Soc. Lond.* **1997**, *115*, 440–466.

(13) Heidelberg, E. E. Studien Über Die s. g. Aromatischen Säuren. *Justus Liebigs Ann. Chem.* **1866**, *137* (3), 327–359.

(14) Fawcett, E.; Trotter, J.; Robertson, J. M. The Crystal and Molecular Structure of Coronene. *Proc. R. Soc. Lond. Ser. Math. Phys. Sci.* **1997**, *289* (1418), 366–376.

(15) Seyler, H.; Purushothaman, B.; Jones, D. J.; Holmes, A. B.; Wong, W. W. H. Hexa-peri-hexabenzocoronene in organic electronics. *Pure Appl. Chem.* **2012**, *84* (4), 1047–1067.

(16) M. Adkins, E.; Houston Miller, J. Towards a Taxonomy of Topology for Polynuclear Aromatic Hydrocarbons: Linking Electronic and Molecular Structure. *Phys. Chem. Chem. Phys.* **2017**, *19* (41), 28458–28469.

(17) Prabhu, S.; Murugan, G.; Arockiaraj, M.; Arulperumjothi, M.; Manimozhi, V. Molecular Topological Characterization of Three Classes of Polycyclic Aromatic Hydrocarbons. *J. Mol. Struct.* **2021**, *1229*, 129501.

(18) Fan, W.; Han, Y.; Wang, X.; Hou, X.; Wu, J. Expanded Kekulenes. *J. Am. Chem. Soc.* **2021**, *143* (34), 13908–13916.

(19) Abbel, R.; Schenning, A. P. H. J.; Meijer, E. w. Fluorene-Based Materials and Their Supramolecular Properties. *J. Polym. Sci. Part Polym. Chem.* **2009**, *47* (17), 4215–4233.

(20) Kilymis, D.; P. Bartók, A.; J. Pickard, C.; C. Forse, A.; Merlet, C. Efficient Prediction of Nucleus Independent Chemical Shifts for Polycyclic Aromatic Hydrocarbons. *Phys. Chem. Chem. Phys.* **2020**, *22* (24), 13746–13755.

(21) Kirschbaum, T.; Rominger, F.; Mastalerz, M. A Chiral Polycyclic Aromatic Hydrocarbon Monkey Saddle. *Angew. Chem. Int. Ed.* **2020**, *59* (1), 270–274.

(22) Bauschlicher, C. W. The Infrared Spectra of Nonplanar Polycyclic Aromatic Hydrocarbons with Five- or Seven-Membered Rings. *Chem. Phys.* **2015**, *448*, 43–52.

(23) Helicenes: Synthesis and Applications | Chemical Reviews.

(24) Sapir, M.; Donckt, E. V. Intersystem Crossing in the Helicenes. *Chem. Phys. Lett.* **1975**, *36* (1), 108–110.

(25) Collins, S. K.; Grandbois, A.; Vachon, M. P.; Côté, J. Preparation of Helicenes through Olefin Metathesis. *Angew. Chem.* **2006**, *118* (18), 2989–2992.

(26) Sehnal, P.; Stará, I. G.; Šaman, D.; Tichý, M.; Míšek, J.; Cvačka, J.; Rulíšek, L.; Chocholoušová, J.; Vacek, J.; Goryl, G.; et al. An Organometallic Route to Long Helicenes. *Proc. Natl. Acad. Sci.* **2009**, *106* (32), 13169–13174.

(27) Avlasevich, Y.; Li, C.; Müllen, K. Synthesis and Applications of Core-Enlarged Perylene Dyes. *J. Mater. Chem.* **2010**, *20* (19), 3814–3826.

(28) Feng, J.; Jiang, W.; Wang, Z. Synthesis and Application of Rylene Imide Dyes as Organic Semiconducting Materials. *Chem. – Asian J.* **2018**, *13* (1), 20–30.

(29) Herrmann, A.; Müllen, K. From Industrial Colorants to Single Photon Sources and Biolabels: The Fascination and Function of Rylene Dyes. *Chem. Lett.* **2006**, *35* (9), 978–985.

(30) Wong, W.-S.; Stępień, M. Emerging Applications of Curved Aromatic Compounds. *Trends Chem.* **2022**, *4* (7), 573–576.

(31) Bae, Y. J.; Zhao, X.; Kryzaniak, M. D.; Nagashima, H.; Strzalka, J.; Zhang, Q.; Wasielewski, M. R. Spin Dynamics of Quintet and Triplet States Resulting from Singlet Fission in Oriented Terrylenediimide and Quaterrylenediimide Films. *J. Phys. Chem. C* **2020**.

(32) Basel, B. S.; Zirzlmeier, J.; Hetzer, C.; Phelan, B. T.; Krzyaniak, M. D.; Reddy, S. R.; Coto, P. B.; Horwitz, N. E.; Young, R. M.; White, F. J.; et al. Unified Model for Singlet Fission within a Non-Conjugated Covalent Pentacene Dimer. *Nat. Commun.* **2017**, *8* (1), 1–8.

(33) Bayliss, S. L.; Chepelianskii, A. D.; Sepe, A.; Walker, B. J.; Ehrler, B.; Bruzek, M. J.; Anthony, J. E.; Greenham, N. C. Geminate and Nongeminate Recombination of Triplet Excitons Formed by Singlet Fission. *Phys. Rev. Lett.* **2014**, *112* (23), 238701.

(34) Zimmerman, P. M.; Zhang, Z.; Musgrave, C. B. Singlet Fission in Pentacene through Multi-Exciton Quantum States. *Nat. Chem.* **2010**, *2* (8), 648–652.

(35) Zhou, L.; Geng, J.; Liu, B. Graphene Quantum Dots from Polycyclic Aromatic Hydrocarbon for Bioimaging and Sensing of Fe3+ and Hydrogen Peroxide. *Part. Part. Syst. Charact.* **2013**, *30* (12), 1086–1092.

(36) Wang, X.-Y.; Yao, X.; Müllen, K. Polycyclic Aromatic Hydrocarbons in the Graphene Era. *Sci. China Chem.* **2019**, *62* (9), 1099–1144.

(37) Maluleke, R.; Oluwafemi, O. S. Synthetic Approaches, Modification Strategies and the Application of Quantum Dots in the Sensing of Priority Pollutants. *Appl. Sci.* **2021**, *11* (24), 11580.

(38) El Abbassi, M.; Perrin, M. L.; Barin, G. B.; Sangtarash, S.; Overbeck, J.; Braun, O.; Lambert, C. J.; Sun, Q.; Prechtl, T.; Narita, A.; et al. Controlled Quantum Dot Formation in Atomically Engineered Graphene Nanoribbon Field-Effect Transistors. *ACS Nano* **2020**.

(39) Sun, Z.; Wu, J. Open-Shell Polycyclic Aromatic Hydrocarbons. *J. Mater. Chem.* **2012**, *22* (10), 4151–4160.

(40) Kubo, T. Phenalenyl-Based Open-Shell Polycyclic Aromatic Hydrocarbons. *Chem. Rec.* **2015**, *15* (1), 218–232.

(41) Sánchez-Grande, A.; Urgel, J. I.; Veis, L.; Edalatmanesh, S.; Santos, J.; Lauwaet, K.; Mutombo, P.; Gallego, J. M.; Brabec, J.; Beran, P.; et al. Unravelling the Open-Shell Character of Peripentacene on Au(111). *J. Phys. Chem. Lett.* **2021**, *12* (1), 330–336.

(42) Gomberg, M. AN INSTANCE OF TRIVALENT CARBON: TRIPHENYLMETHYL. *J. Am. Chem. Soc.* **1900**, *22* (11), 757–771.

(43) Hicks, R. G. What's New in Stable Radical Chemistry? *Org. Biomol. Chem.* **2006**, *5* (9), 1321–1338.

(44) Herzog, S.; Hinz, A.; Breher, F.; Podlech, J. Cyclopenta-Fused Polyaromatic Hydrocarbons: Synthesis and Characterisation of a Stable, Carbon-Centred Helical Radical. *Org. Biomol. Chem.* **2022**, *20* (14), 2873–2880.

(45) Guo, J.; Zhou, C.; Xie, S.; Luo, S.; Gopalakrishna, T. Y.; Sun, Z.; Jouha, J.; Wu, J.; Zeng, Z. Large Aromatic Hydrocarbon Radical Cation with Global Aromaticity and State-Associated Magnetic Activity. *Chem. Mater.* **2020**, *32* (14), 5927–5936.

(46) Cobas, E.; Friedman, A. L.; van't Erve, O. M. J.; Robinson, J. T.; Jonker, B. T. Graphene As a Tunnel Barrier: Graphene-Based Magnetic Tunnel Junctions. *Nano Lett.* **2012**, *12* (6), 3000–3004.

(47) Han, W.; Kawakami, R. K.; Gmitra, M.; Fabian, J. Graphene Spintronics. *Nat. Nanotechnol.* **2014**, *9* (10), 794–807.

(48) Zatko, V.; Dubois, S. M.-M.; Godel, F.; Galbiati, M.; Peiro, J.; Sander, A.; Carretero, C.; Vecchiola, A.; Collin, S.; Bouzehouane, K.; et al. Almost Perfect Spin Filtering in Graphene-Based Magnetic Tunnel Junctions. *ACS Nano* **2022**, *16* (9), 14007–14016.

(49) Mishra, S.; Yao, X.; Chen, Q.; Eimre, K.; Gröning, O.; Ortiz, R.; Di Giovannantonio, M.; Sancho-García, J. C.; Fernández-Rossier, J.; Pignedoli, C. A.; et al. Large Magnetic Exchange Coupling in Rhombus-Shaped Nanographenes with Zigzag Periphery. *Nat. Chem.* **2021**, *13* (6), 581–586.

(50) Mishra, S.; Catarina, G.; Wu, F.; Ortiz, R.; Jacob, D.; Eimre, K.; Ma, J.; Pignedoli, C. A.; Feng, X.; Ruffieux, P.; et al. Observation of Fractional Edge Excitations in Nanographene Spin Chains. *Nature* **2021**, *598* (7880), 287–292.

(51) Li, N.; Jiang, H.-L.; Wang, X.; Wang, X.; Xu, G.; Zhang, B.; Wang, L.; Zhao, R.-S.; Lin, J.-M. Recent Advances in Graphene-Based Magnetic Composites for Magnetic Solid-Phase Extraction. *TrAC Trends Anal. Chem.* **2018**, *102*, 60–74.

(52) Compton, A. H. The Magnetic Electron. *J. Frankl. Inst.* **1921**, *192* (2), 145–155.

(53) Langmuir, I. The Arrangement of Electrons in Atoms and Molecules. *J. Frankl. Inst.* **1919**, *187* (3), 359–362.

(54) Gerlach, W.; Stern, O. Der experimentelle Nachweis der Richtungsquantelung im Magnetfeld. *Z. Für Phys.* **1922**, *9* (1), 349–352.

(55) Breit, G. Does the Electron Have an Intrinsic Magnetic Moment? *Phys. Rev.* **1947**, *72* (10), 984–984.

(56) Jacobson, P. Zur «Triphenylmethyl»-Frage. *Berichte Dtsch. Chem. Ges.* **1905**, *38* (1), 196–199.

(57) Koelsch, C. F.; Antees, J. A. ATTEMPTS TO SYNTHESIZE 9-PHENYL-PERINAPHTHANONE-7.

(58) Ballester, M.; Riera-Figueras, J.; Castaner, J.; Badfa, C.; Monso, J. M. Inert Carbon Free Radicals. I. Perchlorodiphenylmethyl and Perchlorotriphenylmethyl Radical Series. *J. Am. Chem. Soc.* **1971**, *93* (9), 2215–2225.

(59) Piloty, O.; Schwerin, B. G. Ueber Die Existenz von Derivaten Des Vierwertigen Stickstoffs. (I. Mittheilung.). *Berichte Dtsch. Chem. Ges.* **1901**, *34* (2), 1870–1887.

(60) Ullman, E. F.; Osiecki, J. H.; Boocock, D. G. B.; Darcy, R. Stable Free Radicals. X. Nitronyl Nitroxide Monoradicals and Biradicals as Possible Small Molecule Spin Labels. *J. Am. Chem. Soc.* **1972**, *94* (20), 7049–7059.

(61) Tidwell, T. T. Triarylmethyl and Related Radicals. In *Stable Radicals*; John Wiley & Sons, Ltd, 2010; pp 1–31.

(62) Veciana, J.; Ratera, I. Polychlorotriphenylmethyl Radicals: Towards Multifunctional Molecular Materials. In *Stable Radicals*; John Wiley & Sons, Ltd, 2010; pp 33–80.

(63) Morita, Y.; Nishida, S. Phenalenyls, Cyclopentadienyls, and Other Carbon-Centered Radicals. In *Stable Radicals*; John Wiley & Sons, Ltd, 2010; pp 81–145.

(64) Karoui, H.; Moigne, F. L.; Ouari, O.; Tordo, P. Nitroxide Radicals: Properties, Synthesis and Applications. In *Stable Radicals*; John Wiley & Sons, Ltd, 2010; pp 173–229.

(65) Min, H.; Hill, J. E.; Sinitsyn, N. A.; Sahu, B. R.; Kleinman, L.; MacDonald, A. H. Intrinsic and Rashba Spin-Orbit Interactions in Graphene Sheets. *Phys. Rev. B* **2006**, *74* (16), 165310.

(66) Koch, R. J.; Weser, M.; Zhao, W.; Viñes, F.; Gotterbarm, K.; Kozlov, S. M.; Höfert, O.; Ostler, M.; Papp, C.; Gebhardt, J.; et al. Growth and Electronic Structure of Nitrogen-Doped Graphene on Ni(111). *Phys. Rev. B* **2012**, *86* (7), 075401.

(67) Li, X.-F.; Lian, K.-Y.; Qiu, Q.; Luo, Y. Half-Filled Energy Bands Induced Negative Differential Resistance in Nitrogen-Doped Graphene. *Nanoscale* **2015**, *7* (9), 4156–4162.

(68) Pavliček, N.; Mistry, A.; Majzik, Z.; Moll, N.; Meyer, G.; Fox, D. J.; Gross, L. Synthesis and Characterization of Triangulene. *Nat. Nanotechnol.* **2017**, *12* (4), 308–311.

(69) Mishra, S.; Beyer, D.; Eimre, K.; Liu, J.; Berger, R.; Groening, O.; Pignedoli, C. A.; Müllen, K.; Fasel, R.; Feng, X.; et al. Synthesis and Characterization of π-Extended Triangulene. *J. Am. Chem. Soc.* **2019**, jacs.9b05319.

(70) Su, J.; Telychko, M.; Hu, P.; Macam, G.; Mutombo, P.; Zhang, H.; Bao, Y.; Cheng, F.; Huang, Z.-Q.; Qiu, Z.; et al. Atomically Precise Bottom-up Synthesis of π-Extended [5]Triangulene. *Sci. Adv.* **2019**, *5* (7), eaav7717.

(71) Mishra, S.; Xu, K.; Eimre, K.; Komber, H.; Ma, J.; Pignedoli, C. A.; Fasel, R.; Feng, X.; Ruffieux, P. Synthesis and Characterization of [7]Triangulene. *Nanoscale* **2021**, *13* (3), 1624–1628.

(72) Mishra, S.; Beyer, D.; Eimre, K.; Ortiz, R.; Fernández-Rossier, J.; Berger, R.; Gröning, O.; Pignedoli, C. A.; Fasel, R.; Feng, X.; et al. Collective All-Carbon Magnetism in Triangulene Dimers. *Angew. Chem. Int. Ed.* **2020**, *59* (29), 12041–12047.

(73) Mishra, S.; Beyer, D.; Eimre, K.; Kezilebieke, S.; Berger, R.; Gröning, O.; Pignedoli, C. A.; Müllen, K.; Liljeroth, P.; Ruffieux, P.; et al. Topological Frustration Induces Unconventional Magnetism in a Nanographene. *Nat. Nanotechnol.* **2019**.

(74) Hieulle, J.; Castro, S.; Friedrich, N.; Vegliante, A.; Lara, F. R.; Sanz, S.; Rey, D.; Corso, M.; Frederiksen, T.; Pascual, J. I.; et al. On-Surface Synthesis and Collective Spin Excitations of a Triangulene-Based Nanostar. *Angew. Chem. Int. Ed.* **2021**, *60* (48), 25224–25229.

(75) Clar, E. The Aromatic Sextet. In *Mobile Source Emissions Including Policyclic Organic Species*; Rondia, D., Cooke, M., Haroz, R. K., Eds.; NATO ASI Series; Springer Netherlands: Dordrecht, 1983; pp 49–58.

(76) Balaban, A. T.; Klein, D. J. Claromatic Carbon Nanostructures. *J. Phys. Chem. C* **2009**, *113* (44), 19123–19133.

(77) Solà, M. Forty Years of Clar's Aromatic π-Sextet Rule. *Front. Chem.* **2013**, *1*.

(78) Sun, Z.; Zeng, Z.; Wu, J. Zethrenes, Extended p-Quinodimethanes, and Periacenes with a Singlet Biradical Ground State. *Acc. Chem. Res.* **2014**, *47* (8), 2582–2591.

(79) Konishi, A.; Hirao, Y.; Nakano, M.; Shimizu, A.; Botek, E.; Champagne, B.; Shiomi, D.; Sato, K.; Takui, T.; Matsumoto, K.; et al. Synthesis and Characterization of Teranthene: A Singlet Biradical Polycyclic Aromatic Hydrocarbon Having Kekulé Structures. *J. Am. Chem. Soc.* **2010**, *132* (32), 11021–11023.

(80) Shimizu, A.; Konishi, A.; Hirao, Y.; Kubo, T. Singlet Open-Shell Character of Polyperiacenes. In *Graphene and Its Fascinating Attributes*; WORLD SCIENTIFIC, 2011; pp 45–57.

(81) Chen, Q.; Baumgarten, M.; Wagner, M.; Hu, Y.; Hou, I. C.-Y.; Narita, A.; Müllen, K. Dicyclopentaannelated Hexa-Peri-Hexabenzocoronenes with a Singlet Biradical Ground State. *Angew. Chem. n/a* (n/a).

(82) Shen, J.-J.; Han, Y.; Dong, S.; Phan, H.; Herng, T. S.; Xu, T.; Ding, J.; Chi, C. A Stable [4,3]Peri-Acene Diradicaloid: Synthesis, Structure, and Electronic Properties. *Angew. Chem.* **2021**, *133* (9), 4514–4519.

(83) Hu, P.; Wu, J. Modern Zethrene Chemistry. *Can. J. Chem.* **2017**, *95* (3), 223–233.

(84) Clar, E.; Mackay, C. C. Circobiphenyl and the Attempted Synthesis of 1:14, 3:4, 7:8, 10:11-Tetrabenzoperopyrene. *Tetrahedron* **1972**, *28* (24), 6041–6047.

(85) Motomura, S.; Nakano, M.; Fukui, H.; Yoneda, K.; Kubo, T.; Carion, R.; Champagne, B. Size Dependences of the Diradical Character and the Second Hyperpolarizabilities in Dicyclopenta -Fused Acenes : Relationships with Their Aromaticity/Antiaromaticity. *Phys. Chem. Chem. Phys.* **2011**, *13* (46), 20575–20583.

(86) Gong, Y.; Zhan, X.; Li, Q.; Li, Z. Progress of Pyrene-Based Organic Semiconductor in Organic Field Effect Transistors. *Sci. China Chem.* **2016**, *59* (12), 1623–1631.

(87) Bendikov, M.; Duong, H. M.; Starkey, K.; Houk, K. N.; Carter, E. A.; Wudl, F. Oligoacenes: Theoretical Prediction of Open-Shell Singlet Diradical Ground States. *J. Am. Chem. Soc.* **2004**, *126* (24), 7416–7417.

(88) Ishida, T.; Aihara, J. Aromaticity of Neutral and Doubly Charged Polyacenes. *Phys. Chem. Chem. Phys.* **2009**, *11* (33), 7197–7201.

(89) Shil, S.; Roy, M.; Misra, A. Role of the Coupler to Design Organic Magnetic Molecules: LUMO Plays an Important Role in Magnetic Exchange. *RSC Adv.* **2015**, *5* (128), 105574–105582.

(90) Hachmann, J.; Dorando, J. J.; Avilés, M.; Chan, G. K.-L. The Radical Character of the Acenes: A Density Matrix Renormalization Group Study. *J. Chem. Phys.* **2007**, *127* (13), 134309.

(91) Hajgató, B.; Szieberth, D.; Geerlings, P.; De Proft, F.; Deleuze, M. S. A Benchmark Theoretical Study of the Electronic Ground State and of the Singlet-Triplet Split of Benzene and Linear Acenes. *J. Chem. Phys.* **2009**, *131* (22), 224321.

(92) Ruffieux, P.; Wang, S.; Yang, B.; Sánchez-Sánchez, C.; Liu, J.; Dienel, T.; Talirz, L.; Shinde, P.; Pignedoli, C. A.; Passerone, D.; et al. On-Surface Synthesis of Graphene Nanoribbons with Zigzag Edge Topology. *Nature* **2016**, *531* (7595), 489–492.

(93) Son, Y.-W.; Cohen, M. L.; Louie, S. G. Half-Metallic Graphene Nanoribbons. *Nature* **2006**, *444* (7117), 347–349.

(94) Yang, L.; Cohen, M. L.; Louie, S. G. Magnetic Edge-State Excitons in Zigzag Graphene Nanoribbons. *Phys. Rev. Lett.* **2008**, *101* (18), 186401.

(95) Dutta, S.; Wakabayashi, K. Tuning Charge and Spin Excitations in Zigzag Edge Nanographene Ribbons. *Sci. Rep.* **2012**, *2* (1), 519.

(96) Fujita, M.; Wakabayashi, K.; Nakada, K.; Kusakabe, K. Peculiar Localized State at Zigzag Graphite Edge. *J. Phys. Soc. Jpn.* **1996**, *65* (7), 1920–1923.

(97) Lieb, E. H. Two Theorems on the Hubbard Model. *Phys. Rev. Lett.* **1989**, *62* (10), 1201–1204.

(98) Rizzo, D. J.; Veber, G.; Jiang, J.; McCurdy, R.; Cao, T.; Bronner, C.; Chen, T.; Louie, S. G.; Fischer, F. R.; Crommie, M. F. Inducing Metallicity in Graphene Nanoribbons via Zero-Mode Superlattices. *Science* **2020**, *369* (6511), 1597–1603.

(99) Palacios, J. J.; Fernández-Rossier, J.; Brey, L. Vacancy-Induced Magnetism in Graphene and Graphene Ribbons. *Phys. Rev. B* **2008**, *77* (19), 195428.

(100) Liu, J.; Mishra, S.; Pignedoli, C. A.; Passerone, D.; Urgel, J. I.; Fabrizio, A.; Lohr, T. G.; Ma, J.; Komber, H.; Baumgarten, M.; et al. Open-Shell Nonbenzenoid Nanographenes Containing Two Pairs of Pentagonal and Heptagonal Rings. *J. Am. Chem. Soc.* **2019**, *141* (30), 12011–12020.

(101) Su, J.; Telychko, M.; Song, S.; Lu, J. Triangulenes: From Precursor Design to On-Surface Synthesis and Characterization. *Angew. Chem. Int. Ed.* **2020**, *59* (20), 7658–7668.

(102) Turco, E.; Bernhardt, A.; Krane, N.; Valenta, L.; Fasel, R.; Jur, M.; Ruffieux, P. Direct Observation of the Magnetic Ground State of the Two Smallest Triangular Nanographenes.

(103) Goto, K.; Kubo, T.; Yamamoto, K.; Nakasuji, K.; Sato, K.; Shiomi, D.; Takui, T.; Kubota, M.; Kobayashi, T.; Yakusi, K.; et al. A Stable Neutral Hydrocarbon Radical: Synthesis, Crystal Structure, and Physical Properties of 2,5,8-Tri- *Tert* -Butyl-Phenalenyl. *J. Am. Chem. Soc.* **1999**, *121* (7), 1619–1620.

(104) Fukui, K.; Sato, K.; Shiomi, D.; Takui, T.; Itoh, K.; Kubo, T.; Gotoh, K.; Yamamoto, K.; Nakasuji, K.; Naito, A. Electronic Structure of a Stable Phenalenyl Radical as Studied by ESR/ENDOR, Paramagnetic NMR Spectroscopy and SQUID Measurements. *Mol. Cryst. Liq. Cryst. Sci. Technol. Sect. Mol. Cryst. Liq. Cryst.* **1999**, *334* (1), 49–58.

(105) Inoue, J.; Fukui, K.; Kubo, T.; Nakazawa, S.; Sato, K.; Shiomi, D.; Morita, Y.; Yamamoto, K.; Takui, T.; Nakasuji, K. The First Detection of a Clar's Hydrocarbon, 2,6,10-Tri- *Tert* -Butyltriangulene: A Ground-State Triplet of Non-Kekulé Polynuclear Benzenoid Hydrocarbon. *J. Am. Chem. Soc.* **2001**, *123* (50), 12702–12703.

(106) Sogo, P. B.; Nakazaki, M.; Calvin, M. Free Radical from Perinaphthene. *J. Chem. Phys.* **1957**, *26* (5), 1343–1345.

(107) Reid, D. H. The Chemistry of the Phenalenes. *Q. Rev. Chem. Soc.* **1965**, *19* (3), 274–302.

(108) Small, D.; Zaitsev, V.; Jung, Y.; Rosokha, S. V.; Head-Gordon, M.; Kochi, J. K. Intermolecular π-to-π Bonding between Stacked Aromatic Dyads. Experimental and

Theoretical Binding Energies and Near-IR Optical Transitions for Phenalenyl Radical/Radical versus Radical/Cation Dimerizations. *J. Am. Chem. Soc.* **2004**, *126* (42), 13850–13858.

(109) Tian, Y.-H.; Huang, J.; Kertesz, M. Fluxional σ-Bonds of 2,5,8-Tri-Tert-Butyl-1,3-Diazaphenalenyl Dimers: Stepwise [3,3], [5,5] and [7,7] Sigmatropic Rearrangements Viaπ-Dimer Intermediates. *Phys. Chem. Chem. Phys.* **2010**, *12* (19), 5084.

(110) Uchida, K.; Kubo, T. Recent Advances in the Chemistry of Phenalenyl. *J. Synth. Org. Chem. Jpn.* **2016**, *74* (11), 1069–1077.

(111) Pal, S. K.; Bag, P.; Itkis, M. E.; Tham, F. S.; Haddon, R. C. Enhanced Electrical Conductivity in a Substitutionally Doped Spiro-Bis(Phenalenyl)Boron Radical Molecular Solid. *J. Am. Chem. Soc.* **2014**, *136* (42), 14738–14741.

(112) Wehrmann, C. M.; Charlton, R. T.; Chen, M. S. A Concise Synthetic Strategy for Accessing Ambient Stable Bisphenalenyls toward Achieving Electroactive Open-Shell π-Conjugated Materials. *J. Am. Chem. Soc.* **2019**, *141* (7), 3240–3248.

(113) Imran, M.; Wehrmann, C. M.; Chen, M. S. Open-Shell Effects on Optoelectronic Properties: Antiambipolar Charge Transport and Anti-Kasha Doublet Emission from a N-Substituted Bisphenalenyl. *J. Am. Chem. Soc.* **2020**, *142* (1), 38–43.

(114) Clar, E.; Stewart, D. G. Aromatic Hydrocarbons. LXV. Triangulene Derivatives1. *J. Am. Chem. Soc.* **1953**, *75* (11), 2667–2672.

(115) Su, X.; Li, C.; Du, Q.; Tao, K.; Wang, S.; Yu, P. Atomically Precise Synthesis and Characterization of Heptauthrene with Triplet Ground State. *Nano Lett.* **2020**, *20* (9), 6859–6864.

(116) Su, J.; Fan, W.; Mutombo, P.; Peng, X.; Song, S.; Ondráček, M.; Golub, P.; Brabec, J.; Veis, L.; Telychko, M.; et al. On-Surface Synthesis and Characterization of [7]Triangulene Quantum Ring. *Nano Lett.* **2021**, *21* (1), 861–867.

(117) Cheng, S.; Xue, Z.; Li, C.; Liu, Y.; Xiang, L.; Ke, Y.; Yan, K.; Wang, S.; Yu, P. On-Surface Synthesis of Triangulene Trimers via Dehydration Reaction. *Nat. Commun.* **2022**, *13* (1), 1705.

(118) Delgado, A.; Dusold, C.; Jiang, J.; Cronin, A.; Louie, S. G.; Fischer, F. R. Evidence for Excitonic Insulator Ground State in Triangulene Kagome Lattice. arXiv January 15, 2023.

(119) The Story of the Intel® 4004.

(120) updated, A. S. last. China Now Produces One Billion Chips a Day.

(121) World Fab Forecast | SEMI.

(122) Cheung, K. P. On the 60 MV/Dec @300 K Limit for MOSFET Subthreshold Swing. In *System and Application Proceedings of 2010 International Symposium on VLSI Technology*; 2010; pp 72–73.

(123) Leiserson, C. E.; Thompson, N. C.; Emer, J. S.; Kuszmaul, B. C.; Lampson, B. W.; Sanchez, D.; Schardl, T. B. There's Plenty of Room at the Top: What Will Drive Computer Performance after Moore's Law? *Science* **2020**, *368* (6495).

(124) Borkar, S. Designing Reliable Systems from Unreliable Components: The Challenges of Transistor Variability and Degradation. *IEEE Micro* **2005**, *25* (6), 10–16.

(125) Takimiya, K.; Yamamoto, T.; Ebata, H.; Izawa, T. Design Strategy for Air-Stable Organic Semiconductors Applicable to High-Performance Field-Effect Transistors. *Sci. Technol. Adv. Mater.* **2007**, *8* (4), 273.

(126) Yu, E. T.; Sullivan, G. J.; Asbeck, P. M.; Wang, C. D.; Qiao, D.; Lau, S. S. Measurement of Piezoelectrically Induced Charge in GaN/AlGaN Heterostructure Field-Effect Transistors. *Appl. Phys. Lett.* **1997**, *71* (19), 2794–2796.

(127) Long, W.; Ou, H.; Kuo, J.-M.; Chin, K. K. Dual-Material Gate (DMG) Field Effect Transistor. *IEEE Trans. Electron Devices* **1999**, *46* (5), 865–870.

(128) Zhan, B.; Li, C.; Yang, J.; Jenkins, G.; Huang, W.; Dong, X. Graphene Field-Effect Transistor and Its Application for Electronic Sensing. *Small* **2014**, *10* (20), 4042–4065.

(129) Vadlamani, S. K.; Agarwal, S.; Limmer, D. T.; Louie, S. G.; Fischer, F. R.; Yablonovitch, E. Tunnel-FET Switching Is Governed by Non-Lorentzian Spectral Line Shape. *Proc. IEEE* **2020**, *108* (8), 1235–1244.

(130) Hall, K. C.; Flatté, M. E. Performance of a Spin-Based Insulated Gate Field Effect Transistor. *Appl. Phys. Lett.* **2006**, *88* (16), 162503.

(131) Liang, G.; Neophytou, N.; Nikonov, D. E.; Lundstrom, M. S. Performance Projections for Ballistic Graphene Nanoribbon Field-Effect Transistors. *IEEE Trans. Electron Devices* **2007**, *54* (4), 677–682.

(132) Yang, L.; Park, C.-H.; Son, Y.-W.; Cohen, M. L.; Louie, S. G. Quasiparticle Energies and Band Gaps in Graphene Nanoribbons. *Phys. Rev. Lett.* **2007**, *99* (18), 186801.

(133) Landauer, R. Irreversibility and Heat Generation in the Computing Process. *IBM J. Res. Dev.* **1961**, *5* (3), 183–191.

(134) Hirohata, A.; Yamada, K.; Nakatani, Y.; Prejbeanu, I.-L.; Diény, B.; Pirro, P.; Hillebrands, B. Review on Spintronics: Principles and Device Applications. *J. Magn. Magn. Mater.* **2020**, *509*, 166711.

(135) Gyongyosi, L.; Imre, S. A Survey on Quantum Computing Technology. *Comput. Sci. Rev.* **2019**, *31*, 51–71.

(136) Fischer, J.; Trauzettel, B.; Loss, D. Hyperfine Interaction and Electron-Spin Decoherence in Graphene and Carbon Nanotube Quantum Dots. *Phys. Rev. B* **2009**, *80* (15), 155401.

(137) Hurd, C. M. Varieties of Magnetic Order in Solids. *Contemp. Phys.* **1982**, *23* (5), 469–493.

(138) Electron Correlations in Narrow Energy Bands. *Proc. R. Soc. Lond. Ser. Math. Phys. Sci.* **1963**, *276* (1365), 238–257.

(139) Chao, K. A.; Spałek, J.; Oleś, A. M. Canonical Perturbation Expansion of the Hubbard Model. *Phys. Rev. B* **1978**, *18* (7), 3453–3464.

(140) Scalettar, R. 4 An Introduction to the Hubbard Hamiltonian; 2016.

(141) Hubbard, J.; Flowers, B. H. Electron Correlations in Narrow Energy Bands. *Proc. R. Soc. Lond. Ser. Math. Phys. Sci.* **1997**, *276* (1365), 238–257.

(142) Meyer, E.; Bennewitz, R.; Hug, H. J. Introduction to Scanning Tunneling Microscopy. In *Scanning Probe Microscopy: The Lab on a Tip*; Meyer, E., Bennewitz, R., Hug, H. J., Eds.; Graduate Texts in Physics; Springer International Publishing: Cham, 2021; pp 13–45.

(143) Zandvliet, H. J. W.; van Houselt, A. Scanning Tunneling Spectroscopy. *Annu. Rev. Anal. Chem.* **2009**, *2* (1), 37–55.

(144) Bode, M. Spin-Polarized Scanning Tunnelling Microscopy. *Rep. Prog. Phys.* **2003**, *66* (4), 523.

(145) Mukasa, K.; Sueoka, K.; Hasegawa, H.; Tazuke, Y.; Hayakawa, K. Spin-Polarized STM and Its Family. *Mater. Sci. Eng. B* **1995**, *31* (1), 69–76.

(146) Kondo, J. Resistance Minimum in Dilute Magnetic Alloys. *Prog. Theor. Phys.* **1964**, *32* (1), 37–49.

(147) Heinrich, A. J.; Gupta, J. A.; Lutz, C. P.; Eigler, D. M. Single-Atom Spin-Flip Spectroscopy. *Science* **2004**, *306* (5695), 466–469.

(148) Repp, J.; Meyer, G.; Stojković, S. M.; Gourdon, A.; Joachim, C. Molecules on Insulating Films: Scanning-Tunneling Microscopy Imaging of Individual Molecular Orbitals. *Phys. Rev. Lett.* **2005**, *94* (2), 026803.

(149) Fathi, D. A Review of Electronic Band Structure of Graphene and Carbon Nanotubes Using Tight Binding. *J. Nanotechnol.* **2011**, *2011*, e471241.

(150) Zhu, J.; Duan, R.; Zhang, S.; Jiang, N.; Zhang, Y.; Zhu, J. The Application of Graphene in Lithium Ion Battery Electrode Materials. *SpringerPlus* **2014**, *3* (1), 585.

(151) Nag, A.; Mitra, A.; Mukhopadhyay, S. C. Graphene and Its Sensor-Based Applications: A Review. *Sens. Actuators Phys.* **2018**, *270*, 177–194.

(152) Huang, C.; Li, C.; Shi, G. Graphene Based Catalysts. *Energy Environ. Sci.* **2012**, *5* (10), 8848–8868.

(153) Nika, D. L.; Balandin, A. A. Phonons and Thermal Transport in Graphene and Graphene-Based Materials. *Rep. Prog. Phys.* **2017**, *80* (3), 036502.

(154) Stankovich, S.; Dikin, D. A.; Dommett, G. H. B.; Kohlhaas, K. M.; Zimney, E. J.; Stach, E. A.; Piner, R. D.; Nguyen, S. T.; Ruoff, R. S. Graphene-Based Composite Materials. *Nature* **2006**, *442* (7100), 282–286.

(155) Semenov, Y. G.; Kim, K. W.; Zavada, J. M. Spin Field Effect Transistor with a Graphene Channel. *Appl. Phys. Lett.* **2007**, *91* (15), 153105.

(156) Britnell, L.; Gorbachev, R. V.; Jalil, R.; Belle, B. D.; Schedin, F.; Mishchenko, A.; Georgiou, T.; Katsnelson, M. I.; Eaves, L.; Morozov, S. V.; et al. Field-Effect Tunneling Transistor Based on Vertical Graphene Heterostructures. *Science* **2012**, *335* (6071), 947–950.

(157) Yakovkin, I. N. Dirac Cones in Graphene, Interlayer Interaction in Layered Materials, and the Band Gap in MoS2. *Crystals* **2016**, *6* (11), 143.

(158) Estrada, C. J.; Ma, Z.; Chan, M. Complementary Two-Dimensional (2-D) FET Technology With MoS2/HBN/Graphene Stack. *IEEE Electron Device Lett.* **2021**, *42* (12), 1890–1893.

(159) Carr, S.; Massatt, D.; Fang, S.; Cazeaux, P.; Luskin, M.; Kaxiras, E. Twistronics: Manipulating the Electronic Properties of Two-Dimensional Layered Structures through Their Twist Angle. *Phys. Rev. B* **2017**, *95* (7), 075420.

(160) Saxman, A. M.; Liepins, R.; Aldissi, M. Polyacetylene: Its Synthesis, Doping and Structure. *Prog. Polym. Sci.* **1985**, *11* (1), 57–89.

(161) Natta, G.; Pino, P.; Mazzanti, G.; Giannini, U. Complessi Cristallizzabili Contenenti Titanio e Alluminio Cataliticamente Attivi Nella Polimerizzazione Dell'etilene. *J. Inorg. Nucl. Chem.* **1958**, *8*, 612–619.

(162) Shirakawa, H. The Discovery of Polyacetylene Film: The Dawning of an Era of Conducting Polymers (Nobel Lecture). *Angew. Chem. Int. Ed.* **2001**, *40* (14), 2574–2580.

(163) Shirakawa, H.; J. Louis, E.; G. MacDiarmid, A.; K. Chiang, C.; J. Heeger, A. Synthesis of Electrically Conducting Organic Polymers: Halogen Derivatives of Polyacetylene, (CH) x. *J. Chem. Soc. Chem. Commun.* **1977**, *0* (16), 578–580.

(164) Ito, T.; Shirakawa, H.; Ikeda, S. Simultaneous Polymerization and Formation of Polyacetylene Film on the Surface of Concentrated Soluble Ziegler-Type Catalyst Solution. *J. Polym. Sci. Polym. Chem. Ed.* **1974**, *12* (1), 11–20.

(165) Hudson, B. S. Polyacetylene: Myth and Reality. *Materials* **2018**, *11* (2), 242.

(166) Wang, S.; Sun, Q.; Gröning, O.; Widmer, R.; Pignedoli, C. A.; Cai, L.; Yu, X.; Yuan, B.; Li, C.; Ju, H.; et al. On-Surface Synthesis and Characterization of Individual Polyacetylene Chains. *Nat. Chem.* **2019**, *11* (10), 924–930.

(167) Ni, X.; Li, H.; Liu, F.; Brédas, J.-L. Engineering of Flat Bands and Dirac Bands in Two-Dimensional Covalent Organic Frameworks (COFs): Relationships among Molecular Orbital Symmetry, Lattice Symmetry, and Electronic-Structure Characteristics. *Mater. Horiz.* **2022**, *9* (1), 88–98.

(168) Singapore, N. U. of. On-surface synthesis of graphene molecules and their superlattices.

(169) Adjizian, J.-J.; Briddon, P.; Humbert, B.; Duvail, J.-L.; Wagner, P.; Adda, C.; Ewels, C. Dirac Cones in Two-Dimensional Conjugated Polymer Networks. *Nat. Commun.* **2014**, *5* (1), 5842.

(170) Thomas, S.; Li, H.; Bredas, J.-L. Emergence of an Antiferromagnetic Mott Insulating Phase in Hexagonal π-Conjugated Covalent Organic Frameworks. *Adv. Mater.* **2019**, *31* (17), 1900355.

(171) Kumar, A.; Banerjee, K.; Foster, A. S.; Liljeroth, P. Two-Dimensional Band Structure in Honeycomb Metal–Organic Frameworks. *Nano Lett.* **2018**, *18* (9), 5596–5602.

(172) Gomes, K. K.; Mar, W.; Ko, W.; Guinea, F.; Manoharan, H. C. Designer Dirac Fermions and Topological Phases in Molecular Graphene. *Nature* **2012**, *483* (7389), 306–310.

(173) Zhang, B.; Zhang, Y.; Wang, Z.; Wang, D.; Baker, P. J.; Pratt, F. L.; Zhu, D. Candidate Quantum Spin Liquid Due to Dimensional Reduction of a Two-Dimensional Honeycomb Lattice. *Sci. Rep.* **2014**, *4* (1), 6451.

(174) Steiner, C.; Gebhardt, J.; Ammon, M.; Yang, Z.; Heidenreich, A.; Hammer, N.; Görling, A.; Kivala, M.; Maier, S. Hierarchical On-Surface Synthesis and Electronic Structure of Carbonyl-Functionalized One- and Two-Dimensional Covalent Nanoarchitectures. *Nat. Commun.* **2017**, *8* (1), 14765.

(175) Schulzendorf, M.; Hinaut, A.; Kisiel, M.; Jöhr, R.; Pawlak, R.; Restuccia, P.; Meyer, E.; Righi, M. C.; Glatzel, T. Altering the Properties of Graphene on Cu(111) by Intercalation of Potassium Bromide. *ACS Nano* **2019**, *13* (5), 5485–5492.

(176) Jiang, S.; Neuman, T.; Boeglin, A.; Scheurer, F.; Schull, G. Topologically Localized Excitons in Single Graphene Nanoribbons. *Science* **2023**, *379* (6636), 1049–1054.

(177) Li, G.; Han, Y.; Zou, Y.; Lee, J. J. C.; Ni, Y.; Wu, J. Dearomatization Approach Toward a Superbenzoquinone-Based Diradicaloid, Tetraradicaloid, and Hexaradicaloid. *Angew. Chem.* **2019**, *131* (40), 14457–14464.

(178) Das, S.; Herng, T. S.; Zafra, J. L.; Burrezo, P. M.; Kitano, M.; Ishida, M.; Gopalakrishna, T. Y.; Hu, P.; Osuka, A.; Casado, J.; et al. Fully Fused Quinoidal/Aromatic Carbazole Macrocycles with Poly-Radical Characters. *J. Am. Chem. Soc.* **2016**, *138* (24), 7782–7790.

(179) Hu, P.; Lee, S.; Herng, T. S.; Aratani, N.; Gonçalves, T. P.; Qi, Q.; Shi, X.; Yamada, H.; Huang, K.-W.; Ding, J.; et al. Toward Tetraradicaloid: The Effect of Fusion Mode on Radical Character and Chemical Reactivity. *J. Am. Chem. Soc.* **2016**, *138* (3), 1065–1077.

(180) Lu, X.; Gopalakrishna, T. Y.; Phan, H.; Herng, T. S.; Jiang, Q.; Liu, C.; Li, G.; Ding, J.; Wu, J. Global Aromaticity in Macrocyclic Cyclopenta-Fused Tetraphenanthrenylene Tetraradicaloid and Its Charged Species. *Angew. Chem.* **2018**, *130* (40), 13236–13240.

(181) Jeon, S.; Han, P.; Jeong, J.; Hwang, W. S.; Hong, S. W. Highly Aligned Polymeric Nanowire Etch-Mask Lithography Enabling the Integration of Graphene Nanoribbon Transistors. *Nanomaterials* **2021**, *11* (1), 33.

(182) Li, X.; Wang, X.; Zhang, L.; Lee, S.; Dai, H. Chemically Derived, Ultrasmooth Graphene Nanoribbon Semiconductors. *Science* **2008**, *319* (5867), 1229–1232.

(183) Ago, H.; Kayo, Y.; Solís-Fernández, P.; Yoshida, K.; Tsuji, M. Synthesis of High-Density Arrays of Graphene Nanoribbons by Anisotropic Metal-Assisted Etching. *Carbon* **2014**, *78*, 339–346.

(184) Jin, J. E.; Lee, J.-H.; Choi, J. H.; Jang, H.-K.; Na, J.; Whang, D.; Kim, D.-H.; Kim, G. T. Catalytic Etching of Monolayer Graphene at Low Temperature via Carbon Oxidation. *Phys. Chem. Chem. Phys.* **2015**, *18* (1), 101–109.

(185) Jiao, L.; Zhang, L.; Wang, X.; Diankov, G.; Dai, H. Narrow Graphene Nanoribbons from Carbon Nanotubes. *Nature* **2009**, *458* (7240), 877–880.

(186) Kosynkin, D. V.; Higginbotham, A. L.; Sinitskii, A.; Lomeda, J. R.; Dimiev, A.; Price, B. K.; Tour, J. M. Longitudinal Unzipping of Carbon Nanotubes to Form Graphene Nanoribbons. *Nature* **2009**, *458* (7240), 872–876.

(187) Han, M. Y.; Brant, J. C.; Kim, P. Electron Transport in Disordered Graphene Nanoribbons. *Phys. Rev. Lett.* **2010**, *104* (5), 056801.

(188) Saloriutta, K.; Hancock, Y.; Kärkkäinen, A.; Kärkkäinen, L.; Puska, M. J.; Jauho, A.-P. Electron Transport in Edge-Disordered Graphene Nanoribbons. *Phys. Rev. B* **2011**, *83* (20), 205125.

(189) Mucciolo, E. R.; Castro Neto, A. H.; Lewenkopf, C. H. Conductance Quantization and Transport Gaps in Disordered Graphene Nanoribbons. *Phys. Rev. B* **2009**, *79* (7), 075407.

(190) Yang, Y.; Murali, R. Impact of Size Effect on Graphene Nanoribbon Transport. *IEEE Electron Device Lett.* **2010**, *31* (3), 237–239.

(191) Costa Girão, E.; Liang, L.; Cruz-Silva, E.; Filho, A. G. S.; Meunier, V. Emergence of Atypical Properties in Assembled Graphene Nanoribbons. *Phys. Rev. Lett.* **2011**, *107* (13), 135501.

(192) Cocchi, C.; Prezzi, D.; Ruini, A.; Caldas, M. J.; Molinari, E. Optical Properties and Charge-Transfer Excitations in Edge-Functionalized All-Graphene Nanojunctions. *J. Phys. Chem. Lett.* **2011**, *2* (11), 1315–1319.

(193) Wagner, P.; Ewels, C. P.; Ivanovskaya, V. V.; Briddon, P. R.; Pateau, A.; Humbert, B. Ripple Edge Engineering of Graphene Nanoribbons. *Phys. Rev. B* **2011**, *84* (13), 134110.

(194) Joshi, D.; Hauser, M.; Veber, G.; Berl, A.; Xu, K.; Fischer, F. R. Super-Resolution Imaging of Clickable Graphene Nanoribbons Decorated with Fluorescent Dyes. *J. Am. Chem. Soc.* **2018**, *140* (30), 9574–9580.

(195) Scherb, S.; Hinaut, A.; Yao, X.; Götz, A.; Al-Hilfi, S. H.; Wang, X.-Y.; Hu, Y.; Qiu, Z.; Song, Y.; Müllen, K.; et al. Solution-Synthesized Extended Graphene Nanoribbons Deposited by High-Vacuum Electrospray Deposition. *ACS Nano* **2023**, *17* (1), 597–605.

(196) Su, W. P.; Schrieffer, J. R.; Heeger, A. J. Solitons in Polyacetylene. *Phys. Rev. Lett.* **1979**, *42* (25), 1698–1701.

(197) Tung, R. T. (董梓則). The Physics and Chemistry of the Schottky Barrier Height. *Appl. Phys. Rev.* **2014**, *1* (1), 011304.

(198) Giubileo, F.; Di Bartolomeo, A. The Role of Contact Resistance in Graphene Field-Effect Devices. *Prog. Surf. Sci.* **2017**, *92* (3), 143–175.

(199) Qian, Q.; Li, G.; Jin, Y.; Liu, J.; Zou, Y.; Jiang, K.; Fan, S.; Li, Q. Trap-State-Dominated Suppression of Electron Conduction in Carbon Nanotube Thin-Film Transistors. *ACS Nano* **2014**, *8* (9), 9597–9605.

(200) Shimizu, A.; Kishi, R.; Nakano, M.; Shiomi, D.; Sato, K.; Takui, T.; Hisaki, I.; Miyata, M.; Tobe, Y. Indeno[2,1-b]Fluorene: A 20-π-Electron Hydrocarbon with Very Low-Energy Light Absorption. *Angew. Chem. Int. Ed.* **2013**, *52* (23), 6076–6079.

(201) Luo, D.; Lee, S.; Zheng, B.; Sun, Z.; Zeng, W.; Huang, K.-W.; Furukawa, K.; Kim, D.; D. Webster, R.; Wu, J. Indolo[2,3- b]Carbazoles with Tunable Ground States: How Clar's Aromatic Sextet Determines the Singlet Biradical Character. *Chem. Sci.* **2014**, *5* (12), 4944–4952.

(202) Acosta, V.; Hemmer, P. Nitrogen-Vacancy Centers: Physics and Applications. *MRS Bull.* **2013**, *38* (2), 127–130.

(203) Kolb, B.; Kertesz, M.; Thonhauser, T. Binding Interactions in Dimers of Phenalenyl and Closed-Shell Analogues. *J. Phys. Chem. A* **2013**, *117* (17), 3642–3649.

(204) Boudjouk, P.; Johnson, P. D. Improved Routes to Phenalene and Phenalanone. Alane, Borane, and Silane Reductions of Phenalenone. *J. Org. Chem.* **1978**, *43* (20), 3979–3980.

(205) Fieser, L. F.; Hershberg, E. B. A New Synthesis of 3,4-Benzpyrene Derivatives. *J. Am. Chem. Soc.* **1938**, *60* (7), 1658–1665.

(206) Späth, A.; Leibl, C.; Cieplik, F.; Lehner, K.; Regensburger, J.; Hiller, K.-A.; Bäumler, W.; Schmalz, G.; Maisch, T. Improving Photodynamic Inactivation of Bacteria in Dentistry: Highly Effective and Fast Killing of Oral Key Pathogens with Novel Tooth-Colored Type-II Photosensitizers. *J. Med. Chem.* **2014**, *57* (12), 5157–5168.

(207) Ospina, F.; Ramirez, A.; Cano, M.; Hidalgo, W.; Schneider, B.; Otálvaro, F. Synthesis of Positional Isomeric Phenylphenalenones. *J. Org. Chem.* **2017**, *82* (7), 3873–3879.

(208) Sun, Q.; Yu, X.; Bao, M.; Liu, M.; Pan, J.; Zha, Z.; Cai, L.; Ma, H.; Yuan, C.; Qiu, X.; et al. Direct Formation of C−C Triple-Bonded Structural Motifs by On-Surface Dehalogenative Homocouplings of Tribromomethyl-Substituted Arenes. *Angew. Chem.* **2018**, *130* (15), 4099–4102.

(209) Kinikar, A.; Di Giovannantonio, M.; Urgel, J. I.; Eimre, K.; Qiu, Z.; Gu, Y.; Jin, E.; Narita, A.; Wang, X.-Y.; Müllen, K.; et al. On-Surface Polyarylene Synthesis by Cycloaromatization of Isopropyl Substituents. *Nat. Synth.* **2022**, *1* (4), 289–296.

(210) Zaitsev, V.; Rosokha, S. V.; Head-Gordon, M.; Kochi, J. K. Steric Modulations in the Reversible Dimerizations of Phenalenyl Radicals via Unusually Weak Carbon-Centered π- and σ-Bonds. *J. Org. Chem.* **2006**, *71* (2), 520–526.

(211) Dilly, S.; Fotso Fotso, A.; Lejal, N.; Zedda, G.; Chebbo, M.; Rahman, F.; Companys, S.; Bertrand, H. C.; Vidic, J.; Noiray, M.; et al. From Naproxen Repurposing to Naproxen Analogues and Their Antiviral Activity against Influenza A Virus. *J. Med. Chem.* **2018**, *61* (16), 7202–7217.

(212) McCurdy, R. D.; Delgado, A.; Jiang, J.; Zhu, J.; Wen, E. C. H.; Blackwell, R. E.; Veber, G. C.; Wang, S.; Louie, S. G.; Fischer, F. R. Engineering Robust Metallic Zero-Mode States in Olympicene Graphene Nanoribbons. arXiv February 16, 2023.

(213) Jacobse, P. H.; McCurdy, R. D.; Jiang, J.; Rizzo, D. J.; Veber, G.; Butler, P.; Zuzak, R.; Louie, S. G.; Fischer, F. R.; Crommie, M. F. Bottom-up Assembly of Nanoporous Graphene with Emergent Electronic States. *J. Am. Chem. Soc.* **2020**, *142* (31), 13507–13514.

(214) Liu, C.-Y.; Gavryushin, A.; Knochel, P. Synthesis of Functionalized O-, m-, and p-Terphenyl Derivatives by Consecutive Cross-Coupling Reactions of Triazene-Substituted Arylboronic Esters. *Chem. – Asian J.* **2007**, *2* (8), 1020–1030.

(215) Yamamoto, K.; Suganomata, Y.; Inoue, T.; Kuriyama, M.; Demizu, Y.; Onomura, O. Copper-Catalyzed Asymmetric Oxidative Desymmetrization of 2-Substituted 1,2,3-Triols. *J. Org. Chem.* **2022**, *87* (9), 6479–6491.

(216) Enantioselective Oxidative Homocoupling and Cross-Coupling of 2-Naphthols Catalyzed by Chiral Iron Phosphate Complexes | Journal of the American Chemical Society.

(217) Frank, M.; Ahrens, J.; Bejenke, I.; Krick, M.; Schwarzer, D.; Clever, G. H. Light-Induced Charge Separation in Densely Packed Donor–Acceptor Coordination Cages. *J. Am. Chem. Soc.* **2016**, *138* (26), 8279–8287.

(218) Biehl, R.; Hinrichs, K.; Kurreck, H.; Lubitz, W.; Mennenga, U.; Roth, K. ESR, NMR, and ENDOR Studies of Partially Deuterated Phenyl Substituted Anthracenes. .Pi.-.Sigma. Delocalization. *J. Am. Chem. Soc.* **1977**, *99* (13), 4278–4286.

(219) Yamamoto, Y.; Tsurumaki, E.; Wakamatsu, K.; Toyota, S. Nano-Saturn: Experimental Evidence of Complex Formation of an Anthracene Cyclic Ring with C60. *Angew. Chem. Int. Ed.* **2018**, *57* (27), 8199–8202.

(220) Yan, C.; Shang, R.; Nakamoto, M.; Yamamoto, Y.; Adachi, Y. The Substituent Effect of Bridged Triarylamine Helicenes on Light-Emitting and Charge Transfer Properties. *Chem. Lett.* **2020**, *49* (5), 457–460.

(221) Chan, K. L.; Watkins, S. E.; Mak, C. S. K.; McKiernan, M. J.; Towns, C. R.; Pascu, S. I.; Holmes, A. B. Poly(9,9-Dialkyl-3,6-Dibenzosilole)—a High Energy Gap Host for Phosphorescent Light Emitting Devices. *Chem. Commun.* **2005**, No. 46, 5766–5768.

(222) Luliński, S.; Serwatowski, J.; Szczerbińska, M. Regioselective Generation of Aryllithiums from Substituted Bromobenzenes XC6H4Br (X = 4-Br, 4-I, 4-CN, 2-CN). *Eur. J. Org. Chem.* **2008**, *2008* (10), 1797–1801.

(223) Kumar, G. A.; Priya, P. G.; Alagar, M. Functional Phenylethynylene Side Arm Poly(Arylene Ethynylene) Conjugated Polymers: Optical and Electrochemical Behavior for Enrichment of Electronic Applications. *New J. Chem.* **2018**, *42* (8), 5767–5773.

(224) Forbes, D. C.; Ene, D. G.; Doyle, M. P. Stereoselective Synthesis of Substituted 5-Hydroxy-1,3-Dioxanes. *Synthesis* **1998**, *1998* (6), 879–882.

(225) Kamitori, Y.; Hojo, M.; Masuda, R.; Izumi, T.; Tsukamoto, S. Silica Gel as an Effective Catalyst for the Alkylation of Phenols and Some Heterocyclic Aromatic Compounds. *J. Org. Chem.* **1984**, *49* (22), 4161–4165.

(226) Facile Synthesis and Ring-Opening Cross Metathesis of Carbo- and Heterocyclic Bicyclo[3.2.1]oct-6-en-3-ones Using Gaseous Olefinic Reaction Partners - Mihovilovic - 2006 - Advanced Synthesis & Catalysis - Wiley Online Library.

(227) Jung, B.; Hong, M. S.; Kang, S. H. Enantioselective Synthesis of Tertiary Alcohols by the Desymmetrizing Benzoylation of 2-Substituted Glycerols. *Angew. Chem. Int. Ed.* **2007**, *46* (15), 2616–2618.